ABSTRACT

Title of Dissertation: SIMULATION OF MAGNETIC GRANULAR MEDIA USING OPEN SOURCE SOFT SPHERE DISCRETE ELEMENT METHOD

Thomas Leps
Doctor of Philosophy, 2021

Dissertation Directed by: Professor Christine Hartzell
Department of Aerospace Engineering

Magnetic granular media were investigated using a mutual dipole magnetic model integrated into the open source Soft Sphere Discrete Element Method (DEM) framework LAMMPS and LIGGGHTS. Using the magnetic model and the contact force models from LIGGGHTS, we simulated shear behavior of MagnetoRheological Fluids (MRF). We found that the size distribution of simulated particles significantly affects the qualitative and quantitative behavior of MRF in a simple shear cell. Additionally, including cohesion, rolling resistance, friction and other contact forces affect the simulated shear behavior. By using a high fidelity contact force model along with an accurate size distribution and the mutual dipole magnetic model we were able to accurately match experimental data for an example MRF.

We used the DEM model to aid in the development of a novel MRF valve operating on an alternative MRF behavior. Our jamming, MRF valve holds pressure through stable, but reversible jamming in the flow path, and is actuated by electropermanent magnets, which require no quiescent current to maintain their

magnetization states. These valves do not require the large power draw of conventional MRF valves to maintain their state. We were able to accurately predict the experimental jamming behavior of the MRF valve using Finite Element Analysis and LIGGGHTS with magnetization, further validating the model with a non-linear, non-continuum behavior. Our jamming MRF valve was demonstrated in a multi-segmented, elastomeric robot, actuated using MRF.

Using the magnetic DEM model coupled with self-gravity, the effects of magnetism on rubble pile magnetic asteroids were examined. We simulated formation, and disruption of metallic asteroids with remnant magnetizations using LAMMPS with permanent dipoles. We found that rubble pile asteroids, formed from clouds of magnetized grains, coalesce more quickly, and have higher porosities than asteroids coalesced from unmagnetized grains. Distortion and disruption was affected by magnetization during simulated YORP spin-up. Large fragments with high aspect ratios and low densities were formed from highly magnetized asteroids after disruption, matching the shapes of suspected metallic small bodies. Simulations of grain avalanching on the surface of magnetized asteroids found additional morphological differences from their unmagnetized counterparts, with reduced densities, increased angles of repose, and cornicing.

Simulation of Magnetic Granular Media Using Open Source Soft Sphere Discrete Element Method

by

Thomas Leps

Dissertation submitted to the Faculty of the Graduate School of the
University of Maryland, College Park in partial fulfillment
of the requirements for the degree of
Doctor of Philosophy
2021

Advisory Committee:
Professor Christine Hartzell, Chair/Advisor
Professor Raymond Sedwick
Professor Dave Akin
Professor Norman Wereley
Professor Derek Richardson

Acknowledgments

I would foremost like to give my gratitude to my advisor, Dr. Christine Hartzell, who allowed me to branch out and explore new exciting topics when I needed it, but brought me back to focus when necessary, and tolerated my globe-trotting aspirations when I absconded to the South Pole in the middle of my thesis writing. I'm honored that she made me a part of her lab during its formative years and enjoyed my time working under her tutelage immensely.

I'd like to thank my committee, Drs. Dave Akin, Ray Sedwick, Derick Richardson, and Norman Wereley who have likewise been extremely flexible and tolerant towards my unconventional position of completing my thesis from one of the most isolated locations on earth.

My parents, Cynthia and Richard, cultivated my curiosity from a young age, never getting too upset from disassembled electronics, and the messes I made from various 'science experiments' conducted in the kitchen when I was kid, as well as supporting my decision to quit my job to get my PhD as an adult.

My labmates in the GRAINS lab, Dr. Anthony DeCicco, Dr. Dylan Carter, Dr. Jackson Shannon, and Charles Pett made the long days, occasional nights, and frantic deadlines more bearable with their willingness to offer their expertise, fresh eyes, and humor to my work, and join me for weekly trivia breaks.

Finally I'd like to thank the whole 2021 South Pole Winterover crew for offering their support while I finished my research. We made it through a unique year together, including dwindling supplies at the store, a skeleton crew, and months of isolation before we even arrived at pole. I especially want to thank the galley crew who kept the leftover fridge stocked with delicious meals and snacks, allowing me to focus on writing in the middle of the night while the satellites were up, and the South Pole Telescope winterovers for letting me use their servers to run last minute simulations.

This work was supported, in part, by the NASA Early Stage Innovation grant NNX16AD17G.

Table of Contents

List of Tables

List of Figures

List of Abbreviations

Alnico	Aluminum-Nickel-Cobalt
BJT	Bipolar Junction Transistor
CFD	Computational Fluid Dynamics
CFD-DEM	Computational Fluid Dynamics and Discrete Element Method
CoM	Center of Mass
DEM	Discrete Element Method
DMT	Derjaguin-Muller-Toporov
DoF	Degrees of Freedom
DS1	Deep Space 1
EPM	Electropermanent Magnet
EPSD	Elastic Plastic Spring Dashpot
ERF	Electrorheological Fluid
FEA	Finite Element Analysis
HSDEM	Hard Sphere Discrete Element Method
ISRU	In-Situ Resource Utilization
LAMMPS	Large-scale Atomic/Molecular Massively Parallel Simulator
LIGGGHTS	LAMMPS Improved for General Granular and Granular Heat Transfer Simulations
MGP	Magnetic Gradient Pinch
MO	Mineral Oil
MRF	Magnetorheological Fluid
OA	Oleic Acid
PPPM	Particle-Particle Particle-Mesh

SDS	Spring Dashpot Slider
SJKR	Simplified Johnson-Kendall-Roberts
SLA	Stereolithography Apparatus
SMT	Surface Mount Technology
SSDEM	Soft Sphere Discrete Element Method
USD	United States Dollar
YORP	Yarkovsky-O'Keefe-Radzievskii-Paddack

Chapter 1: Introduction

1.1 Granular Mechanics of Magnetized Media

Granular media exists in the border between continuum mechanics and discrete media. They exhibit properties of solids, liquids, and gasses depending on the energy and structure of the system. In a jammed state they behave like solids while, when allowed to freely flow, or driven with moderate strength, they tend to behave like liquids. When driven at high energies they begin to exhibit gas like behaviors [4, 5, 6, 7].

Many systems can be modeled as granular media, from micro-scale to macro-scale materials, as long as they can be characterized by a mixture of individual grains with a large, individual internal strength and low tensile strength between grains. Soils, sands, powders, ice flows, rubble pile asteroids, and colloidal suspensions all behave like granular media in various contexts [7].

Two dimensional experiments are able to examine structures and force chains, however they are not representative of many real world conditions, and so are of limited applicability [8, 9, 10, 11]. Micro-structural analysis of 3-D granular systems requires expensive x-ray equipment and only captures snapshots of the system, making transient effects difficult to capture [12, 13, 14, 15]. To better understand 3D

systems of granular media, it is useful to simulate them, so that real time analysis of individual particle paths and transient structures can be studied in three dimensions. These simulations allow us to better understand when and why granular systems exhibit different phase behaviors, as well as when they will exhibit non-continuum behaviors such as jamming.

One important class of granular materials is magnetized granular media. Paramagnetic or ferromagnetic powders or agglomerates can be subject to magnetic forces. These include iron powders used in powder metallurgy, suspensions such as ferrofluids and magnetorheological fluids, metal dust from machine wear or manufacturing, and metallic agglomerates such as rubble pile asteroids. The added magnetic forces will affect the dynamics of these systems in unique ways due to the increased tensile strength and anisotropy of magnetic dipole interactions [6, 16].

These magnetic interactions have been simulated in the context of magnetorheological fluids (MRF) [17, 18, 19, 20, 21, 22, 23, 24, 25]. MRF are used in many systems as a controllable non-newtonian fluid. By applying a magnetic field to an MRF it undergoes a phase transition from liquid to solid [26]. The solid then transitions back to a shear thinning fluid above a critical shear stress known as the yield stress. By accurately simulating MRF we can obtain a better understanding of the mechanisms by which the MRF phase transitions occur. These insights into MRF behavior will allow us to more effectively optimize their performance. Additionally, non-standard, and non-bulk behaviors such as jamming can be predicted, allowing for mitigation of undesirable behavior and novel applications.

Using the data-sets available for MRF to validate magnetic interaction mod-

els integrated into DEM simulations, other systems that are less mature and less empirically accessible can be studied. Metallic, m-type, asteroids are composed of magnetizable material and may have remnant magnetizations [27, 28, 29]. M-type asteroids have not been explored, and little is known about their formation and structure. These asteroids may be rubble piles, which behave like a granular media [30, 31, 32, 33, 34]. By integrating self gravity, along with contact forces and magnetism in DEM simulations, we can simulate the formation and disruption of these asteroids, giving us a better understanding of the formation and evolution of small planetary bodies in the solar system and informing our design of future missions to these objects.

This work improves DEM simulation of MRF by adding a mutual dipole, soft magnetic induction force model to the open source Soft Sphere Discrete Element Method (SSDEM) software LIGGGHTS and using the magnetic force model, with high fidelity grain size distributions, as well as the extensive and well validated particle contact force models already included in LIGGGHTS, to simulate MRF with higher accuracy than in previous works. It goes on to model MRF in a novel valve application, which takes advantage of a nonstandard MRF operation using a jamming phase transition, and then demonstrates the valve's use in a multi-segmented elastomeric soft robot. Finally, using the magnetic force models, validated with MRF behaviors, it explores the granular behaviors of the interior and surface of self-gravitating small planetary bodies with remnant magnetizations.

1.2 Publications

The following publications and presentations were derived from the research presented in this work.

1.2.1 Journal Articles

- T. Leps, P.E. Glick, D Ruffatto III, A Parness, M T Tolley, and C Hartzell. A Low-Power, Jamming, Magnetorheological Valve using Electropermanent Magnets Suitable for Distributed Control in Soft Robots. *Smart Materials and Structures*, 29(10):105025, Sep 2020.

- T. Leps and C. Hartzell. High Fidelity, Discrete Element Method Simulation of Magnetorheological Fluids Using Accurate Particle Size Distributions in LIGGGHTS Extended With Mutual Dipole Method. *Materials Research Express*, 8(8):085701, Aug 2021.

- T. Leps and C. Hartzell. The Effects of Remnant Magnetization on the Formation, Disruption, and Surface morphology of Metallic Asteroids. *presubmission*, 2021.

1.2.2 Conferences

- T. Leps and C. Hartzell. Simulating Small Body Formation Using Soft Sphere DEM with Induced Magnetic Dipoles. *EPSC-DPS Joint Meeting*. Sep 2019. (Poster)

- T. Leps and C Hartzell. Cohesion and Avalanching on Metallic Asteroids with Remnant Magnetic Fields. *The Interdisciplinary Nature of Particulate Systems Gordon Research Conference*, Jul 2018.

- T. Leps and C. Hartzell. Simulation of a Magnetorheological Fluid Based, Jamming, Soft Gripper Using the Soft Sphere DEM Method in LIGGGHTS. 70^{th} *Annual Meeting of the APS Division of Fluid Dynamics*, Nov 2017.

- T. Leps and C. Hartzell. Simulation of Magnetorheological Fluid Using Soft Sphere Discrete Element Method [SS-DEM]. 18^{th} *Mid-Atlantic Soft Matter Meeting*, May 2017.

1.3 Literature Review

1.3.1 Granular Simulation

Due to the non-linear nature of granular media, modeling their behavior with just its bulk behavior is often insufficient [35]. Several emergent phenomena occur such as jamming and phase transitions, which need to be accurately predicted for a variety of industrial applications [36, 37, 38, 39]. In order to determine the micro-scale effects that lead to these behaviors, accurate simulations of granular systems are important [40].

Davis and Deresiewicz first simulated granular systems as a static system, with Hertzian contact forces (described in detail in chapter 2) between a lattice of disks [41]. Trollope and Berman also developed a lattice model that was able to match

elastic analytic solutions [42]. These simulations were for the purposes of analyzing structures made of granular systems and do not include dynamics between particles, instead measuring the bulk behavior of the system of discrete elements. Cundall and Strack developed a dynamic "Distinct" Element Method (DEM) computer model for the purposes of modeling structures, but capable of handling dynamic systems [43]. They validated their code using photoelastic disks and simulated filling and emptying of a chute to demonstrate their code's dynamic capabilities.

Campbell and Brennen first simulated dynamic granular flows with the purpose of analyzing microstructures during flows [44, 45]. They used a Hard Sphere model where collisions were resolved analytically between time steps and resultant velocities and positions were applied to the next time step. Between collisions, particle trajectories are considered inertial. The code was able to run three dimensional simulations, but due to computational limitations and experimental data available they simulated two dimensional disks and were able to recreate experimental results, including granular temperature as an important value in characterizing granular flow phases and behaviors.

Tsuji et. al. introduced Soft Sphere Discrete Element Method (SSDEM) to granular simulations, integrating equations of motion through the contact of particles by allowing them to interpenetrate each other with a restoring force [46]. The restoring normal force is calculated using the Hertzian contact model and a tangential force is calculated using the Mindlin contact force [47]. This allows for the simulation of dense systems with large numbers of contacts because it does not depend on having just a single contact per time-step like hard sphere DEM and also

allows contact stresses and force chains to be resolved.

Adding rolling resistance allows DEM programs to mimic irregular particles without the added computational costs associated with aspherical particles. Sakaguchi integrated a simple torque rolling resistance model and was able to accurately reproduce stable arch formation in silo jamming simulations [48]. Jiang introduced a two dimensional Elastic-Plastic Spring-Dashpot (EPSD) model where a spring dashpot force provided a restoring torque to an equilibrium point that could shift with large relative angular displacements between particles [49]. Ai et. al. expanded the EPSD model to three dimensions and improved the handling of back rolling [3].

The open source molecular dynamics software LAMMPS developed by Plimpton [50] and its derivative software LIGGGHTS developed by Kloss et. al. [51] implement a diverse range of contact force models which have been well validated in the literature eg. [3, 52, 53, 54, 55, 56, 57]. The modular nature of these software packages makes it possible to extend the code with new contact and long range forces.

1.3.2 Magnetorheological Fluid

Magnetorheological fluids are granular suspensions of soft magnetic particles, a carrier fluid such as silicone oil, mineral oil, or water, and surfactants to help maintain the particles in suspension [2, 58, 59, 60, 61, 62]. In its rest state, with no external magnetic field, MRF behaves like a liquid, however when a magnetic field is applied the MRF changes phase and behaves like a solid [58, 63]. Optimally, MRF

have a low off-state viscosity and a high on-state viscosity and revert back to a low viscosity state after removal of the magnetic field. MRF typically have an increasing yield stress with increasing magnetic field up to saturation of $\sim 700-1000\,\mathrm{mT}$ and yield strength of $\sim 100\,\mathrm{kPa}$ [26, 64, 65]. This bulk behavior can be approximated with several shear thinning models, including the Bingham Plastic, Herschel-Buckley, and bi-viscous models detailed by Ghaffari et al [24].

The particle size distributions and packing fraction affect the off and on-state viscosity of MRF [2, 66, 67, 68, 69]. Increasing particle size tends to increase the on-state yield stress, however it also results in faster settling of particles out of suspension, undesireable jamming transitions, and higher off-state viscosity. Typically the particle sizes are between 1 µm-10 µm. The MRF used by Goncalves, conversely, used larger particles on the order of 100 µm to intentionally create conditions where a jam could occur [70]. Similarly, increasing the packing fraction results in higher on and off-state viscosities, with most MRF using a packing fraction of $\phi = 0.3 - 0.45$ [2, 66, 67, 68, 69]. Interestingly, it has been found that using particles with two size distributions results in an enhancement in the yield stress and a reduction in the off-state viscosity, compared to either size distribution on its own, with the same packing fraction [2, 66, 68].

Magnetorheological fluids are used in a wide range of applications taking advantage of the bulk rheological behavior of the fluid [59, 60, 61, 62, 71]. These applications include valves, clutches, and dampers, which can all be actuated in real-time and their characteristics actively controlled with no additional moving parts. There are also some applications where the granular behavior is desirable.

Goncalves designed a unique MRF valve that takes advantage of a reversible jamming behavior where a constriction's effective diameter is decreased by the addition of a strong magnetic field gradient that attracts magnetic particles to the edge of the constriction [70]. MRF can also be used to polish surfaces to extremely fine finishes on the order of tens of nanometers and tens of angstroms RMS roughness, while limiting heating of the surface and wear of the polishing tools because the MRF is continuously circulated with the polishing grains suspended in the fluid, pulling heat and debris away while all of the shear forces are reacted within the fluid and not by the polishing tool [72].

To understand the mechanisms behind the bulk behavior of MRF and to better understand some non-standard behaviors such as jamming, it is desirable to understand the granular micro-behaviors of the MRF. Several experiments have attempted to capture the microstructures [63, 73]. Tang et. al. uses an epoxy resin instead of an oil as the MRF carrier fluid. This allows the iron particles to be frozen in their state and the resulting composite is then sectioned and analyzed with SEM. This approach is limited to static conditions as the MRF cannot be in motion as the resin is cured. It also does not allow for the capture of transient structures. Dimock et al. uses a quasi-2D cell, which allows for shearing and can capture transient effects, however is limited by the packing fraction that can be used and the geometries it can examine, as well as being subject to wall effects [63].

To examine microstructure of MRF without the limitations of experimental methods it is desirable to be able to simulate MRF with high fidelity. Due to their granular nature, SSDEM is well suited to simulation of MRF, however it requires

the addition of a long range magnetic force and modeling of the interstitial carrier fluid [17, 18, 20, 22, 25, 74]. When placed in a magnetic field, a paramagnetic or ferromagnetic particle will have a magnetic moment induced in the direction of the background field [16, 17, 19, 20]. In the case of a spherical particle, the resultant moment is purely a dipole moment. This is an exact solution to the Laplace equation resulting from Maxwell's equations. However, when the particle is surrounded by other particles as well, the boundary value problem for solving the Laplace equation quickly becomes intractable [16, 19, 20]. The 0th order approximation that the total magnetic moment is simply equal to the dipole moment induced by the background field, ignoring the contribution of the additional particles, works for disperse systems because the dipole field drops off proportional to distance cubed [19]. Early DEM simulations of MRF used this approximation [17] however, because MRF are generally a dense suspension, the assumption of independent magnetizations breaks down. Keaveny introduced the mutual dipole method, where the field from each close neighbor is added to the background field to calculate induced dipole moments. This process is iterated and rapidly converges within a few iterations and is used by many subsequent works [19, 20, 22]. This mutual dipole method increases attractive forces between two particles by up to 78% and reduces repulsive forces between two particles by up to 21% compared to the fixed dipole approximation, however it ignores multipole effects and still underestimates the force compared to an exact solution [20]. Kittipoomwong uses a Mean Field approximation, assuming that the two particle sizes in a bi-disperse mixture all have the same magnetic moment and solving directly assuming perfect dipoles [74].

The interstitial fluid can be modeled in a coupled or uncoupled regime. In an uncoupled regime, the effects of the particles on the fluid flow are ignored, and only the forces on the particles by the fluid are considered [17, 18, 22]. In coupled regimes the effect of the fluid on the particles and the effect of the particles on the fluid are both considered [20, 25]. Uncoupled flow generally takes the form of Stokes drag and is used in simple geometries where the bulk flow is well defined, such as stationary background fluids, or simple shear cells that will have Couette flow background flow profiles [17, 18, 22]. Stokes drag is generally a good approximation for individual particles with low Reynolds number. Han et al. instead use a Lattice-Boltzman coupled flow where fluid 'particles' move through lattice nodes, colliding with other fluid 'particles' at the nodes. The pressure is calculated from the density function, determined by the number of fluid 'particles' at each node. Boundary conditions are recovered from the 'particle' interactions at boundary nodes. Lagger uses a smoothed particle hydrodynamic model, another lagrangian method that treats the fluid as discrete fluid 'particles' [25]. Lagger found that for realistic MRF simulations, with low relative velocities between particles, simple stokes drag is sufficient for accurate simulations.

Most MRF simulations use monotonic particle sizes [17, 18, 20, 22, 25]. Typical particle size distributions for MRF are actually log-normal distributions [2, 68]. Furthermore particle size is known to significantly affect the MRF performance [2, 66, 67, 68, 69]. Kittipoomwong simulated a bi-disperse mixture in a 2D simulation and was able to recreate the yield stress enhancement, however each particle distribution was monotonic, with just two particle sizes, and the yield stresses were

much lower than experimental results [74]. Sherman simulated a theoretical log-normal distribution, but did not match a specific experimental distribution, and used a simple, fixed dipole, magnetic model [23].

1.3.3 MRF Valve

One application of Magnetorheological fluids is in solid state valves, which require no moving parts to actuate [26, 65, 70, 75, 76, 77, 78]. MR valves are typically larger than 25 mm-50 mm in diameter with the size limited by the pressure drop calculated by Abd-Fatah [71]:

$$P_{flow} \approx \frac{\tau_y L}{d} \tag{1.1}$$

requiring large magnetic fields to increase the yield strength (τ_y), long paths (L), or small effective path diameters (d) which then require large annular path circumferences to achieve good flow rates. They are also made of heavy magnetically permeable material, and require 1 W-100 W of steady power draw to actuate [70, 75]. Goncalves' MGP valve can hold significantly more pressure for a given size and power than traditional yield based MR valves by taking advantage of a granular jamming transition that does not follow Equation (1.1), and flows better when off due to a 2 mm diameter orifice, compared to pathways on the order of 0.1 mm wide used in traditional valve designs [70]. The MGP valve still requires on the order of watts of power to maintain the closed state and an electromagnet capable of maintaining amps of current, limiting its size. Gilpin and Knaian developed an alternative

electromagnet called an electropermanent magnet (EPM), which uses a very high current pulse on the order of 10's of amps for microseconds in order to permanently magnetize and demagnetize a high remnant permanent magnet [79, 80]. Because the current pulse is so short, the total energy used in switching and maintaining a state is very low, and the wire gauge carrying the current can be much smaller. This allows for magnetic fields on the order of hundreds of milliTesla to be maintained with a device on the order of tens of cubic millimeters in volume.

Simulation and modeling of MR valves can successfully be done with FEA to analyze the magnetic properties of the valve system and the bulk behavior of the MRF flowing in the valve [71, 76, 81]. Using the bulk behavior is insufficient to simulate an MGP valve however because jamming is a microscopic effect of the granular nature of MRF.

1.3.4 Simulation of Rubble Pile Asteroids

Davis et al. proposed that some asteroids are made up of gravitationally bound 'rubble piles' [82]. The spin rates of asteroids show a clustering near the limit of asteroid strength, as calculated for self-gravitating agglomerates, supporting that many asteroids could be rubble piles [83]. Observations of asteroids Itokawa, Ryugu, and Bennu by Hayabusa, Hayabusa 2, and OSIRIS-REx, have also been consistent with rubble piles, indicating that not only are some asteroids rubble piles, many or even most are [34, 84, 85, 86]. Holsapple showed that internal strength from rolling resistance, friction and cohesion could add to the maximum rotation velocity

before disruption [87, 88]. Scheeres showed that cohesion was an important force in asteroid strength, dominating gravity for a range of possible asteroid and grain sizes [89]. Hartzell found that cohesion could affect the surface morphology of asteroids by limiting reshaping due to electrostatic dust lofting [90].

Since rubble pile asteroids are granular systems they lend themselves to simulation with DEM. Richardson developed the PKDgrav software adding a Hard Sphere DEM solver to an n-body solver, allowing simulation of granular systems with self gravitation [30]. Richardson went on to include cohesive effects in these simulations [31]. In order to handle close contacts in a HSDEM simulation, Richardson used a crystalization model for bound particles. Sanchez implemented n-body long range forces into SSDEM allowing simulations to be run with one set of physics for the entire system [32]. PKDgrav was also modified to run SSDEM granular interactions [91]. To investigate the results of YORP effect spin-up on asteroid shape and disruption, Sanchez progressively stepped up the angular velocities of simulated cohesive aggregates to look at the effects of internal strength caused by rolling resistance, friction and cohesion on asteroid disruption patterns [33]. Sanchez found that increasing internal strength resulted in agglomerates that remained stable to higher spin rates. Additionally, as internal strengths increased, objects went from deforming into oblate spheroids and shedding grains individually or in small clumps, to fissuring into large fragments.

Asteroids and meteorites have been found to have remnant magnetic fields [27, 28, 29]. The magnetization of the asteroids Gaspra, and Braille, as well as magnetizations of meteorites are consistent with each other, implying that asteroid

magnetization may be somewhat common [29]. The consistent magnetization may be due to a primordial background magnetic field in the early solar system [27, 92].

M-type asteroids are assumed to be composed primarily of nickel and iron based on their spectral signature and similarities to metallic meteorites [93, 94]. Several potentially metallic small planetary bodies have densities and shapes that are not consistent with what would be expected from gravitation, friction, and cohesion [95, 96, 97]. Kleopatra has a dog bone shape with a long, skinny center with a bulge on either end [95]. Kalliope has an m-type spectral signature, but a density of just $3.4\,\mathrm{g/cm^3}$, which would require a very high porosity or the presence of a large amount silicates [96]. 'Oumuamua, has an extremely high aspect ratio, and experienced an extra-gravitational acceleration that requires either more outgassing than observed or a lower density than expected [97, 98].

Chapter 2: Simulation of Magnetorheological Fluid

This chapter contains material published in: T. Leps and C. Hartzell. High Fidelity, Discrete Element Method Simulation of Magnetorheological Fluids Using Accurate Particle Size Distributions in LIGGGHTS Extended With Mutual Dipole Method. *Materials Research Express*, 8(8):085701, Aug 2021. [99]

2.1 Introduction

Magnetorheological fluids (MRF) are mixtures of paramagnetic particles, with sizes on the order of microns to 10s of microns, in suspension with a carrier fluid and small amounts of various additives [59, 60, 61, 62]. An MRF flows similarly to a nearly Newtonian fluid when there is no applied magnetic field. When a magnetic field is applied, the paramagnetic particles form structures that impede the flow, resulting in a non-Newtonian, shear thinning, Bingham plastic (fig. 2.1) behavior. The MRF acts like a solid below a critical yield stress, then flows with a linear shear rate-stress curve offset from the origin by the yield stress. When the magnetic field is removed, the MRF reverts to its nearly Newtonian behavior [63]. The yield stress of MRF increases with magnetic field strength until saturation, at which point increasing the magnetic field does not significantly increase the yield stress.

The maximum yield stress for MRF is $\sim$100 kPa, at saturation of $\sim$700$-$1000 mT [26, 64, 65].

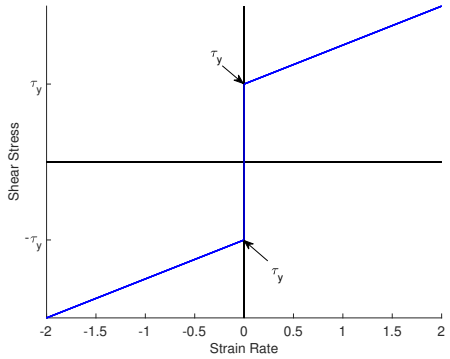

Figure 2.1: Magnetorheological fluid stress strain curve, modeled as a Bingham plastic, with no flow when $\tau \leq \tau_y$ [1].

The properties of MRF depend on the particle size and packing fraction. As packing fraction increases (ϕ), the off-state viscosity increases and the on-state yield stress increases [67, 69]. Most MRF formulations tend to fall between $\phi = 0.3 - 0.45$ representing a good compromise between off-state viscosity and yield stress. Similarly, as particle size increases, the off-state viscosity and on-state yield stress increase. However, as the particle size gets too large, the particles quickly settle out of suspension. Typical MRF formulations tend to have particle sizes between 1-10 µm. Interestingly, a bidisperse mixture of particles enhances the yield stress beyond that of a purely larger particle mixture, while also having an off-state viscosity lower than that of the smaller particles [2, 66, 68]. The lower off-state viscosity may be due to the reduced ratio of the packing fraction to the maximum packing fraction with bidisperse particle distributions, but the mechanism for the yield stress enhancement is not well understood.

The unique viscosity characteristics of MRF make them interesting in a wide

range of applications, including solid state valves, flow control, power transmission, polishing, and robotics [59, 60, 61, 62]. For many applications, it is desirable to maximize the yield stress for an applied magnetic field, while minimizing the off-state viscosity. Many of these properties are empirically determined. While empirical, bulk properties of MRF are sufficient to achieve good results in applications, better understanding of the MRF microstructure in use and how different formulations affect the characteristics can allow for better prediction of performance and optimization of designs, as well as development of novel applications.

In order to better understand MRF, it is useful to see what is happening at the microscopic level. Attempts have been made to capture the microstructures experimentally in both electrorheological and MR fluids by using resin as the carrier fluid and allowing it to set inside a field or making quasi-2D cells [63]. However, resin cannot capture dynamic or transient effects and quasi-2D cells affect the physics of the interactions. To overcome these shortcomings, many attempts have been made to simulate MRF using the Discrete Element Method (DEM) [17, 18, 20, 22, 25, 74]. DEM takes a brute force strategy; summing forces on individual particles and integrating their equations of motion [51]. Because the particle dynamics are fully determined from integrating Newton's 2nd Law, additional physics are easily implemented during the force summation step.

Early simulations were limited to quasi-2D models due to computational limitations. Such models are subject to similar limitations as the experimental work with monolayer cells [18], but were able to recreate the structures seen in the experimental cases. Mohebi extended simulations into full three-dimensional space

showing the formation of three-dimensional particle chains, however the magnetic induction model assumed fixed dipoles unaffected by the fields of adjacent particles and there was no attempt to characterize the rheology of the fluid [17]. Keaveny developed a mutual dipole method where the magnetic fields from nearby particles are included to calculate the magnetic moment of each particle, iteratively converging to a more accurate value [19]. This model has been used in several works [20, 22].

The effect of the hydrodynamics model on simulating MR fluids has also been examined. Often, uncoupled Stokes drag is assumed, where the carrier fluid is not affected by the particles and the drag on the particles is independent of its neighbors. In the case of a single grain at low Reynolds number, Stokes drag is very accurate; however, because of the dense packing of grains in contact with each other in an MRF, the assumptions break down. To get around the breakdown of the assumptions, attempts have been made at using coupled fluid dynamics where the effect of the particles on the fluid and the fluid on the particles is calculated using Computational Fluid Dynamics (CFD) [20, 25]. This increases the fidelity of the simulation; however, it also drastically increases computation time. Thus, for simple geometries with low shear rates, where relative velocities between the grains and the carrier fluid are low, uncoupled models are preferable for their lower computing costs.

One area that has not been fully explored is the effect of particle size distributions on DEM simulations of MRF. Most previous work has assumed a monotonic particle size distribution [17, 18, 20, 22, 25]. Kittipoomwong investigated bidisperse distributions, but again, used two monotonic particle distributions. Despite the

simple particle distribution model, they were able to show a yield strength enhancement for the bidisperse particle distribution, though the absolute yield stress was considerably lower than experimental values [74]. Actual particle distributions tend to follow log-normal distributions (fig. 2.2) [2, 68]. Due to the cubic relationship between volume and diameter, this can result in mixtures that have many smaller particles. A theoretical log-normal distribution was examined by Sherman using a simple fixed dipole model [23]. In this work we examine the effect of using hi-fidelity contact models and reproductions of the particle size distributions found in experimental investigations of MRF on the simulation of magnetorheological fluids using DEM software.

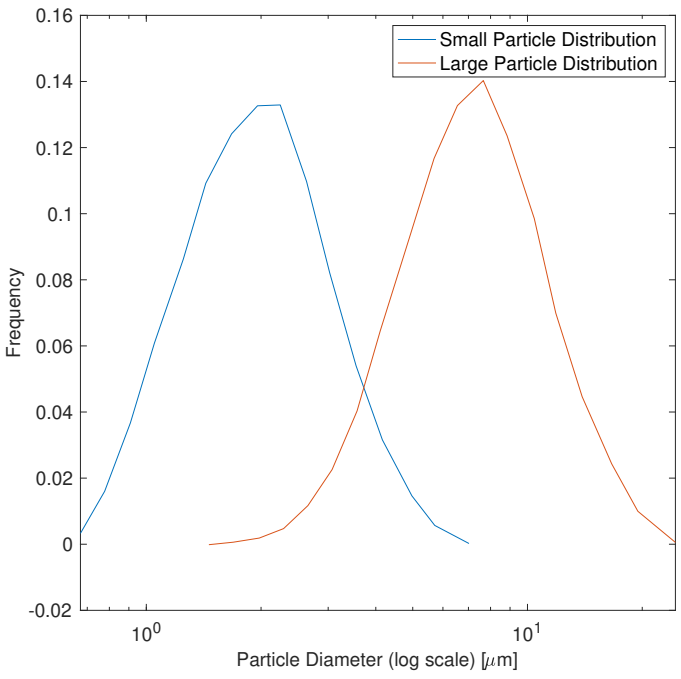

Figure 2.2: Two log-normal distributions used to create bidisperse MRF mixtures from Trendler and Bose with mean particle sizes of approximately 1.8 µm and 6.7 µm for the small and large particles, respectively [2].

2.2 Model

For our simulations we use LIGGGHTS an open-source Soft Sphere Discrete Element Method software [51]. LIGGGHTS, which is built on very mature LAMMPS code, is highly parallelizable and uses a modular code structure that makes it suitable for extension with custom models. We use 3D shear cells to examine the full structure and behavior of the MRF with high fidelity to experimental and applied geometries.

2.2.1 Contact Model

The particle-particle contact forces govern how particles resist interpenetrating and rebound off each other in collisions. There are two common contact models used in DEM simulations with magnetic particles. The highest fidelity model is the Hertzian model, which treats the particles as an elastic material with a defined Young's modulus and Poisson ratio. Given two spherical particles with radii R_i, R_j, Young's modulus Y_i, Y_j, Poisson ratio ν_i, ν_j, and coefficient of restitution e, co-penetrating each other a distance Δn_{ij}, with a normal component of their relative velocities $v_\perp$, the normal force between particles is given by (eq. (2.1)). The tangential force is similarly formulated with an additional sliding friction coefficient μ_x which limits the maximum Hertzian tangential force $F_t \leq F_n \mu_x$ [51].

$$F_n = k_n \Delta n_{ij} - \gamma_n v_\perp \tag{2.1}$$

$$k_n = \frac{4}{3} Y^* \sqrt{R^* \Delta n_{ij}}; \quad \gamma_n = -2\sqrt{\frac{5}{6}} \beta \sqrt{S_n m^*}$$

$$\frac{1}{Y^*} = \frac{1-\nu_i^2}{Y_i} + \frac{1-\nu_j^2}{Y_j}; \quad \beta = \frac{\ln(e)}{\sqrt{\ln^2(e) + \pi^2}}; \quad S_n = 2Y^* \sqrt{R^* \Delta n_{ij}}$$

where Y^*, m^*, and R^* are the reduced Young's modulus, reduced mass, and reduced radius of the particle pairs respectively. This contact force has the advantage of creating realistic separations between particles in contact, which is important due to the d^4 dependence of the magnetic force, however the spring force ramps up very quickly, creating a very stiff system. The stiffness of the system requires very short timesteps in order to maintain numerical stability in the system. To reduce the stiffness, some simulations have implemented an exponential contact force model (eq. (2.2)).

$$F_n = Q \exp\left[k \Delta n_{ij}\right] \tag{2.2}$$

where Q is chosen to cancel the maximum attractive magnetic force between the particles and k is chosen to balance the tradeoff between the stiffness of the system with the additional, unphysical repulsion force that extends past the particle contact distance [22].

To maximize the fidelity of our simulations, we use a Hertzian contact model in all our simulations. We also include several additional standard LIGGGHTS contact forces. A sliding friction coefficient μ_x limits the maximum Hertzian tangential force $F_t \leq F_n \mu_x$. Rolling resistance is included to mimic some of the mechanical effects of some asphericity in the iron grains using the Elastic-Plastic Spring-Dashpot (EPSD) model. This creates a static restoring spring torque back to original contact point,

which ramps up from zero to a maximum value as displacement increases, and then falls back along the same slope to zero as if the particles start to roll backwards (fig. 2.3) [3]. Finally, we include a cohesion term using the SJKR cohesion model $F_c = k_c A$, where A is the contact area and k_c is a volume energy density. Values used in our simulations can be found in Table 2.1.

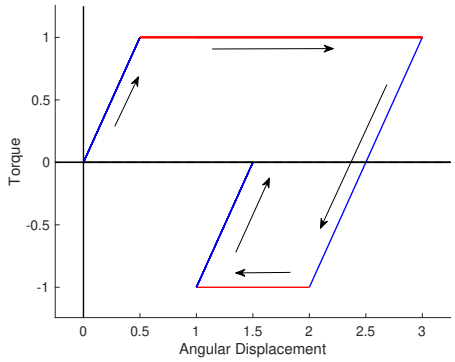

Figure 2.3: EPSD model for rolling resistance from Ai et al. Blue paths represent elastic torques where the particle will roll to a constant equilibrium point if allowed to. Red paths represent plastic deformations where the particles will roll to a new equilibrium point [3].

2.2.2 Fluid Model

In our simulations we implement a simple shear cell, with the top boundary moving right and the bottom boundary moving left with speed v_{wall}. Due to the symmetry of the system, we can assume a simple Couette flow velocity profile (fig. 2.4) for the carrier fluid in the cell. To reduce computational complexity, we use an uncoupled hydrodynamic model, with fluid velocities v_f equal to the Couette profile for a given shear rate and Stokes drag (eq. (2.3)) on the grains from the carrier fluid with dynamic viscosity μ. The Reynolds numbers in our simulations

are on the order of 10^{-10} with terminal velocities created by the magnetic forces on particles, making Stokes drag a very good approximation for individual grains.

$$F_d = -6\pi\mu R_i(v_i - v_f) \tag{2.3}$$

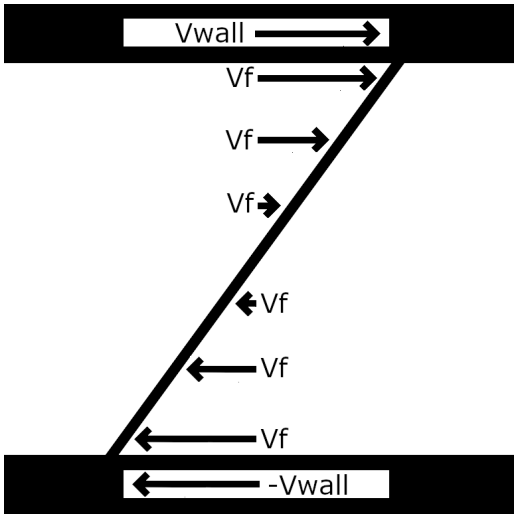

Figure 2.4: A couette flow profile with walls moving at V_{wall} in opposite directions while the fluid velocity, V_f, varies linearly from $-V_{wall}$ to V_{wall} traversing from the bottom wall to the top wall

2.2.3 Magnetic Induction

Paramagnetic grains with susceptibility χ, such as those in an MRF, become magnetized when in the presence of an external magnetic field $\vec{H}$. In the case of a sphere in a uniform magnetic field, the grain is uniformly magnetized, resulting in a dipole moment (eq. (2.4)) [16].

$$\vec{m_i} = 4\pi\frac{\chi - 1}{\chi + 2}R_i^3\vec{H} = C_{m_i}\vec{H} \tag{2.4}$$

The force on the resultant dipoles is found in Equation (2.5).

$$\vec{F}_{m_i} = \nabla \left(\vec{m}_i \cdot \vec{B} \right) \tag{2.5}$$

Notably, there is no force on a magnetic dipole in the presence of a uniform magnetic field. There is a torque term in the magnetic dipole interaction; however, because we use soft magnetic grains, the dipole of the particles will always be aligned with the local magnetic field. The resulting torque will always be zero. Therefore, we omit the magnetic dipole torque equation in our simulation.

In disperse mixtures, it is often acceptable to use the dipole calculated from the background field in simulations (fixed dipole method). However, in the dense mixtures of MRF, the magnetic fields from neighboring grains begin to have a significant effect. To capture the effect of neighboring grains, we implement a mutual dipole method [19]. In the mutual dipole method, all of the grains are magnetized using the background magnetic field. Then the dipoles are recalculated using the background field plus the magnetic fields created by all near neighbors. This calculation is then iterated until the dipole moments of the individual particles converge (eq. (2.6)).

$$\vec{m}_i^{k+1} = C_{m_i} \left(\vec{H}_0 + \sum_{j=1, j \neq i}^{n} \vec{H}_{\vec{m}_j}(\vec{r}_i) \right) \tag{2.6}$$

Increasing the distance neighbors are considered will increase the accuracy of the model while incurring computational costs increasing with the square of the neighbor length. An infinite neighbor-length recreates a 2nd order approximation (terms

higher than dipole ignored) of the entire system. A neighbor length of three particle diameters was used by Sherman simulating non-disperse particle [21]. Han, Feng, and Owen demonstrate that using the mutual dipole method with a two-particle chain, parallel to the background field, increases attractive forces by 77.78% while two particles adjacent to each other, aligned perpendicular to the background field, have their repulsive force reduced by 20.99% [20]. This model converges rapidly, with forces on an L shaped chain of particles converging to within one part in 10^5 within five iterations. Due to the rapid convergence and extremely short timestep from the stiffness in the contact forces, we make the assumption:

$$|(\nabla(\vec{H} \cdot \vec{v}_p)ts| \ll |\vec{H}| \tag{2.7}$$

and only iterate the mutual dipole method once per timestep. This, by the assumption that the motion of a particle in one timestep results in a very small change in the local magnetic field, does not introduce appreciable error, and greatly reduces the computational cost of the mutual dipole method.

2.3 MRF Simulation

In order to test the effects of particle size distribution on MRF simulations, we attempted to recreate the properties of the MRF in Trendler and Bose (fig. 2.5) [2]. Trendler examined the effect of size and bidisperse mixtures on MRF properties. They reported precise curves for their particle size distributions (fig. 2.2) found through laser diffraction, allowing us to recreate their MRF mixtures in LIGGGHTS.

Trendler and Bose do not specify whether their distributions are volume or number densities, so simulations are performed with both interpretations. The two distributions they used to make their mixtures have mean particle size of 1.8 µm and 6.7 µm that were mixed in varying proportions for their experiments.

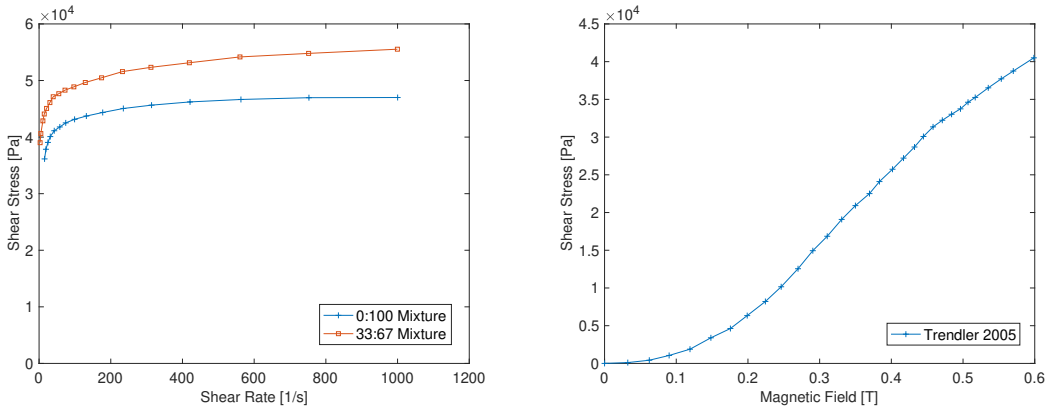

(a) Trendler shear stress vs. shear rate (b) Trendler shear stress vs. magnetic field

Figure 2.5: Trendler and Bose experimental data for (2.5a) shear stress as a function of shear rate for 33:67 and 00:100 mixtures, and (2.5b) shear stress as a function of magnetic field at 100 s^{-1} for a 00:100 mixture.

Due to computation time limitations, we only attempt to reproduce two mixtures from their experimental data; a 00:100 ratio and a 33:67 ratio of small to large particles with a packing fraction/vol.% of $\phi = 0.3$. The parameters for the particle contact forces are given in Table 2.1. Most of the properties are chosen as accepted values for lubricated iron. The Young's modulus notably varies from the accepted value for iron at approximately 1% of the accepted value. Reducing the modulus reduces stiffness and allows for an increased timestep. Chen et al. found that for moduli down to 0.1% of the actual material modulus, the behavior of a granular mixing simulation is statistically unchanged [100]. Moreover, in our simulations, particle chains will be largely under tension, further reducing the dependence on

the Young's modulus.

Young's	Poisson	Restitution	μ_f	μ_r	γ_r	k_c
1 GPa	0.278	0.1	0.1	0.1	0.1	60 kJ/m^3

Table 2.1: Particle properties

The carrier fluid dynamic viscosity is 10 mPa·s. This matches the silicone oil used by Trendler and Bose as their carrier fluid.

Unless otherwise specified, all simulations are carried out in a shear cell 250 µmX250 µmX250 µ with periodic boundary conditions in the X and Y directions, and fixed boundary conditions in the Z direction.

The shear cell is initialized by filling the simulation volume with particles randomly packed with a particle distribution pulled from a digitized version of Trendler's data (fig. 2.2, table 2.2). A constant magnetic field is then applied to the volume in the Z direction, and the particles are allowed to reach an equilibrium state, comprised of particle chains aligned along the magnetic field. Once the particles have settled, the top and bottom 15 µm are frozen to create particle rafts to act as the shearing surfaces. Prior work has used either densely packed, crystalline particle rafts, randomly distributed particle rafts, or monolayers as their shearing surfaces. This tends to create a weaker attachment of particle chains, which slip across the shearing surfaces. By using the magnetic structures, the surface of the raft has strong magnetic field concentrations, which create strong attachment points for the active volume particle chains and are more representative of physical shear cells.

When the initialization process is complete, the top and bottom rafts are

(a) Small particle distribution

Size	0.67 µm	0.78 µm	0.91 µm	1.05 µm	1.25 µm	1.43 µm	1.67 µm	1.96 µm
%	0.0033	0.0160	0.0367	0.0609	0.0863	0.1092	0.1242	0.1326
Size	2.25 µm	2.63 µm	3.03 µm	3.55 µm	4.16 µm	4.97 µm	5.71 µm	7.02 µm
%	0.1329	0.1097	0.0821	0.0540	0.0316	0.0146	0.0057	2.230e-4

(b) Large particle distribution

Size	1.46 µm	1.69 µm	1.98 µm	2.29 µm	2.65 µm	3.07 µm	3.57 µm
%	1e-4	6.155e-4	0.0019	0.0047	0.0117	0.0226	0.0403
Size	4.11 µm	4.89 µm	5.69 µm	6.55 µm	7.66 µm	8.84 µm	10.42 µm
%	0.0646	0.0925	0.1167	0.1327	0.1403	0.1236	0.0985
Size	11.87 µm	13.91 µm	16.63 µm	19.48 µm	24.44 µm		
%	0.0699	0.0446	0.0243	0.0100	5.593e-4		

Table 2.2: Particle size distributions used in simulations digitized from Trendler and Bose

given equal and opposite velocities in the X direction starting with the maximum speed 0.128 µm/µs for 3e6 timesteps to create a fully yielding fluid. The simulation then runs an additional 1e6 timesteps, then reduces the speed successively to 0.064 µm/µs, 0.032 µm/µs, 0.011 µm/µs, 0.008 µm/µs, 0.004 µm/µs, 0.002 µm/µs, 0.001 µm/µs, running for 1e6 timesteps at each shear rate. Timesteps for all simulations are 0.0002 µs, sufficient to keep the simulation timestep below 10% of the hertzian time for all particle sizes used in simulation.

Simulations were run with 600 mT background fields for the two different mixtures with the two different particle distributions. With just the 00:100 mixture MRF, the following additional simulations were run: with a monodisperse particle distribution; with each dimension of the shear cell doubled; without cohesion; with a stationary carrier fluid; and with no rolling resistance. We also ran simulations with the large particle mixture and varying magnetic fields at shear rates down to $100\,\mathrm{s}^{-1}$ corresponding to the shear stress/magnetic field experiment performed by

Trendler and Bose (data recreated in fig. 2.5b).

2.4 Results

2.4.1 Particle Structures and Morphology

Our simulations formed particle chains along the applied magnetic field after approximately 1e5 timesteps. In the case of the lognormal distributions, rope-like chains and thick walls are formed at approximately the diameter and width of the largest particles (figs. 2.6b and 2.6c). These thick chains are stable under shear until they break and are reformed into new morphologically similar chains. In contrast, the monodisperse particles initially form one particle thick, disordered chains, which quickly coalesce into sheets composed of crystallographic domains (fig. 2.6a). The domains rotate under the shear, but do not break and reform as obviously as the chains formed by the lognormal distributions.

Observing the Z-plane cross-sections, it can be seen more clearly that the monodisperse particles form structures that are predominantly one particle wide, particularly after they have been sheared (fig. 2.7a). The structures also align themselves prominently along the direction of shear, with the crystallographic sheets seen in the Y-Plane cross-sections forming roughly parallel bands across the Y direction. The lognormal distributions show considerably less banding and continue to exhibit thickness similar to the largest particle diameter (figs. 2.7b and 2.7c). The gaps between structures also appear as approximately the same width as the largest particles in the lognormal distributions and single particle wide in the monodisperse

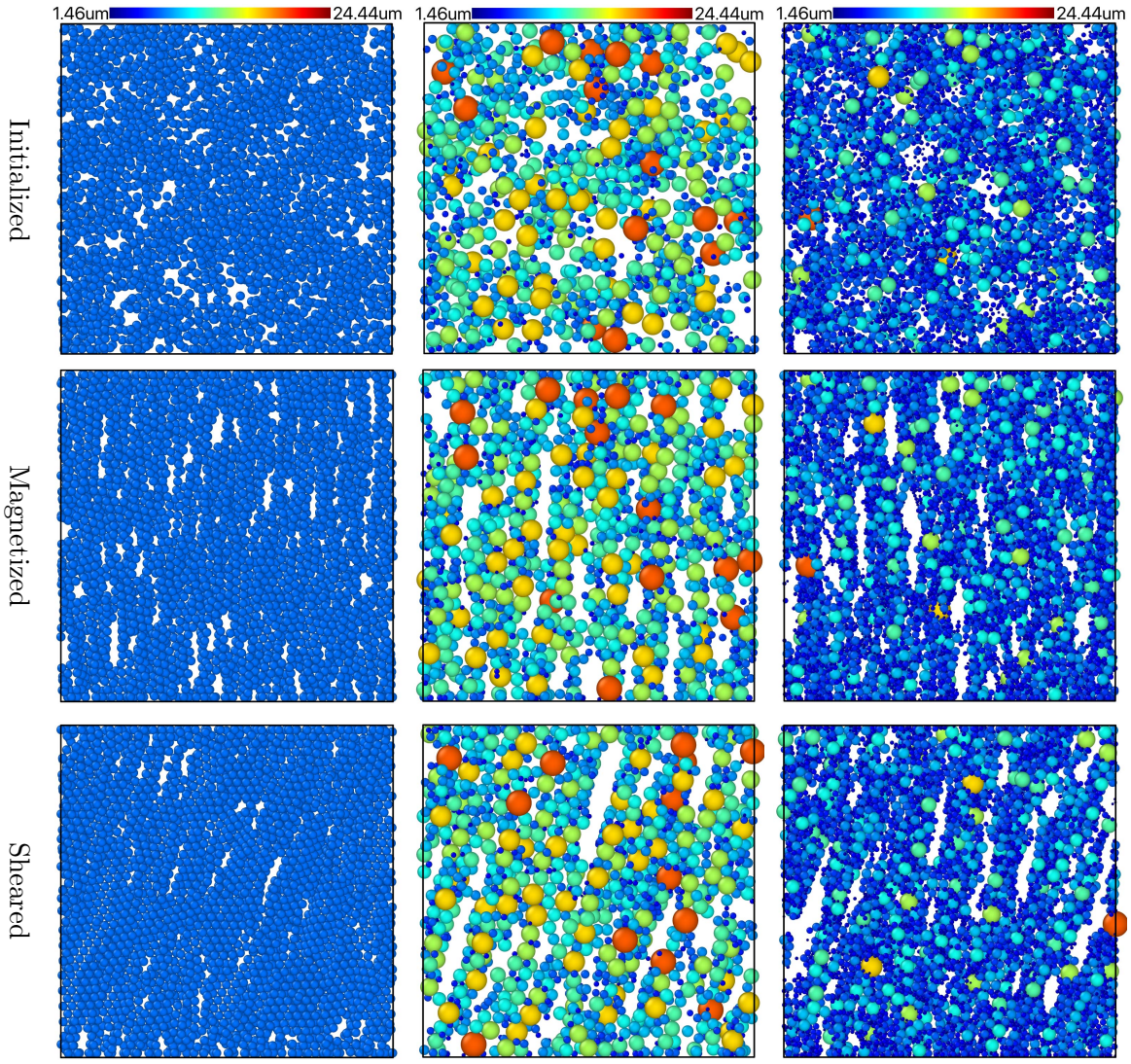

(a) Monodisperse (b) Number Density (c) Volume Density

Figure 2.6: 25 µm thick, center, Y-plane cross-sections of simulated 00:100 mixture. The top sections are initialized with no magnetic fields. The middle sections are magnetized in a $\vec{B} = 600\,\mathrm{mT}\hat{z}$ field. The bottom sections are sheared with $\gamma = 0.93$ of simple shear in the X direction at a shear rate starting at $\dot{\gamma} = 1100\,\mathrm{s}^{-1}$ and finishing at $590\,\mathrm{s}^{-1}$. Figure 2.6a shows monodisperse 6.7 µm particles forming vertical chains when the magnetic field is applied. As the cell is sheared, the disordered chains begin to form sheets with crystallographic domains. Figure 2.6b shows a lognormal, number density distribution. During the initial magnetization, the structures formed are thick chains tending towards the diameter of the larger particles, sometimes coming together to form large clumps. As the cell is sheared, the chains also shear over with the cell but remain morphologically similar to the unsheared chains. Figure 2.6c shows a lognormal, volume density distribution. The initial magnetization still produces structures with a thickness comparable to the larger particles despite there being relatively fewer large particles. The chains again shear along with the cell though some additional clumping occurs.

case.

In the 33:67 distributions many of the same trends continue (fig. 2.8). With the addition of smaller particles, the particle chains become tighter and more numerous, with smaller and more numerous gaps particularly pronounced in the volume density distribution. The 33:67 mixture volume distribution is the first simulation where the particle chains are smaller than the largest particle diameters and instead tend towards the diameter of the more numerous, medium-large diameter particles. The volume density mixture also creates smaller and more convoluted structures than any of the other simulations with considerably smaller gaps between structures (fig. 2.9). There is virtually no plane formation along the shear direction in the case of the volume distribution.

One interesting feature is the way that the chains behave at large strains. Past works have characterized the chains as reaching a critical strain where the tensile stress in the chains exceeds the magnetic forces, at which point the chains break and then reform with other broken chains with lower shear and strain [21]. In our simulations using particle distributions, the deformation and destruction of chains are considerably less distinct. During shear, the gaps between chains shrink. As the shear angle of the chains increases, the component of the background field across the chains increases. Neighboring chains then link together and the attachment points split into new, lower shear chains (fig. 2.10).

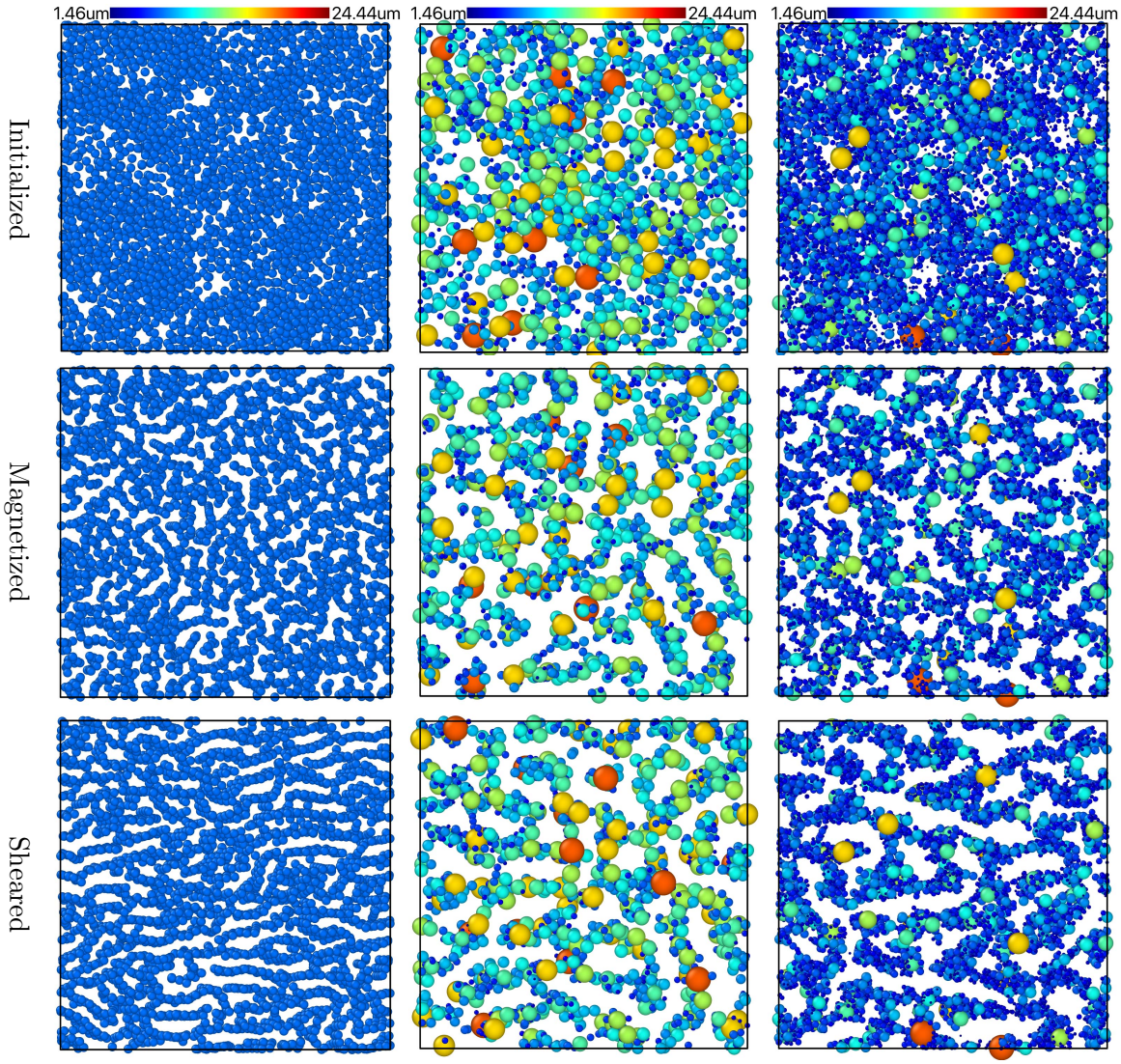

(a) Monodisperse (b) Number Density (c) Volume Density

Figure 2.7: 25 µm thick, center, Z-plane cross-sections of simulated 00:100 mixture. The top sections are initialized with no magnetic fields. The middle sections are magnetized in a $\vec{B} = 600\,\mathrm{mT}\hat{z}$ field. The bottom sections are sheared with $\gamma = 0.93$ of simple shear in the X direction at a shear rate starting at $\dot{\gamma} = 1100\,\mathrm{s}^{-1}$ and finishing at $590\,\mathrm{s}^{-1}$. Figure 2.7a shows monodisperse 6.7 µm particles forming extremely convoluted, single particle wide structures when the magnetic field is applied. They then straighten into single particle wide lamellar structures, aligned with the direction of shear as the cells are sheared. Figure 2.7b shows a lognormal, number density distribution. During the initial magnetization, the structures formed are thicker tending towards the diameter of the larger particles. As the cell is sheared, there is some alignment along the direction of shear, though the formation of lamellar sheets is muted. Figure 2.7c shows a lognormal, volume density distribution. The initial magnetization still produces structures with a thickness comparable to the larger particles. There is little alignment into lamellar structures during shearing.

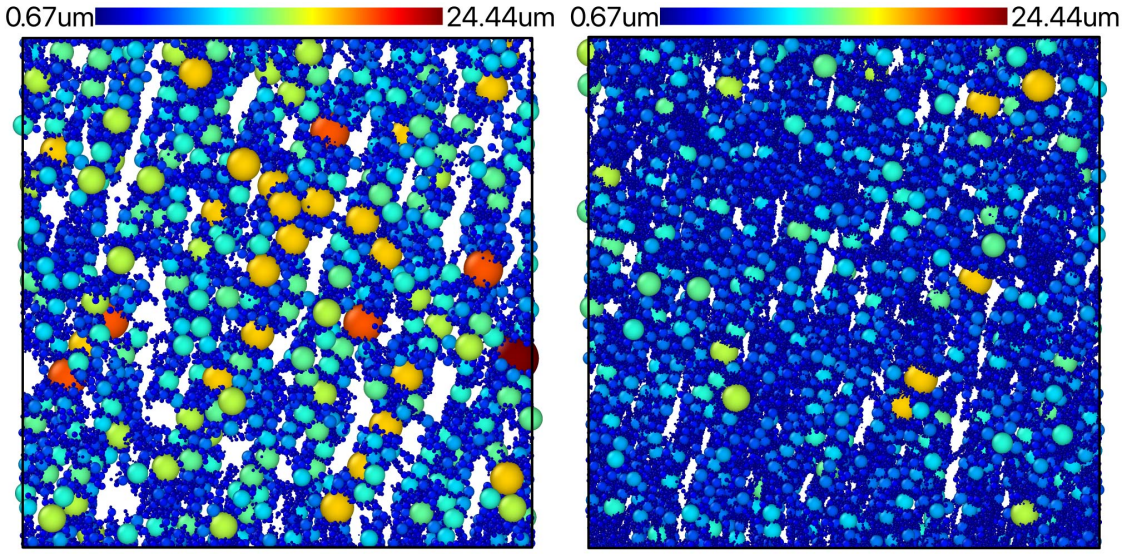

(a) Sheared Number Density (b) Sheared Volume Density

Figure 2.8: 25 µm thick, center, Y-plane cross-sections of simulated 33:67 mixture, magnetized in a 600 mT field and sheared with $\gamma = 0.93$ of simple shear at a shear rate starting at $\dot{\gamma} = 1100\,\mathrm{s}^{-1}$ and finishing at $590\,\mathrm{s}^{-1}$. (fig. 2.8a) The number density distribution produces strands and clumps similar morphologically to those from the volume distribution from the 00:100 mixture. (fig. 2.8b) breaks from the trend and has structures somewhat smaller than the largest particles with more cross linking from the smallest particles and more numerous and smaller gaps between strands.

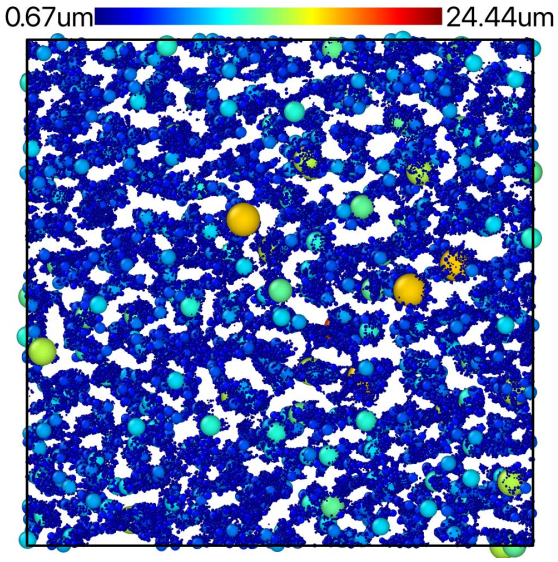

Figure 2.9: Sheared, 33:67, Volume Density Distribution Z Cross-section. The volume density distribution again shows the largest deviation from the other distributions, with much finer features. The labyrinthine behavior of the other distributions is replaced by small, disjoint chambers. No alignment with the direction of shear is apparent.

2.4.2 Yield Stress

To compare the simulation results to the data from Trendler and Bose, the force on the upper raft particles was stored every 5K time steps, summed and divided by the area to calculate the stress (eq. (2.8)).

$$\tau = \frac{1}{X_{dim} Y_{dim}} \sum_{i \in raft} F_i \tag{2.8}$$

The last 100 calculated shear stresses for each shear rate were averaged to obtain the shear stress at each shear rate. Figure 2.11 shows the results of four different initial seeds for the particle packing using the number density distribution, compared against the Trendler and Bose experimental results. Simulations with number par-

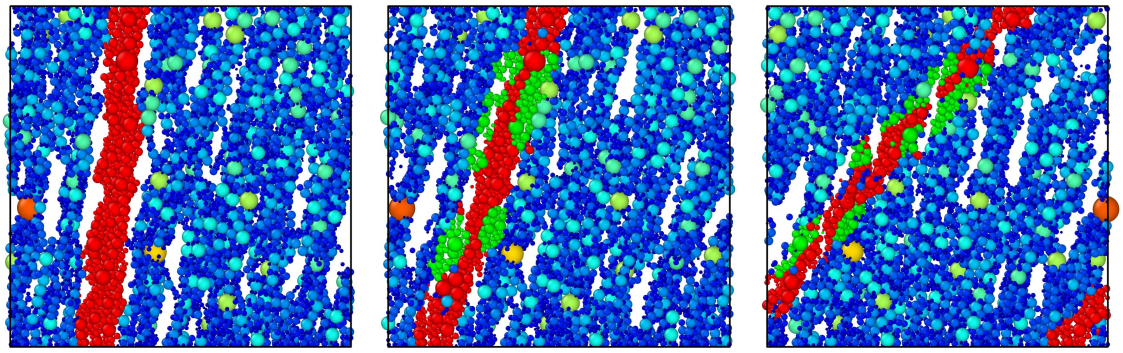

(a) Unsheared particle chain, highlighted in red

(b) Sheared, attachment points highlighted in green

(c) Chain, integrated into new chains

Figure 2.10: The progression of a chain of particles (red, fig. 2.10a) from a disjoint, low shear pillar to a higher shear chain, which then attaches itself to adjacent chains (green, fig. 2.10b). The attachment points then go on to form sections of a new set of chains (fig. 2.10c). Note that the new chains have a pattern of red sandwiched between two layers of green, indicating that a left side and right side attachment point go on to form the top and bottom of a chain segment. (Y cross-section 00:100 volume density)

ticle distributions for 00:100 mixtures were computationally inexpensive and agreed with Trendler and Bose's experimental data very well. The four simulations were run using the standard shear cell size and the 00:100 number distribution mixture. The different seeds were fairly consistent, though Seed3 had somewhat larger deviation from the experimental data, and showed some morphological differences (fig. 2.11a). Still, the maximum standard deviation in the simulated shear stress for the four seeds was 7.16% of the mean shear stress, at a shear rate of $36.4\,s^{-1}$. The experimental data was within one standard deviation of the mean of the four seeds at all data points but the lowest shear rate, $9\,s^{-1}$, which was too high in the simulations (fig. 2.11b). In addition to the regular size shear cells, two additional simulations were run with a 500 µmX500 µmX500 µm shear cell, to check the sensitivity to the shear cell size in simulations (fig. 2.12). The double sized shear cell

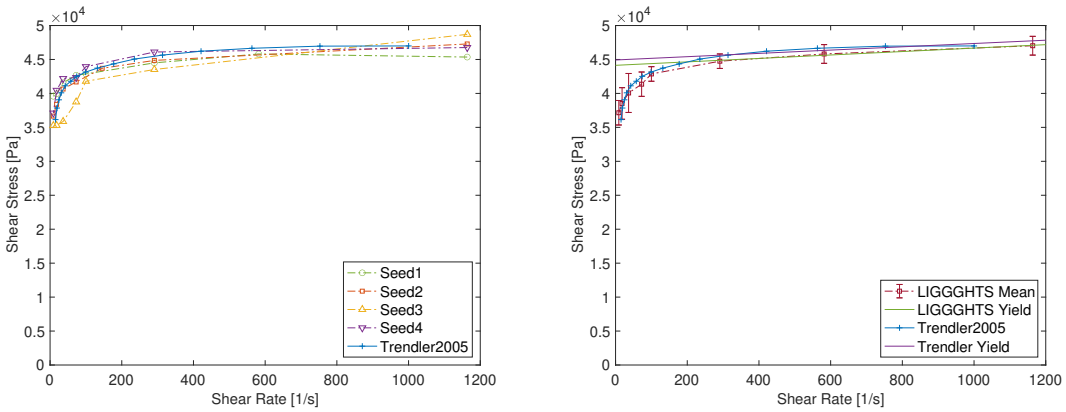

(a) Trendler and simulation shear stress vs. shear rate for multiple 00:100 seeds

(b) Trendler and mean simulation shear stress vs. shear rate for 00:100 mixture including fit lines for yield stress

Figure 2.11: Plots of shear stress obtained from simulations compared to Trendler and Bose experimental data at 600 mT showing: (fig. 2.11a) Shear stress for several different initial particle packing random seeds being sheared at rates ranging from $\dot{\gamma}$ =1100 s^{-1} to $\dot{\gamma}$=9 s^{-1}. (fig. 2.11b) Mean shear stress from the multiple seeds in fig. 2.11a. Linear regressions for the shear rates above 200 s^{-1} are used to calculate the yield stress.

simulations produced similar results to the 250 µm cells. The volume distribution, in addition to being considerably more computationally expensive, does not match the experimental results as well as the number density distributions (fig. 2.13).

Yield stress was calculated using a linear fit to data points with shear rates $\dot{\gamma}$ >200 s^{-1} (fig. 2.11b). The yield stress and errors are shown in table 2.4. The mean yield stress for all 00:100 number density simulations was 43.9 kPa compared to 44.9 kPa in Trendler and Bose's data, and the standard deviation in yield stress for these data sets was 1.28 kPa or 2.9% of the mean yield stress. The volume distribution produced a 49.6 kPa yield stress.

Our simulation with the 33:67 mixture, using number density distributions, was able to capture the shear stress enhancement found experimentally in bi-disperse

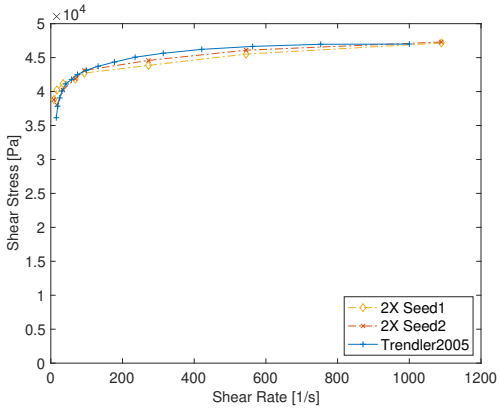

Figure 2.12: Trendler and simulation shear stress vs. shear rate for two 00:100 double size shear cell simulations with number density distributions. The simulations closely match those from the shear cells with half the side lengths.

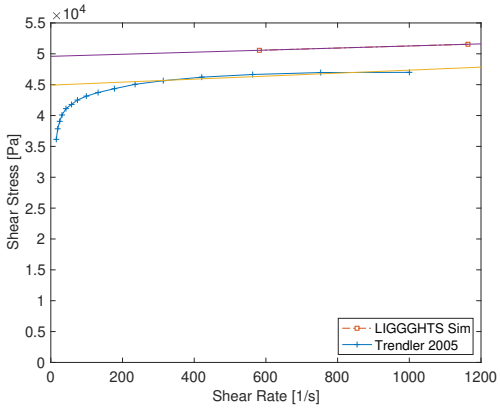

Figure 2.13: Trendler and simulation shear stress vs. shear rate for a 00:100 volume density distribution, only run 5e6 timesteps due to computation costs. The volume density distribution over estimates the yield stress by 10%.

Data Set	τ_y	% Error
00:100 Mix		
Trendler	44.9 kPa	NA
Seed1	44.7 kPa	0.4%
Seed2	44.1 kPa	1.9%
Seed3	41.8 kPa	7.0%
Seed4	45.9 kPa	2.1%
Mean	44.1 kPa	1.8%
2X Seed1	43.0 kPa	4.2%
2X Seed2	44.0 kPa	2.1%
Average	43.9 kPa	2.2%
Volume den.	49.6 kPa	10.4%
33:67 Mix		
Trendler	50.8 kPa	NA
Number den.	56.3 kPa	10.8%

Table 2.4: Yield stress for simulations at 600 mT: with four number density random seeds, the mean shear stresses from the four regular size number distributions, two double sized number density seeds, the average of the calculated yield stresses from all number density simulations, and a volume density simulation.

MRF mixtures (fig. 2.14). The enhancement to the shear stress was somewhat over-pronounced however, overshooting the experimental value by approximately 10%. There was also some reduction in the knee where the shear stress drops off at low shear rates. Simulations using volume distributions for the 33:67 mixture were too computationally expensive for us to produce a full shear profile in simulations and are only examined qualitatively in this work.

In addition to the shear stress vs. rate simulations, we also simulated various field strengths and measured the resultant shear stress at $100\,\mathrm{s}^{-1}$. Two seeds were used, and they produced very consistent shear stresses with a similarly shaped trend to the experimental data, however the deviation from experiment is considerably larger than the yield stress data, growing as the magnetic field strength approaches 300 mT, with a maximum error of 31%. At 32 mT the error also spikes, though the

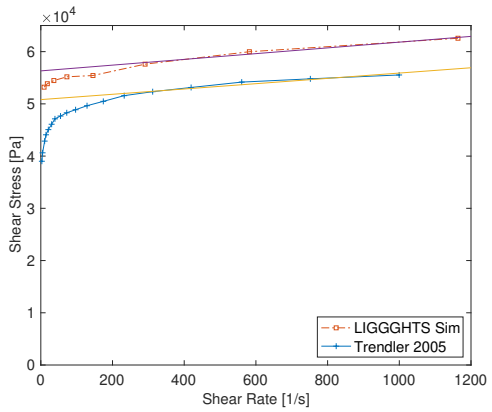

Figure 2.14: Trendler and simulation shear stress vs. shear rate for a 33:67 number density distribution

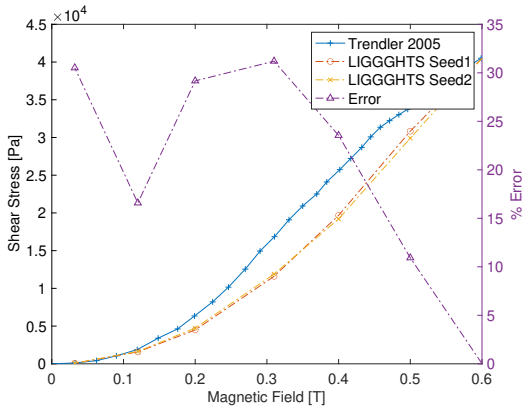

Figure 2.15: Trendler and simulation shear stress vs. magnetic field for a 00:100 number density distribution. The shape of the trend is comparable, though the simulated shear stress droops in the middle compared to the experimental data from Trendler and Bose. The deviation from experimental is also large near zero, though the magnitude of the shear stress is very low at low fields.

magnitude of the shear stress is very low at that point, therefore, small deviations in the magnetic forces on the particle raft can create large errors in the simulated shear stress (fig. 2.15).

To examine the sensitivity of the simulated shear stresses to the contact force model we ran simulations without some of the contact forces enabled. These simulations were run using a 00:100 mixture with a number density particle distribution

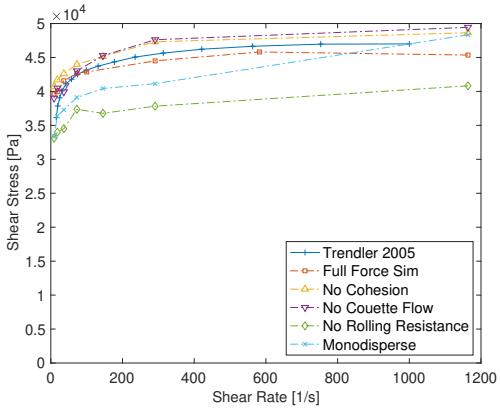

Figure 2.16: 00:100 Number density distribution simulations run with various model forces neglected. Neglecting rolling resistance or or using a monodisperse particle distribution resulted in reduced yield stress and some morphological differences in the shape of the shear rate/stress curve. Removing cohesion or using a stationary background fluid (though still including Stoke's drag) produced slightly increased shear stress but remained very similar morphologically to the full force simulations.

and were all run using the same initial particle packing seed. Eliminating the rolling resistance caused the largest reduction in shear stress of any of the forces and resulted in a less smooth roll-off at low shear rates. Using a monodisperse mixture resulted in a high initial shear stress that dropped off quickly. Simulations run using a stationary background fluid with Stoke's drag had slightly increased shear stress, as did simulations run without cohesion (fig. 2.16). The closest match to the experimental data came from the simulations with all the forces considered, demonstrating the importance of maintaining a high fidelity contact model in MRF simulations.

2.4.3 Computational Costs

Simulations for the 00:100 mixture with 250 µm cube shear cells were run on the Deep Thought 2 High Performance computing cluster at University of Maryland consisting of dual Intel E5-2680v2 processors and 128GB of 1866MHz DDR3 memory

per node. The number density distributions simulations were run with 18 cores on a single node. The simulations used approximately 15MB of RAM per core and took 4.64 ms per timestep with about 12k particles. The average number of neighbors used to calculate magnetic interactions, per particle, using a neighbor length of 8 µm plus the radii of the particles being evaluated as neighbors, was approximately 100. The monodisperse 6.7 µm particle simulations were also run on 18 cores, using approximately 29MB of RAM per core, and took 3.90 ms per timestep with approximately 30,000 particles. Despite the larger particle counts, the absence of smaller particles resulted in only 25 neighbors per particle with which to calculate magnetic interactions. Volume density distribution simulations are considerably more computationally intensive because of the larger number of small particles in the simulation. The volume density simulations ran on 60 cores on three nodes and used 17MB of memory per core taking 31 ms per timestep to run the simulations with ≈60,000 particles. On average, approximately 500 neighbors per particle were used to calculate magnetic interactions. Double sized shear cell simulations with number density distributions were run on a standalone workstation with dual Intel E5-2699V4 processors and 128GB of 2400MHz DDR4 RAM. The simulations used 27 cores and 17MB of RAM per core, taking 30.1 ms per timestep with ≈93,000 particles. An average of 100 neighbors per particle were used for magnetic interaction calculations.

Simulations for the 33:67 mixture were run on the standalone workstation. The number distribution used 40 cores and 33MB per core for a runtime of 72 ms per timestep with ≈200,000 particles. On average, approximately 220 neighbors

per particle were used for magnetic interactions. For the volume distribution, the neighbor length was required to be shortened to 2 µm plus the radii of the particles to prevent neighbor list overflows. On 40 cores, 80MB per core were used, taking 1152 ms per timestep to run the simulation with ≈910,000 particles and an average of approximately 300 neighbors per particle. Due to the computational resources required for the volume distribution, the simulation was only run for a single shear rate to observe the morphology of the structures and to analyze how that shear stress compared to the values for the same shear with a number density distribution.

2.5 Conclusion

Including realistic contact forces and particle size distributions has allowed us to accurately model magnetorheological fluids with higher fidelity than previous efforts. We have identified qualitative differences in the behavior of MRF composed of a distribution of particle sizes compared to the behavior of more uniformly sized mixtures, such as the resistance to the formation of sheets, lack of crystalline structures, and the reorganization of particle chains under shear. We have also captured the yield stress enhancement effect of MRF composed of bidisperse mixtures of particles. The tradeoff to the high-fidelity model is the potential for much higher computation times in the case of particle volume size distributions which contain many, much smaller particles, increasing the total particle number and the number of close neighbors included in magnetic interaction computations. For the 33:67 mixture, considerably more computing resources would need to be devoted

to get data for volume distributions. Despite the computational limitations, the increased fidelity improves our understanding of the microstructures and behaviors of magnetorheological fluids, some of which are contrary to results obtained from uniform particle sizes. Furthermore, the LIGGGHTS base code allows for the implementation of arbitrary MRF mixtures, allowing for rapid evaluation of new formulations. We've also matched experimental data for bulk properties of MR fluids, providing high confidence validation of the magnetic model and its integration with the LIGGGHTS framework. Additionally, the model has been used to simulate non-standard MRF operation modes. The behavior of an electropermanent magnet-based jamming, magnetorheological valve was replicated using LIGGGHTS simulations with the same magnetic model as was used in this work. [101].

Due to the use of the LIGGGHTS open source framework, it is possible to easily integrate new force models into simulations, creating a magnetic, granular simulation testbed, including a coupled fluid model using the supported CFDEM framework which integrates LIGGGHTS with OpenFoam. In keeping with the open source nature of LIGGGHTS the source code, for our magnetic interaction model, will be released for public use at https://github.com/TJLeps/LIGGGHTSwMAGNETICS.

Chapter 3: Design and Simulation of a Jamming Magnetorheological Valve

This chapter contains material published in: T. Leps, P.E. Glick, D Ruffatto III, A Parness, M T Tolley, and C Hartzell. A Low-Power, Jamming, Magnetorheological Valve using Electropermanent Magnets Suitable for Distributed Control in Soft Robots. *Smart Materials and Structures*, 29(10):105025, Sep 2020. [101]

3.1 Introduction

3.1.1 MRF Valves

Magnetorheological fluid (MRF) is an attractive working fluid for a number of applications due to the ability to modify its rheological properties rapidly, in-situ using a magnetic field [26]. MRF is comprised of two primary components: iron particles and a carrier fluid such as mineral oil or silicone oil. Optional additives such as surfactants and detergents can also be added to enhance MRF properties [65]. With no magnetic field applied, the iron particles remain in suspension and flow past each other, with minimal interference, allowing the fluid to flow, behaving as a slightly shear thinning liquid. When a magnetic field is applied, the iron particles

align to the field and form chains, which resist flow. In the magnetized state, MRF can be modeled as a Bingham plastic[102], solid up to a critical yield shear stress and flowing like a fluid above that yield stress (Figure 3.1c). Previous works have used MRF for variable stiffness devices, shock absorption, and even robotic grasping and climbing [103, 104, 105].

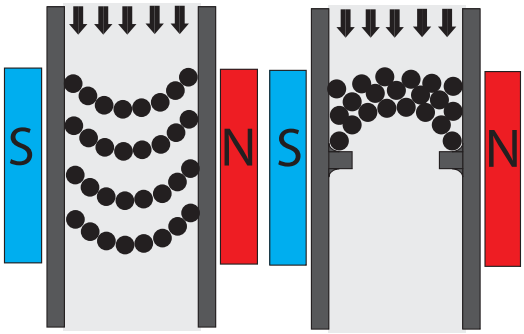

(a) Traditional MRF valve (b) Jamming MRF valve

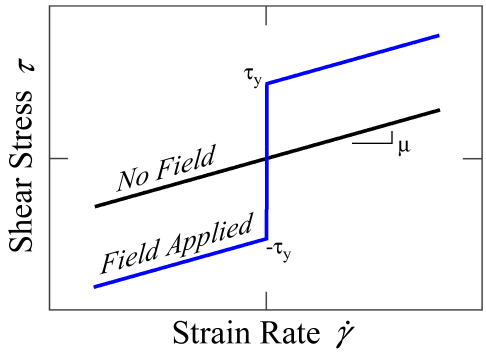

(c) Magnetorheological fluid stress strain curve, modeled as a Bingham plastic, with no flow below τ_y [102].

Figure 3.1: A traditional MRF valve (a), forms chains across the magnetic field, which need to be broken to flow, resulting in a Bingham Plastic behavior (c), stable below and flowing above a critical yield strength. A jamming valve (b) forms stable arches across a restriction under pressure. Increasing pressure further jams and stabilizes the structure.

The yield stress of MRF increases with magnetic field strength until saturation, at which point increasing the magnetic field does not significantly increase

the yield stress. The maximum yield stress for MRF is ∼100 kPa, at saturation of ∼700−1000 mT [26, 64, 65]. For typical MRF valve designs, when the magnetic field is turned on, the flow will be stopped at pressures below and will begin to flow at pressures above the yield stress, τ_y, times the effective length, L, divided by the effective diameter of the valve, d [71].

$$P_{flow} \approx \frac{\tau_y L}{d} \tag{3.1}$$

The maximum holding pressure for an MRF valve based on this yield stress is therefore limited to about ∼100 kPa of pressure in a compact valve with length on the same order as width, and requires a strong magnetic field to realize these pressures.

A different mode of operation, Magnetic Gradient Pinch (MGP) valves, are able to hold much higher pressures for a given magnetic field and valve size [70]. They operate by taking advantage of the granular nature of the MRF rather than the bulk properties. A strong magnetic gradient near the walls of the valve attracts iron particles, causing them to clump against the wall, reducing the effective diameter of the valve. Granular flows, such as in an MRF, are subject to a behavior known as jamming when they flow through a constriction [106]. When a suspension jams in a constriction, the particles form a stable dome across the passage, mechanically stopping the flow of the grains and carrier fluid (Figure 3.1). In most applications jamming is avoided, as it can lead to irreversible stoppages. However with MRF, due to the variable effective diameter and cohesion in an MGP valve, it is possible to

design a valve around the formation of jams that can be induced and reliably reversed by the addition and removal of a magnetic field [70]. When the effective constriction diameter is a small multiple of the grain diameter, a jamming transition occurs. Once jammed, the valve can hold an extremely high pressure, up to 20 000 kPa, as the jam is stabilized with increasing pressure. Using larger, e.g. 100 µm, particles in MGP valves, rather than the more typical 1 µm-10 µm particles, encourages the jamming behavior by reducing the width of the orifice relative to grain size [70].

Current MRF valve designs require on the order of one amp of current to actuate using an electromagnet. This results in $\sim 1\,\mathrm{W} - 100\,\mathrm{W}$ of power in order to maintain their state, using conventional electromagnets [70, 75]. The bulk of the coils and cores required to maintain the field, combined with the power dissipation required to prevent overheating make MRF valves too large for many applications. Furthermore, the continuous power consumption of MRF valves requires increased energy storage for mobile applications. Due to their large size and power requirements, MRF valves have been limited to use in large structures and machines, such as the automotive industry [26, 65, 75]. Small scale, portable devices have not been practical.

Gilpin and Knaian developed a novel electromagnet, an electropermanent magnet (EPM), for use in miniature robotic building blocks ("pebbles") [79, 80]. These magnets are able to switch between an "ON" state, with a strong external magnetic field, and an "OFF" state, with no external field with a short duration current pulse. The EPMs require no continuous power to maintain their state after being switched. By replacing the electromagnets in a jamming MRF valve with an EPM, this work

miniaturizes MRF valves, shrinking them by an order of magnitude and reducing their average power consumption (assuming a single actuation per second) by three orders of magnitude (Figure 3.2).

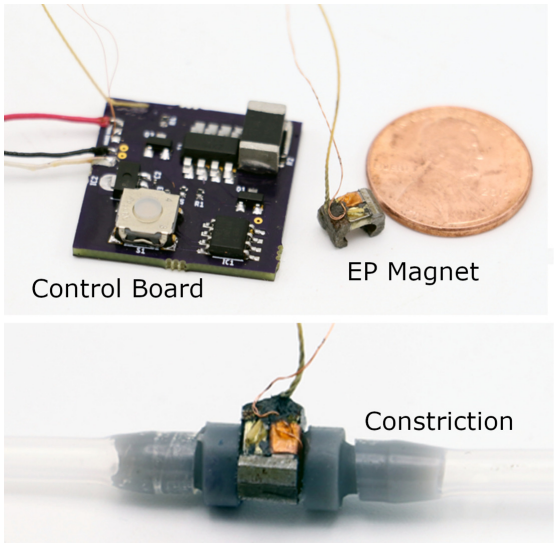

Figure 3.2: A small, low-power, magnetorheological valve. The electropermanent magnet weighs only 0.476 g. The magnet is comprised of an alnico magnet wrapped in copper wire, adjacent to a neodymium magnet, between two iron end caps. A small circuit can drive several of the magnets, and it takes no power to hold the OPEN or CLOSED state (top). This magnet can be placed around a constriction, outside of the flow, to create a valve that holds more than 415 kPa. We use custom fittings with internal constrictions for our valves (bottom).

3.1.2 Soft Robot Valving

Efforts to design soft robots with distributed valving have succeeded in producing multi-segmented designs with novel behavior [107, 108, 109, 110]. Increasing the number of independently controlled actuators in a soft robot can improve dexterity, flexibility, and positional accuracy [111, 112, 113], yet many elastomeric robots consist of only a few actuated degrees of freedom. Each fluidic actuator requires additional infrastructure (tubing, power, valving, and control) to facilitate

independent control. The complexity and size of this additional infrastructure has prohibited the use of many (e.g. $\mathcal{O}(10)$ to $\mathcal{O}(100)$) discrete actuators in a single robot, limiting their use to relatively simple behaviors [114]. However, with any un-tethered robot or when many valves are distributed along a robot, issues such as mass, size, price, complexity, and power become paramount [115, 116, 117]. The range of existing approaches to valving illustrates this need, with actuators designed using pressure-actuated soft membrane valves [118, 119, 120], electrorheological fluid valves [121, 122, 123], and commercially available pneumatic solenoid valves [108, 109]. Pressure driven valves require additional pressure lines for controlling the valve. These valves can be multiplexed to drive a greater number of valves than the number of control lines. However, these valves are difficult to distribute across a soft robot and multiplexing alleviates but does not solve the issues introduced by having to integrate large bundles of tubing lines into the robot [111]. Commercially available pneumatic valves do not scale well due to size, power consumption, and price [108, 109]. Electrorheological fluid valves are a compelling solution, but require high activation voltages (i.e. $\sim$kVs), consume power continuously, and require tight constrictions in their flow path that adversely effect fluid flow rate [124] (see Table 3.1 for a comparative review). An ideal valve is small, simple to control, low mass, low cost, and low power. MRF valves, miniaturized with EPMs, use a smart material, similar to electrorheological fluid valves, but are able to operate at lower voltages and with larger orifices. To the best of our knowledge, MRF valves have not previously been explored for use in soft robots.

In this paper we introduce a low-power MRF valve, using electro-permanent

Valve Type	Size (mm)	Vol. (mm^3)	Steady-State Power (mW)	Mass (g)	Maximum Pressure (kPa)	Price (USD)	Special Considerations
Magnetorheological with electropermanent magnet (this work)	4×4×6.5	104	0	0.476	> 415	7.32	Requires use of MR fluid as working fluid
Electropermanent Air Valve [107]	38x38x7	10,108	0	5	30 *approx.*	not reported	Does not fully arrest flow
Addressable Pneumatic Valve [118]	14×14×6	1,176	0	5 *est.*	35 *approx.*	not reported	Pressure regulated, requires complicated control
Bistable Membrane [119]	27x27x34	24,786	0	8 *est.*	80 *approx.*	not reported	Pressure regulated
Electrorheological Valve Soft, 3D Printed [121]	30×10×10 *approx.*	3,000 *approx.*	< 1,000	< 10	275	not reported	Requires > 1 kV supply Requires use of ERF as working fluid
Electrorheological Valve Plate Style [122]	2.5×2.5×15	93.75	< 1,000	< 10	1,000	not reported	Requires > 1 kV supply Requires use of ERF as working fluid
Latching micro-solenoid valve (Lee Company)[108]	6×7×13	546	0	2.5	70	375	
Mini-solenoid valve (Parker-Hannifin)[109]	8×12×23	2,208	1,000	4.5	700	39	

Table 3.1: Review of several representative miniature valves used in soft robots. Pressure regulated valves use another pressure source as the control input. Electrically driven valves tend to be large and power hungry. The high-voltage supply and constant power draw of Electrorheological Fluid (ERF) valves pose challenges that are well addressed by our MRF valve. Not all sources cite the maximum pressure that their valve can hold, and for these we use the highest value reported in the paper.

magnet (EPM) actuation, as a valve for soft robots that can scale to many segments effectively. Our valve should be suitable for other applications in which size and power concerns prohibit traditional valves and MRF can be used as the working fluid, such as bypass valves for MR dampers.

We begin by presenting the design and fabrication of an MR valve (Section 2), discussing the EPM, use of constrictions, and choice of MRF. In Section 3 we present the experimental design for testing the valves. Section 4 compares a large range of independent variables to select working valves, then evaluates stopping pressure and flow rates for the successful valve designs. Included is a demonstration of MR fluid driving a soft robot, and the MRF valves providing control of independent actuators. We follow with a discussion of the results and practical considerations (Section 5)

and a conclusion (Section 6).

3.2 Design of a Magnetorheological Valve

3.2.1 Magnetorheological Fluid

The choice of the carrier fluid will determine the viscosity, thermal properties, and conductivity of the MRF. If the carrier fluid is too inviscid, the iron will quickly settle out of suspension. If the carrier fluid is too viscous, the flow rate will be unacceptably low. For this application, thermal and electrical properties are not relevant, so we used mineral oil as our carrier fluid due to its advantageous viscosity characteristics and low cost.

Jamming behavior is appealing in our application as we do not require flow modulation and it results in a smaller magnetic field density requirement for a given holding-pressure, allowing us to use smaller magnets, and to hold higher pressures than we would be able to with a shear valve. In addition to a more traditional 10 µm iron powder, a coarser, 325 mesh iron powder (corresponding to a maximum particle diameter of 44 µm) is used to encourage jamming.

Increasing either the volume percentage or the size of the iron particles increases the yield stress, fluid viscosity, probability of jamming, and magnetic permeability of the MRF. A successful MRF valve requires a fluid that jams consistently, unjams reliably, and maintains a sufficient flow rate for robot actuation. We test several mass percentages and particle sizes to experimentally select between these variables. Furthermore, additives may be used to change the magnetorheological be-

havior, such as the the off-state viscosity, and settling time of the fluid. Surfactants, such as oleic acid (used in this work), act to disperse iron particles by attaching to the grains at the hydrophilic end of the molecule, while pulling the grains into suspension with the lipophilic end. The result is that even a very small volume fraction of oleic acid drastically reduces the unmagnetized viscosity for a given iron fraction.

3.2.2 Electro-permanent Magnet

We fabricated our EPMs similar to those presented by Gilpin et. al. and by Knaian [79, 80]. EPMs have a permanent neodymium magnet adjacent to an aluminum-nickel-cobalt (alnico) magnet sandwiched between two iron end caps. The alnico magnet is wrapped in thin gauge wire and connected to an H-bridge circuit that can drive current in either direction through the wire (Figure 3.2). The alnico magnet has a much lower coercivity than the neodymium magnet, allowing it to be magnetized by a short current pulse, while the neodymium magnet is unaffected. The remnant field for alnico 5 and N42 neodymium magnets are very similar $\sim 1.3\,\mathrm{T}$, so when fully magnetized, the two magnets are roughly equal strength. If the alnico magnet is magnetized parallel to the neodymium magnet, their field lines both exit the magnets through the north poles, travel up into the iron end cap, then down to the other end cap and up into the south pole of the magnets. When the alnico magnet is magnetized anti-parallel to the neodymium magnet, the field lines travel up from the north pole of the neodymium magnet, into the iron end, then back

down through the south pole of the alnico magnet, into the other end cap, and back into the neodymium magnet. The field lines don't escape from the end caps, and so there are no external magnetic fields (Figure 3.3). The alnico magnets in our work are wrapped in 80 turns of 42 gauge magnet wire. The alnico and neodymium magnet, both 1.6×1.6×3.2 mm, are sandwiched between iron end caps, adjacent to each other, and bonded with cyano-acrylate adhesive. Excluding the control circuit, the EPM is 4×4×6 mm, 0.476 g, and costs $7.32 USD per device at quantity 100 (Figure 3.2). Switching the state of the alnico magnet is done through a 100 µs pulse, which has a maximum power of ∼ 150 W and uses ∼ 10 mJ of energy.

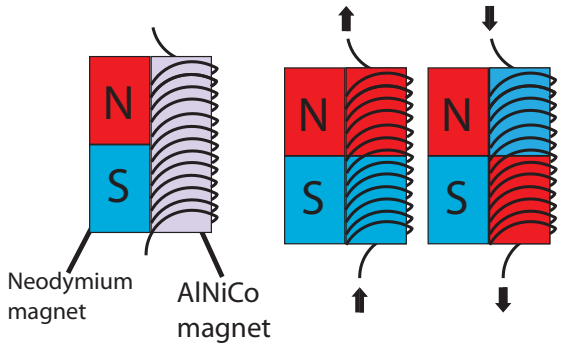

(a) Unenergized (b) On (c) Off

Figure 3.3: The behavior of an electropermanent magnet. The neodymium magnet has a permanent orientation. However, the alnico can be magnetized via a short burst of current to have its field either aligned with (*b*) or opposed to (*c*) the neodymium magnet. By realigning the alnico magnet, the EPM can be switched to either have a strong external magnetic field (*b*) or a negligible external magnetic field (*c*), and will hold this state with no quiescent power draw.

3.2.3 Magnet bracket design

A primary design goal is to minimize the size of the magnet. A smaller magnet reduces the valve size, allowing for more compact and softer robots. It also requires

less energy to actuate a smaller magnet [80]. The energy for actuation is stored locally on the control board, in a capacitor, therefore reducing the energy requirement also reduces the capacitor and control board size. However, with a small magnet it is imperative to make efficient use of the magnetic field density to sufficiently magnetize the iron in the MR fluid. Magnetic fields can be analyzed much like an electric circuit, due to the zero divergence property, where field lines flow between the north and south poles like current in an electric circuit. The field will tend to concentrate between areas of low magnetic reluctance (i.e. shorter distances and materials with higher magnetic permeability). Increasing the field density increases the yield strength and jamming probability of the MRF.

The end caps on the EPM assembly guide the magnetic field lines to both ensure an effective CLOSED state, and to maximize the field density in the active fluid portion of the valve during the OPEN state. Figure 3.4 shows three possible magnetic circuit designs. Configuration A is an inefficient use of the magnetic field, as many field lines flow from N to S without being guided through the MR fluid inside of the tubing and failed to achieve meaningful results prior to formal lab testing. Both configuration B and C were fabricated and tested. Both use mild steel brackets bonded to the ends of the EPM. Configuration B uses straight iron brackets extending out to the center of the fluid flow. This method is well suited for thin walled tubing where the MR fluid is close to the iron brackets, providing a high permeability path for the field lines to follow, and preventing leakage through the air. Configuration C has a cutout in the brackets, away from the active fluid area, to increase the reluctance through the airgap, encouraging field lines to concentrate

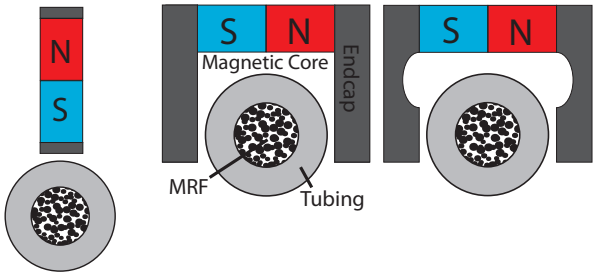

(a) Unguided (b) Rectangular (c) Curved

Figure 3.4: Three possible magnetic circuit designs, with magnetic cores in red and blue, the end caps in dark grey and the valves in light grey. Unguided magnets (a) have flat plate iron ends with the same cross-section as the magnets. Rectangular brackets (b) and curved brackets (c) have iron end caps which overhang the magnets. Rectangular end caps have constant reluctance across the airgap until the MRF is present. Curved end caps have a cutout at the base to increase reluctance in inactive area. Both curved and rectangular brackets provided enough field for a functional valve. With our concentration of iron particles, tubing thickness, and constriction size, rectangular brackets outperformed curved brackets.

inside the MRF in the valve. However, the curved brackets can result in some field leakage out of the active region, in the case of a very low reluctance in the tubing, due to saturation of the smaller cross sectional area of iron at the tips.

We used a wire electric discharge machining process to create the mild-steel brackets due to their small size and flatness requirements for the contact with the magnet ends. This is one of the most expensive components due to the manufacturing process at \$6.30 per pair, accounting for 86% of the cost of one complete valve. Given the similar results between the flat and curved brackets (Figures 3.10a and 3.10b), most applications will be satisfied with just the flat brackets which can be fabricated at a lower cost using a laser cutting process.

3.2.4 Control Circuit

The control board is dual layered and populated using SMT components for space savings. A strain-relief cable (Yellow Spectra thread) is bonded between the EPM assembly and control circuit to protect the fragile magnet wire during testing. Our prototype control circuit switches a single magnet per board and consists of an H-bridge, a large tank capacitor, two gate drive BJTs, an ATTiny13 microcontroller, a voltage regulator, and a tactile switch, which, including the board, cost $6.73 (Figure 3.5). The board is 22×22×6 mm. The largest individual component is the capacitor C1 (Board top right Figure 3.2), which stores the energy required to switch the EPM on the board, allowing for thinner gauge wires to supply power to the board and charge the capacitor with a low current. The next largest component is the tactile switch (Board bottom left Figure 3.2), which is only necessary on the prototype boards for manual actuation.

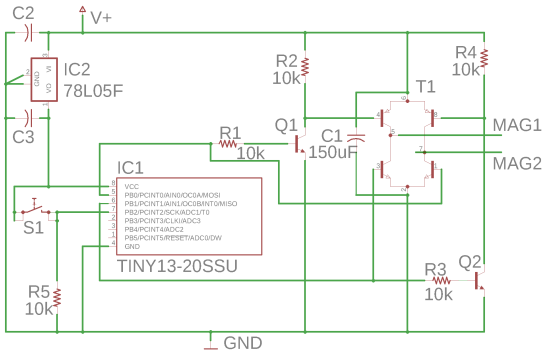

Figure 3.5: Circuit diagram for the prototype control board used during our valve experiments and implementation into a soft robot.

A benefit of the EPM valve design is that switching the state of the magnet is several orders of magnitude faster than the actuation rate of the robot, and so

a single capacitor and microcontroller can be used to switch multiple magnets. By replacing the H-bridge with a half bridge for each magnet and completing the circuit with a common half bridge we can reduce the board size, per magnet, considerably. The boards can also be remotely controlled through software, eliminating the tactile switch. The next generation boards (Figure 3.6), taking advantage of these optimizations, allow for controlling 5 EPMs with a board approximately half the size of the manually controlled prototype boards (Figure 3.2). Using one-wire serial communication over the power lines, we can control and power all of the boards using only two low current conductors, simplifying the design and assembly of the actuators.

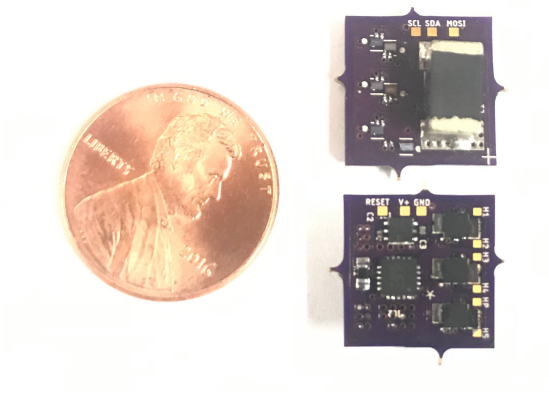

Figure 3.6: Miniaturized, second generation control board, which actuates up to five independent electropermanent magnets and is controlled via serial communication while taking up only $0.25\,\text{in}^2$.

3.2.5 Constrictions

For both non-jamming and jamming valves, the geometry of the passage can affect the performance of the valve. In the case of a yielding valve, a constriction in the valve prevents the fluid from sliding along the non-magnetic walls of the passage,

reducing the holding pressure, instead creating a plug of solidified material that must yield through the constriction in order to flow. The jamming probability/time to jam is a function of the ratio of constriction diameter to particle diameter. With no applied magnetic field, jams typically only spontaneously occur when constrictions are less than around 5× the diameter of the particles [106]. The magnetic field interaction with the MRF reduces the effective diameter of the constriction, while also increasing the cohesion of the grains, allowing jams to occur with larger constriction diameters [70]. An ideal valve will have the maximum constriction diameter that still allows for induced jamming, ensuring that the jam will clear when the magnet is turned off, and improving the OPEN flow rate. The constrictions were 3D printed (FormLabs) and are sized to have circular openings of 20, 30, and 40 times the maximum diameter of the largest 325 mesh iron particles (0.88, 1.32, 1.76 mm respectively) and a tapering constriction cross-section (Figure 3.7). We confirmed the aperture size using pin gauges as there is some inherent inaccuracy with printing, and only performed tests with valves that were within 0.05 mm of the nominal size.

3.3 Experimental Methods

MRF was supplied using a pneumatic syringe dispenser (Loctite) to pressurize a syringe full of MRF, measuring the pressure with a high resolution gauge (Winters) for all tests below 100 kPa and the built-in pressure gauge for higher pressures. We ran a tube from the syringe to the EP valve, and then another tube from the

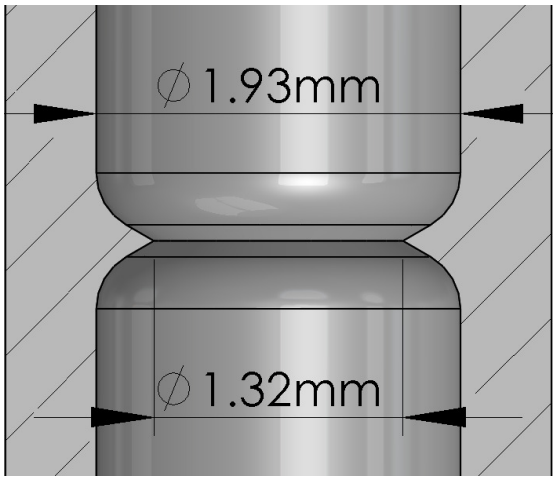

Figure 3.7: A cross-section of the 30× constriction throat showing the constriction geometry.

valve to a receptacle container. All tubes were rigidly fixed to a backing board to prevent shaking of the valve during operation. As the results are sensitive to small concentrations of additives, we cleaned any constrictions and tubing between different fluids with pure mineral oil. Tubing lengths were kept constant for all trials and between all tests so any variation in the head-loss due to tubing is minimized.

We conducted three primary experiments. The first test was a broad survey of different bracket, constriction, and fluid types. With a pressure regulator held at 105 kPa we set the valve to CLOSED, applied pressure and observed if the valve blocked flow. We then set the valve to OPEN and observed if flow resumed. We took three trials, and a single failure to jam or failure to resume flow resulted in a "fail". Results for this experiment are in Table 3.2. This test was used to find a working set of valves and fluids.

Using a subset of successful fluid and valve combinations from the first experiment, we performed a second experiment to assess the ability of the valves to

arrest flow in a valve which was already pressurized for several different supply line pressures. We set the pressure and began flow with the valve OPEN, then set the valve to CLOSED. We checked whether the valve jammed, and measured time until flow ceased, taking 3 trials for each fluid and pressure. Due to the viscosity of the material and manual measurement approach, values under one second were indistinguishable (Figure 3.8).

In the third test, we selected a pressure and set the valve to OPEN, then measured the mass flow rate of the fluid over a 30 second period. Using the density of each fluid, we calculated volume flow rate in milliliters per second. Results are time averaged based on the test approach, and we calculate error margin analytically based on error in timing and accuracy of the scale (Figure 3.9). OPEN state viscosity combined with CLOSED state holding pressure, and robot actuation volume, determine the actuation rate of a joint.

3.4 Results

3.4.1 Evaluating across multiple independent variables

There are a large number of potential independent variables in an MRF valve such as the mass percentage of iron (Fe) relative to mineral oil (MO), presence of oleic acid (OA), constriction size, end cap shape, and iron particle size. However, much of the data is best measured in a binary test; either the valve works (reliably jamming then returning to flow) or it does not. We created 6 fluids and tested each at 105 kPa as described in Section 3.3 with results in Table 3.2.

	Composition (Volume %)	20× (0.88 mm) constriction	30× (1.32 mm) constriction	40× (1.76 mm) constriction
Mix 1:	28.6 Fe, 70 MO, 1.3 OA	Fail-No Jam	Fail-No Jam	Fail-No Jam
Mix 2:	34.5 Fe, 64.2 MO, 1.3 OA	Success	Success	Fail-No Jam
Mix 3:	45 Fe, 53.7 MO, 1.3 OA	Success	Success	Fail-No Jam
Mix 4:	45 10 µm Fe, 53.7 MO, 1.3 OA	Fail-No Jam	Fail-No Jam	Fail-No Jam
Mix 5:	28.6 Fe, 71.4 MO	Fail-Irreversible	Fail-No Jam	Fail-No Jam
Mix 6:	34.5 Fe, 65.5 MO	Fail-Irreversible	Fail-Irreversible	Success

Table 3.2: Valve behavior for various MRF types. We first varied iron (Fe) and mineral oil (MO) concentration in Mix 1,2, and 3 while keeping the iron size (325 mesh) constant, and tested all three on each constriction size. We also test an MRF (Mix 4) that has the same mass percent of iron as Mix 3, but uses 10 micron sized iron particles to compare how iron size effects jamming. Mix 5 and 6 do not have oleic acid (OA). We set the valve to CLOSED, then applied 105 kPa of pressure, then set the valve to OPEN. If the valve did not jam it receives "Fail-No Jam" and if the jam did not reverse to allow flow then it receives "Fail-Irreversible". All trials taken using curved iron brackets, and Fe is 325 mesh unless specified.

Mix 5 and 6 highlight the importance of oleic acid; without it the mixtures were unsuitable for use. Mix 5 showed no successful tests and Mix 6 did not resume flow with the valve set to open at both 20× and 30× constriction sizes (which was not observed in any Mixes with oleic acid). Similarly, Mix 1 and Mix 5 showed that a mass percentage of iron below 30% is too low for jamming; at all constriction sizes these fluids failed.

In Mix 4, we used a single iron particle size (10 µm), while all other mixes were made with a polydisperse, 325 mesh, corresponding to particles up to 45 µm. The monodisperse, 10 µm fluid performed poorly and did not jam. The larger particles and polydisperse distribution of the particles promoted jamming by increasing the maximum packing density of the material, increasing the bulk magnetic permeability, and, when the path is a small multiple of the particle diameter, provide lower permeability paths, with fewer junctions, for the magnetic field to pass through. Polydisperse particles were able to form more stable configurations because they

have a higher number of average contact points for the larger grains [125]. Both Mix 2 and Mix 3 worked with the largest range of constrictions, with the only variation being the mass percentage of iron. These mixes were selected for further study to better characterize differences in the fluids (Figures 3.8 and 3.9).

3.4.2 Assessing performance and reliability

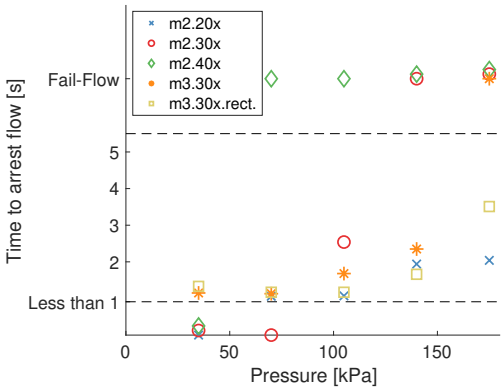

Figure 3.8: Time to arrest flow as a function of fluid pressure for several mixtures and orifice sizes (see Table 3.2 for details). As the pressure and orifice size goes up, the time to arrest flow also increases and the valve ultimately fails to jam. The legend states the mix, bracket type, and constriction (e.g. M2.20× is Mixture 2 with the 20× constriction). The brackets are curved unless specified as rectangular (rect.). Horizontal lines specify where the data is no longer continuous. Below the bottom line, all trials jammed within our margin of error. Above the top horizontal line, the valve did not arrest flow so the time to jam is not applicable.

We used a range of pressures to look at Mix 2 across all constrictions. We also tested Mix 3 across a range of pressures, with the 30× constriction, and both rectangular and curved brackets (Figure 3.8). The 40× constriction failed to jam in all but the highest concentration MRF (Mix 6) while both the 20× and 30× constrictions jammed reliably with Mix 2 and Mix 3, though the 20× constriction jammed more quickly than the 30×. The higher iron MRF (Mix 3) jammed more reliably.

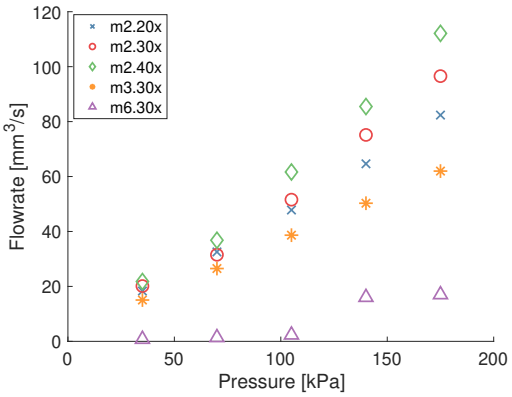

Figure 3.9: Flow rate as a function of pressure for several mixtures and constriction sizes. As iron concentration goes up, flow rate drops. The legend states the mix and constriction (e.g. M2.20× is Mixture 2 with the 20× constriction).

The valve with flat brackets outperformed the valve with curved brackets. This was unexpected, as we believed there would be more leakage of the magnetic field through the inactive area with the flat end caps, due to lower reluctance between the end caps, which would result in a lower field strength in the MRF cross-section. Because we use a thin walled constriction and 325 mesh iron particles which have a high permeability, the reluctance through the magnetic circuit that includes the MRF is much smaller than the reluctance through the air, even with the rectangular end caps, which makes any field leakage outside the MRF negligible. This is validated by our FEA analysis in Section 3.4.3.

In selecting a valve for a particular application, flow rate becomes an important consideration. We investigated five fluids for flow rate properties (Figure 3.9). As expected, Mix 6 without OA performed very poorly. Mix 2 outperformed Mix 3 as lower mass percentages of iron will lead to lower viscosity. As expected, a wider constriction leads to faster flow rate. Figures 3.8 and 3.9 can be used together to select a combination that jams at a desired pressure with the highest flow rate.

Once a valve was jammed, the pressure could be raised to the maximum tolerable by the supply tube (more than 405 kPa) without spontaneously unjamming, as long as the magnetic field was maintained, and still unjam after the magnetic field was removed.

3.4.3 EP Magnet Modelling

The end cap designs were analyzed, using FEA, in ANSYS Maxwell 3d (Figure 3.10). The end caps were made of soft iron, remnant fields in the alnico and neodymium magnets were fixed at 1350 mT, and the permeability of the magnetorheological fluid was considered to be linear and equal to 10. We found that the end cap design had a relatively small effect on the mean magnetic field, inside the valve active area, for the valve geometries investigated experimentally (Figures 3.10a and 3.10b). The rectangular end-caps had the largest resultant magnetic field, inside the active area, with a mean field of 229.4 mT, while the curved brackets had a mean field of 222.8 mT. This matched our experimental results where the rectangular bracket slightly outperformed the curved bracket. We also checked the off-state external magnetic fields to see if they were having an effect on the unjamming behavior of the valves (Figure 3.10c). We found that the magnetic field in the inactive area was a negligible 0.066 mT, which is on the order of the Earth's surface field. To test the effect of incomplete magnetization of the alnico magnet in the off-state, we reduced the alnico remnant field to 1250 mT. The resultant field, in the active area, was 4.3 mT, which is comparable to a flexible refrigerator magnet. This is ap-

proaching the level that could have some effect on the valve performance, however in experiment, we were able to remove the magnet completely from an irreversibly jammed valve without the flow resuming.

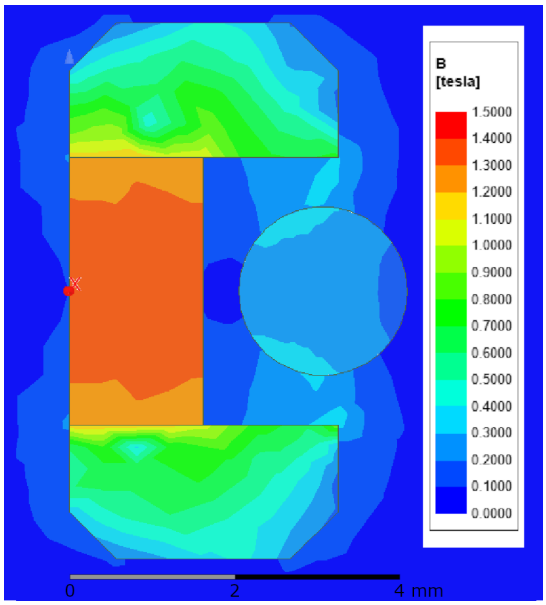

(a) Rectangular End-Cap

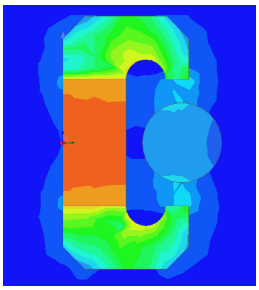

(b) Curved End-Cap

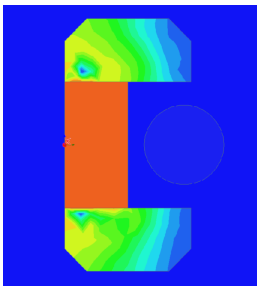

(c) Rect. End-Cap in Off State

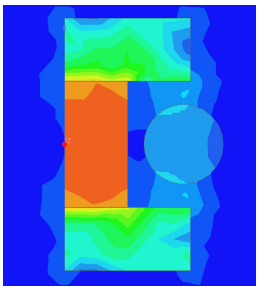

(d) Unchamfered End-Cap

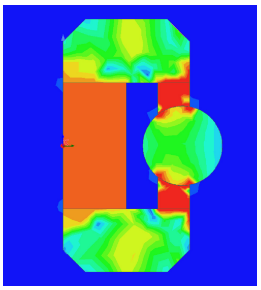

(e) Rect. End-Cap with Insert

Figure 3.10: FEA analysis of magnetic fields in the MR Valves for tested (*a*) rectangular and (*b*) curved end-cap designs, (*c*) the rectangular end cap in its off state, and two new possible designs, (*d*) unchamfered and (*e*) with inserts. Rectangular, curved and unchamfered end-caps produce similar magnetic fields, though the rectangular end cap does have a slightly stronger field than both unchamfered and curved designs and slightly outperformed curved in experiments. The insert design dramatically increases the field strength in the active area.

Using the FEA model, we are able to examine some new end-cap geometries. The end-cap shape seemed loosely coupled to field strength, so we checked the effect of removing the chamfered edges (Figure 3.10d). The resultant magnetic field was only slightly degraded, with a mean field of 224.5 mT, however this allows for simplified manufacturing, requiring only a waterjet or laser cutter to cut caps

from flat stock, rather than the specialized, wirefeed electric discharge machining manufacturing of the more complex end-caps. Looking at the field for these three end-cap designs, it can be seen that a considerable amount of field leakage is occurring around the active area. To mitigate the leakage we tested another design which has iron inserts in the valve body to bridge the gap between the end-caps and the MRF (Figure 3.10e). Adding inserts to reduce the reluctance in the magnetic circuit resulted in an increase in the average field of the active area by a factor of 2.5 to 557.8 mT.

3.4.4 Valve Simulation

Because of the many variables, expense of building new valves designs, and time consuming experimental testing process, we created a simulation framework for testing possible valve design revisions. We used a magnetic module we added into LIGGGHTS, an open source Soft Sphere DEM (SSDEM) software [51]. The magnetic module was developed for simulation of MRF in an MRF based soft gripper [104]. The simulation works by summing the forces on, and integrating the equations of motion for, each individual iron grain in the system. The particles interact with each other, through direct contact and magnetic interactions, with a fixed background magnetic field, fixed walls, and a constant background fluid flow field through stokes drag. The magnetic induction of the particles is done through the mutual dipole method, which iteratively calculates the dipole moment on a particle by summing the contribution from the background field, and all its close neighbors.

Then after all the dipoles are calculated, the process is repeated with the previous iteration's particle dipoles.

The simulations were initialized with a particle size distribution of 44% 44 µm, 35% 38.9 µm, 24.2% 33.8 µm, 13.2% 28.7 µm, 5.6% 23.6 µm by mass, and a total volume percentage of 34.5%, inside of 20×, 30× and 40× constrictions. Particles had a Young's modulus of 1 GPa, rather than the true value of 200 GPa, in order to maintain reasonable time step sizes (20 ns). It has been shown that the behavior of granular media, in simulations, is not strongly affected by reducing Young's modulus above 0.1% of the actual value [100]. The coefficient of friction was set to 0.4. The background fluid had a dynamic viscosity of 0.16 Pa s and a velocity profile of 0.273 m/s inside the constriction diameter, linearly decreasing to 0 m/s between the constriction diameter and the valve body's inside diameter. Coupled with the number of particles in the system and the flow velocity, the viscosity created a force on an arrested flow approximately equal to the force generated by 100 kPa of pressure acting on the system. In a volume immediately inside the constriction, the flow velocity is increased by a factor equal to the ratio of the valve and constriction diameters squared (Figure 3.11a). The particles were allowed to flow for 1 ms with no magnetic field. After the flow was established, a magnetic field, $\vec{B} = 230\,\mathrm{mT}\hat{x}$, was applied across the valve, and the system was allowed to run until it jammed, or until a steady flow rate developed.

The simulation recreated the experimental behavior of Mix 2, arresting flow in the case of the 20× and 30× constrictions, but failing to arrest flow in the case of the 40× constriction. Examining the connectedness of the particles (Figure 3.11b),

it can be seen that the particles in the arrested flows appear to be forming an arch across the gap, with a lens of particles (red), immediately between the constriction, disconnected from the bulk of the particles (blue). In the 40× constriction, in which the flow is never arrested, on the other hand, there are no discernible patterns to the connectedness, mostly consisting of relatively small, similarly sized clumps (Figure 3.11c).

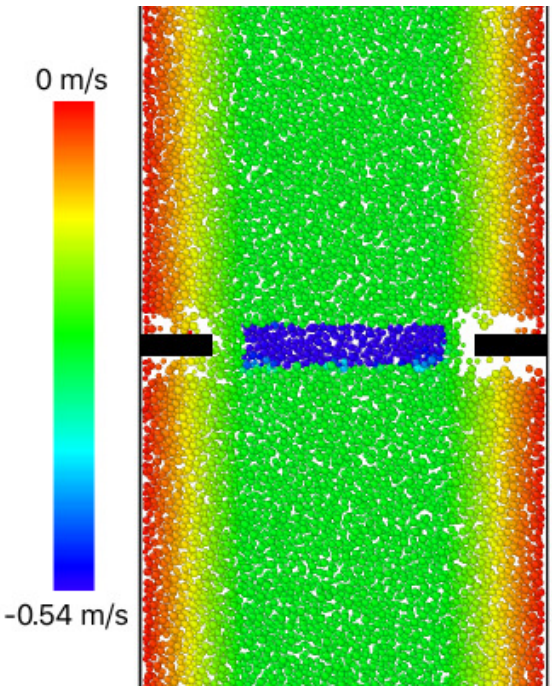

(a) Initialized valve

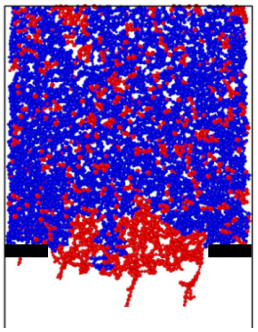

(b) Jammed 30× constr.

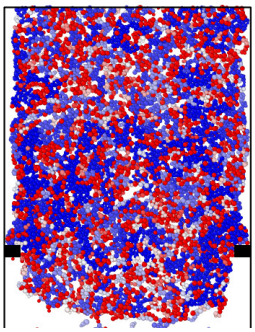

(c) Unjammed 40× constr.

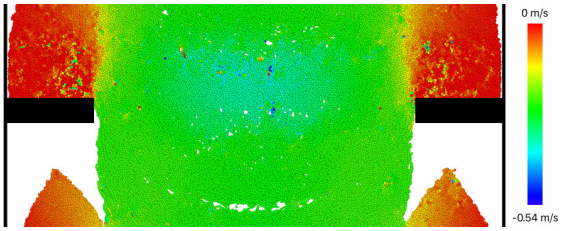

(d) Unjammed 10 µm particle valve

Figure 3.11: (*a*) The initialized, unmagnetized, 30× constriction with a 44 µm grain distribution, and background flow field, colored by particle speed. (*b*&*c*) The magnetized valves with a 44 µm grain distribution and a 230 mT magnetic field applied. The coloring shows connected groups. (*b*) The 30× constriction shows a large connected cluster (blue), and several disconnected clusters (red), including a disconnected lens between the constriction, demonstrating the jamming behavior (note: for clarity, the largest cluster is shown in blue, while all smaller clusters are shown in red). The flow is fully arrested. (*c*) The 40× constriction has a patchwork of bunched particles with no discernible pattern in the clusters. The flow is not arrested. (*d*) The unjammed, 30× valve, with a 10 µm particle distribution, colored by particle speed. The grain chains yield through the valve, bowing downwards. Flow is not arrested.

The simulation was repeated with a particle size distribution of 44% 10 µm, 35% 9.49 µm, 24.2% 8.98 µm, 13.2% 8.47 µm, 5.6% 7.96 µm by mass, a total volume percentage of 34.5%, and the same diameter constriction as in the 30× valve. The simulation was otherwise equivalent, though the valve was shortened in the direction of flow, due to the increased number of particles, to improve computation time and the time step was reduced to 5 ns due to smaller particle diameters. As with our experimental results, the 10 µm mixture failed to jam, and instead yielded through the constriction with no jamming behavior whatsoever (Figure 3.11d). This further strengthens the evidence that jamming behavior is observed in the 20× and 30× constriction, as the yield strength of an MRF is not strongly dependent on the grain size, however the larger grains do not yield through the constriction, despite having equal shear stress across the valve.

3.4.5 Demonstration in a soft robot

We constructed a two segment soft robot, where each segment is comprised of two antagonistic actuators (for a complete hydraulic circuit see fig. 3.12). The actuators had an internal volume of 10.8 cm^3, weighed 17.8 g when empty, and weighed 43.42 g when full of Mix 3 (Table 3.2) in the unactuated (straight) state. We printed our soft actuators using a SLA printer (Carbon3D, Sil-30) then assembled four actuators into a single continuum, bonding the actuators with an adhesive (SilPoxy). Each segment can bend 180 deg in either direction when actuated to 140 kPa using air. However, due to the density of the MRF, the robot was not able to reach this

full range of motion when actuated with MRF as it did not have enough torque to counteract the weight of the fluid.

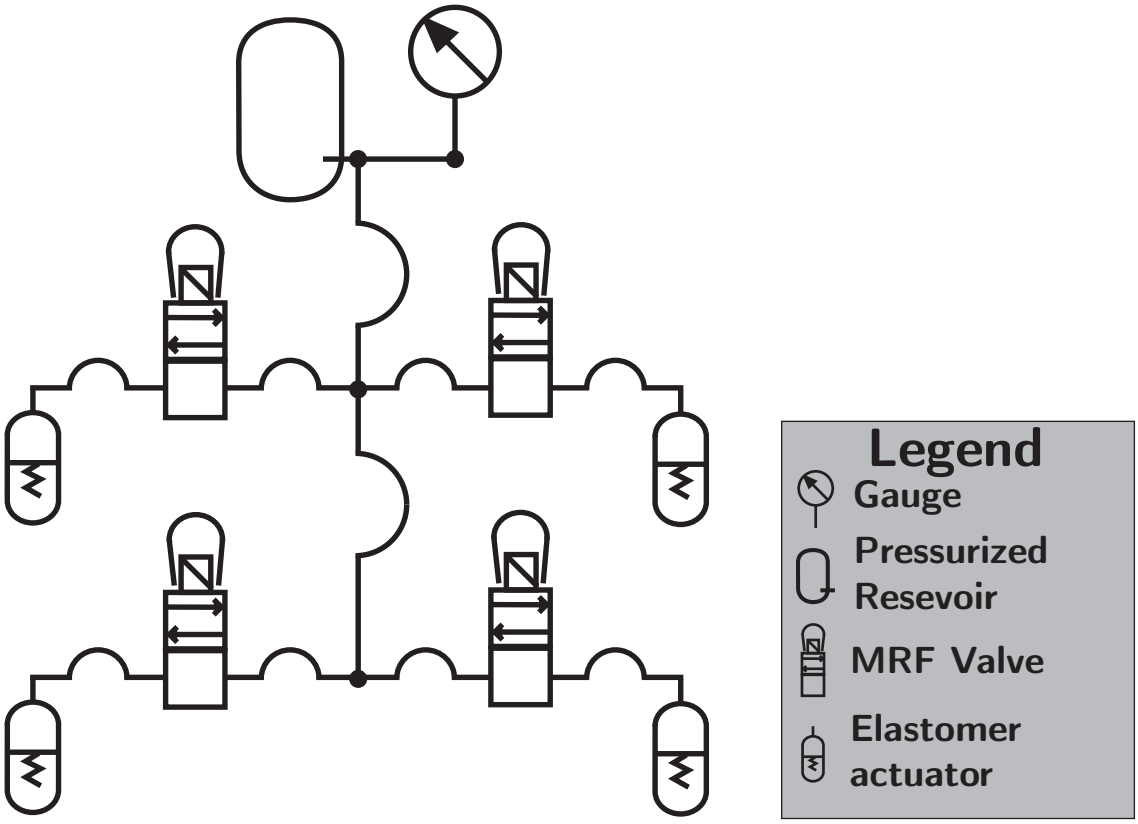

Figure 3.12: The hydraulic circuit for the soft robot demonstrated in section 3.4.5.

We individually controlled two of the actuators in the robot using MRF valves, showing unique shape generation (Figure 3.13). It took 250 seconds to fully pressurize an actuator. In our demonstration we only fill the actuators, however, due to the symmetry of the valve, suction can be applied to the reservoir and deflation controlled by the same fluid lines which control inflation.

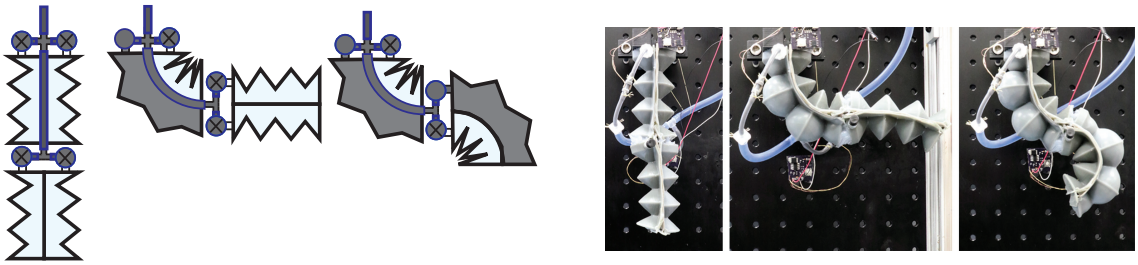

Figure 3.13: A demonstration using MRF to drive a 2 segment, 4 actuator soft robotic appendage. With a 140 kPa pressure source applied we control individual valves along the robot to change shape. It takes 250 seconds to pressurize these large actuators volume.

3.5 Discussion

Low flow rate through the constriction is one of the biggest challenges of an EPM based valve. Based on our FEA analysis of the electropermanent magnet design, we expect the performance of the valves can be considerably improved by adding paramagnetic inserts into the valve body in future work. The increased resultant field should allow a larger constriction diameter in the valve, increasing flow rate, while still reliably jamming. Furthermore, our model for the valve body in LIGGGHTS, while successful at recreating the valve performance in its current state, can be improved by adding fully resolved CFD-DEM coupling, which calculates both the fluid effects on the grains, as well as the grain effects on the fluid [126]. This would improve the fidelity of simulations and enable further computational design optimization. Coupled with additive manufacturing techniques for valve construction, an improved numerical framework should allow for quick and inexpensive development of electropermanent valve systems for new applications and design requirements.

Some potential issues with the valve need to be considered in future work and applications. First, the larger grains are more prone to settling. On the timescale of our experiments, this was not a problem, however fluid left undisturbed for two days required stirring to re-suspend particles. This is partially alleviated by surfactant (oleic acid), and can be further addressed with a more viscous carrier fluid, though this also affects flowrate. Second, MRF is a shear thinning fluid and the time to jam or un-jam for a valve is not constant across pressures. As the shear stress on the fluid increases, its viscosity is reduced and it flows faster (as observed with Mix 6, Figure 3.9). This non-constant behavior complicates control of the valve slightly. Finally, physically working with the fluid can be a challenge. Any leaks or failure can result in spillage that can contaminate surfaces, and damage sensitive electronics or sensors.

There are a few considerations for using MRF in soft robots, based on lessons learned from this investigation. 1) Actuators with smaller volume, and small changes in volume are well suited for MRF as not as much fluid is required to be transported. 2) Integrating the control circuit into the robot, and keeping tubing along a neutral bending axis will minimize the effects of tubing and wiring. This is facilitated by the actuator sitting outside the flow path, allowing flexibility in its implementation. 3) If the robot is designed with only short lengths of thin tubing branching from a single supply tube, running along the neutral axis, a larger supply tube can be used for a faster flow rate. As the equation for head loss along a cylindrical tube is proportional to the radius raised to the fourth power (r^4), a single wider tube will outperform many narrow tubes used in parallel. Soft actuators with low torque will

have a hard time reacting the mass of the MRF, and as such may be well suited for applications where the robot's effective weight is reduced, such as underwater or in microgravity. The large mass and thermal mass of the MRF could also potentially be used advantageously to dampen vibrations and sink heat away from other components. Future work optimizing and analyzing the kinematics of the MRF actuated soft robot is warranted to explore these topics.

3.6 Conclusions

We have presented a new valve construction that uses electropermanent magnets to induce reversible jams in magnetorheological fluid, as well as a numerical simulation framework for examining the valve behavior and designing new iterations of the valve. These valves are able to arrest flows at pressures up to 180 kPa and can hold over 415 kPa once jammed, while consuming zero steady state power and minimal switching energy. By reducing the size and energy requirements, these valves open a range of applications for magnetorheological fluids which were previously excluded by orders of magnitude of power and size limitations, particularly of interest are miniature robots where active damping and hydraulic actuation would have been previously impractical. We have also demonstrated that the valves are well suited for distribution along a soft robot. This valve addresses the fundamental challenges in controlling many lines of fluid pressure that have limited the number of degrees of freedom that can be independently controlled in fluidic soft robots. Using a small, low-mass, low-power, and economical valve, we demonstrated that a

single line of pressurized fluid with distributed and independently controlled valves can be used to drive a soft robot. With further integration efforts and improved actuator designs, this fluid control approach could lead to feasible soft robot designs with hundreds or thousands of independently controlled degrees of freedom.

Chapter 4: Magnetic Asteroids

This chapter contains material which is pre-submission to Icarus for publication.

4.1 Introduction

The properties of small planetary bodies in the solar system are of significant interest for understanding the formation and evolution of our solar system, and for the planning of exploration, planetary defense, and In-Situ Resource Utilization (ISRU) missions. Davis proposed that asteroids could be composed of loosely held together 'rubble piles' with little internal strength [82, 127]. Work by Richardson et al. provided support for the idea that asteroids could be composed of rubble piles [127]. Evidence from the breakup of comet P/2013 R3 indicated a rubble pile with some internal cohesive strength [128]. To learn crucial details about asteroid strength, structure, and composition, several missions have already been sent to small bodies in our solar system. Hayabusa visited the the asteroid Itokawa and found it to be composed of a mix of dust and boulders smaller than 10m in diameter [84]. Hayabusa 2 and OSIRIS-REx confirmed similar, though less dusty structures for asteroids Ryugu and Bennu [85, 86]. These missions have confirmed that some,

if not many, asteroids are rubble piles, agglomerates of many small pieces, loosely held together by gravity. Despite the evidence that asteroids largely consist of rubble piles, several asteroids have been observed to spin faster than would be stable through self-gravity of a non-cohesive rubble pile, implying some sort of internal strength [83, 128].

To explain the fast rotators Holsapple showed that a small cohesive force, friction, and rolling resistance, can account for the increased strength required to maintain a stable structure at high rates of spin, beyond the point of purely gravitational stability [87]. Scheeres et. al. found the asteroid and constituent scales at which the various forces – self-gravity, surface gravity, and cohesion – acting on an asteroid dominate, showing that for some cases cohesion can provide most of the strength of a cohesive rubble pile [89]. To better understand rubble pile structures, granular models have been simulated using Discrete Element Method (DEM) to examine formation and disruption of cohesive asteroids [31, 33].

Rubble pile asteroids can be disrupted through collisions which can both provide enough energy to directly break apart the asteroid, or through increasing the angular velocities beyond the structural limit of the agglomerate. Additionally, the YORP effect, a torque caused by differential heating and radiation from the surface of an irregular asteroid, may cause asteroids to increase their angular velocity until they are disrupted [83, 88, 129, 130]. The shape of the fragments created during disruption provide a test for simulations of asteroid strength, with different asteroid strength parameters resulting in different resultant shapes which can be compared to existing shape models [31, 33].

All asteroids visited by spacecraft to date have been S or C spectral type, corresponding with ordinary and carbonaceous chondrites. M-type asteroids, in contrast, have remained unvisited despite making up approximately 10% of the asteroid belt [131], and being of interest for ISRU. Due to their similar spectral profile to metallic meteorites, M-type asteroids are thought to be composed primarily of nickel and iron [93, 94]. M-type asteroids are speculated to be formed from the cores of protoplanets that had melted and differentiated dense metallic components and lighter silicates, and were then broken apart and stripped of their silicates through collisions in the early stages of planet formation [132]. This makes them attractive targets for planetary science as well, providing a window into cores of planets that are otherwise shrouded by rocky exteriors. Both nickel and iron are ferromagnetic materials, with large magnetic susceptibilities (χ) of greater than 100000 and 300 respectively. Nickel and Iron can have an induced magnetic dipole in the presence of a magnetic field and maintain a permanent, remnant magnetic dipole after an external field is removed. The Psyche mission, planned for a 2022 launch, will visit the M-type asteroid 16 Psyche, the third largest asteroid in the solar system. This mission will provide the first detailed observations of an M-type asteroid, giving further insight into their properties.

Magnetic fields have been detected around several rocky asteroids during close approaches despite the low concentrations of magnetizeable material compared to metallic asteroids. The Galileo spacecraft indirectly measured a possible magnetic field around the asteroid Gaspra during a close approach [28]. The magnetic field perturbation was attributed to the disruption of the solar wind by the asteroid's

magnetosphere. Also, a direct measurement was made by the Deep Space 1 (DS1) spacecraft during its flyby of the asteroid Braille [29]. The magnetization of these two asteroids was found to be 93 A/m and 110 A/m respectively [29]. These magnetizations also agree with those of magnetized chondrites discovered on earth [27]. The bulk dipole moment provides a lower bound on the magnetization of individual grains. Any grains in the asteroid that are aligned opposite the bulk magnetization would decrease the effective magnetization of the whole asteroid, requiring a higher mean magnetization of the individual grains to create the same bulk magnetization. Due to their higher proportion of magnetic material, and observed magnetization in metallic meteorites, magnetic forces may influence the coalescence and morphology of M-type asteroids. Similarly, the additional magnetic forces may influence disruption of asteroids spun up by the YORP effect.

The recent visit to our solar system by the interstellar object 1I/2017 U1, 'Oumuamua, raised several questions. It was found to have a very high aspect ratio of 3.5-10:1, the formation of which is difficult to understand based on forces conventionally considered for small bodies [97]. Zhang has shown it is possible to create high aspect ratio objects during tidal disruption however [133]. Additionally, 'Oumuamua had a large extra-gravitational acceleration as it approached perihelion. This acceleration was stronger than would be expected for an asteroid or comet with normal densities $\sim 2\,\mathrm{g/cm^3}$ and the observational limits set on outgassing [98]. Gravity acts in a radially symmetric way that leads to spheroidal minimum energy configurations. Similarly, cohesion acts symmetrically in all directions, leading to a minimum energy in a closely packed spheroidal configuration. Magnetism, in

contrast, acts heterogeneously. The force on a dipole $\vec{m}$ by an external magnetic field $\vec{B}$ is given by eq. (4.1) and the field created by a dipole is given by eq. (4.2). The maximum attractive force for magnetic dipoles is when they are aligned axially in a chain, creating a large tensile strength. However, the same particles, when placed next to each other, perpendicular to their dipole moments, will repel each other. This asymmetric force may allow for low energy configurations which are loosely packed and non spheroidal. Given 'Oumuamua's spectral signature, which is consistent with M-type asteroids, magnetism may explain the low density and aspect ratio.

$$\vec{F}_m = \nabla(\vec{m} \cdot \vec{B}) \tag{4.1}$$

$$\vec{B}(r) = \frac{\mu_0}{4\pi}\left[\frac{3\vec{r}(\vec{m} \cdot \vec{r})}{r^5} - \frac{\vec{m}}{r^3}\right] \tag{4.2}$$

With magnetic fields strengths on the order of the fields around Braille and Gaspra, magnetic effects may have an impact on the formation and shape of metallic asteroids. We will investigate the effects of these magnetizations on the formation of metallic asteroids using open source Soft Sphere Discrete Element Method software modified to include magnetic forces and self gravity. Additionally, we will investigate the evolution of magnetized asteroids through YORP effect spinup and surface mass wasting.

4.2 Coalescence

To examine the effect on asteroid formation of remnant magnetism, we simulated the formation of an iron rubble pile asteroid from a thermal cloud of iron particles with remnant magnetizations.

4.2.1 Simulation

4.2.1.1 Contact Force Model

Our simulations were run on the open source DEM code LAMMPS [50]. LAMMPS uses a Soft Sphere DEM (SSDEM) model where particles are treated as soft spheres that can interpenetrate each other with a restoring force modeled as a spring-dashpot force. The particle-particle contact forces govern how particles resist interpenetrating and rebound off each other in collisions. We use Hertzian model contact forces, which treats the particles as an elastic material with a defined Young's modulus and Poisson ratio. Given two spherical particles with radii R_i, R_j, masses m_i, m_j, Young's modulus Y_i, Y_j, Poisson ratio ν_i, ν_j, and coefficient of restitution e, co-penetrating each other a distance Δn_{ij}, with a normal component of their relative velocities $v_\perp$, the normal force between particles is given by (eq. (4.3)). The tangential force is similarly formulated with an additional sliding friction coefficient μ_x which limits the maximum Hertzian tangential force $F_t \leq F_n \mu_x$ [50, 134].

$$F_n = k_n \Delta n_{ij} - \gamma_n v_\perp \tag{4.3}$$

$$k_n = \frac{4}{3}E^*\sqrt{R^*\Delta n_{ij}}; \quad \gamma_n = \sqrt{\frac{4}{3}}\beta\sqrt{S_n m^*}$$

$$\frac{1}{E^*} = \frac{1-\nu_i^2}{Y_i} + \frac{1-\nu_j^2}{Y_j} \quad S_n = 2E^*\sqrt{R^*\Delta n_{ij}}$$

$$\beta = 1.2728 - 4.2783e + 11.087e^2 - 22.348e^3 + 27.467e^4 - 18.022e^5 + 4.8218e^6$$

Where m^* and R^* are the reduced mass and radius found by section 4.2.1.1.

$$\frac{1}{K^*} = \frac{1}{K_i} + \frac{1}{K_j}$$

Rolling resistance is included to mimic some of the mechanical effects of some of the asphericity and angular shape of grains in space environments. We use the SDS model from Ludwig with friction constant and damping coefiicient k_{roll} and γ_{roll}, angular displacement and velocity ξ_{roll} and v_{roll}, and coefficient of rolling resistance μ_{roll} [135] (eq. (4.4)).

$$\vec{\tau}_{roll} = R^*\vec{n}_{ij} \times \left[min\left(\|k_{roll}\vec{\xi}_{roll} - \gamma_{roll}\vec{v}_{roll}\|, \mu_{roll}F_n\right)\vec{v}_{roll}/\|\vec{v}_{roll}\|\right] \tag{4.4}$$

The Derjaguin-Muller-Toporov (DMT) cohesion model is implemented with an attractive cohesion force between particles given by eq. (4.5),where γ_c is the surface energy density of the particle pair.

$$F_{ncohesion} = -4\pi\gamma_c R^* \tag{4.5}$$

4.2.1.2 Magnetic Model

We implement a magnetic force model, based on the model previously implemented in LIGGGHTS for magnetorheological fluids, but including permanent magnetizations [99, 101]. The force and torque on a magnetic dipole ($\vec{m}$) by an external magnetic field ($\vec{B}$) is given by [16]:

$$\vec{F}_m = \nabla(\vec{m} \cdot \vec{B}) \tag{4.6}$$

$$\vec{\tau}_m = \vec{m} \times \vec{B} \tag{4.7}$$

The total force on a magnetic grain with dipole moment ($\vec{m}_i$) due to the dipole field of its neighbors ($\vec{B}_j(\vec{r}_{ij})$) separated by ($\vec{r}_{ij} = \vec{r}_j - \vec{r}_i$) is therefore equal to (eq. (4.1)):

$$\vec{F}_i = \nabla(\vec{m}_i \cdot \vec{B}_0) + \sum_{j=1, j\neq i}^{n} \nabla \left[\vec{m}_i \cdot \vec{B}_j(\vec{r}_{ij}) \right] \tag{4.8}$$

$$\vec{F}_i = \nabla(\vec{m}_i \cdot \vec{B}_0) + \frac{3\mu_0}{4\pi} \sum_{j=1, j\neq i}^{n} \vec{1} r_{ij}^4 [\vec{m}_j(\vec{m}_i \cdot \hat{r}_{ij}) +$$

$$\vec{m}_i(\vec{m}_j \cdot \hat{r}_{ij}) + \hat{r}_{ij}(\vec{m}_i \cdot \vec{m}_j) - 5\hat{r}_{ij}(\vec{m}_i \cdot \hat{r}_{ij})(\vec{m}_j \cdot \hat{r}_{ij})]$$

The total torque is equal to:

$$\vec{\tau}_i = \vec{m}_i \times \vec{B}_0 + \sum_{j=1, j\neq i}^{n} \left[\vec{m}_i \times \vec{B}_j(\vec{r}_{ij}) \right] \tag{4.9}$$

$$\vec{\tau}_i = \vec{m}_i \times \vec{B}_0 + \frac{\mu_0}{4\pi} \sum_{j=1, j\neq i}^{n} \frac{1}{r_{ij}^3} \left[3\vec{m}_i \times \hat{r}_{ij}(\vec{m}_j \cdot \hat{r}_{ij}) - \vec{m}_i \times \vec{m}_j \right]$$

The magnetic field and torque drops off at r^{-3}, while force drops off as r^{-4}, so the fields and forces can be approximated by summing over a short range, with acceptable accuracy. Using a cutoff distance of several particle diameters allows for high fidelity, while still maintaining efficient parallelization of the workload across processors[99]. For our simulations a magnetic force cutoff distance of three of the subject particle diameters is used.

4.2.1.3 N-Body Gravity

Gravitational forces drop off proportional to r^{-2}; therefore, a range cutoff can add unacceptable error. The field from one particle does not, however, depend on the field from any other particles, simplifying the physics to solving Poisson's equation for N-bodies. Using a purely spectral solver limits the near field accuracy while using an exact solution is slow. Instead, we use a Particle-Particle Particle-Mesh (PPPM) solver. In PPPM solvers, the problem is decomposed into long range and short range terms [136]. The short range term is calculated exactly for near neighbors. The long range term is then calculated spectrally, using Fast Fourier Transforms (FFTs). LAMMPS implements the PPPM solver for the purposes of

simulating electrostatics. In order to adapt it for the purposes of gravitational forces, a dielectric constant of -1 was used for the empty space. Particles were then given a charge proportional to the mass (eq. (4.10))[137].

$$q_i = m_i\sqrt{G} = m_i\sqrt{7.425826298 \times 10^{-21}} \tag{4.10}$$

4.2.1.4 Initialization

The particles are initialized to a spherical cloud of 32,662 particles on a simple cube lattice with a lattice length of 2 m. They have diameters of 50 cm and 100 cm and a density of 3 g/cm^3. The low density, compared to pure iron, assumes a high porosity in the individual boulders. Additional particle properties can be found in table 4.1. The cloud is given random velocities following a Boltzmann velocity distribution with a temperature of 8e20 times the cube of the particle diameter and a random angular velocity with a normal distribution. In addition to the random velocities, simulations were run with several angular velocities about the system center of mass of 500 µrad/s, 1000 µrad/s, and 2000 µrad/s added to the Boltzmann distribution such that $\vec{v}_i = \vec{v}_{i_{boltz}}(T) + \vec{\omega} \times \vec{r}_i$. A large, permanently magnetized "seed" particle, with diameter 5 m, is placed in the center of the cloud to provide a core for the particles to coalesce onto. All the particles are then given a permanent magnetization of 0, 119, or 1190 A/m. The system is then integrated to show the time evolution as the particles coalesce.

Particle Diameters	50 cm		100 cm
Magnetizations	0 A/m	119 A/m	1190 A/m
Angular Velocity	$\mu = 5 \times 10^{-5}$ rad/s, $\sigma = 10^{-4}$ rad/s		
Density	$3000\,\mathrm{kg/m^3}$		
Young's modulus	$10^6\,\mathrm{N/m^2}$		
Coefficient of Restitution	0.1		
Poisson's ratio	0.3		
Surface Energy Density	$2.86 \times 10^{-3}\,\mathrm{J/m^2}$		
Sliding Friction	$\mu_s = 0.4$		
Rolling Friction	$\mu_r = 0.8$, $\gamma_r = 0.4$, $k_r = 10$		

Table 4.1: Simulation particle properties for asteroid self gravity simulations

4.2.2 Results

4.2.2.1 Agglomeration Rate

The agglomeration rate increases as the magnetization of the grains increases (fig. 4.1). The grains in the magnetized systems begin to form chains and clumps as they orbit the Center of Mass (CoM). These chains have a larger cross section of interaction, resulting in more collisions and a faster dissipation of the energy in the system. In the highly magnetized 50 cm system, large clumps form very quickly and those clumps then coalesce into the final asteroid shape. By 15 000 s, 89% of the uncoalesced particles are in chains or clumps of two or more particles and 45% are in clumps of more than 10 particles. The low magnetization 50 cm system particles form chains more slowly and do not tend to clump as much. By 15 000 s, 14.5% of the uncoalesced particles are in chains of two or more particles, and only 1% are in clumps of 10 or more particles. The unmagnetized 50 cm grains do not form clumps and form very few chains. At 15 000 s, only 0.7% of the uncoalesced particles are in

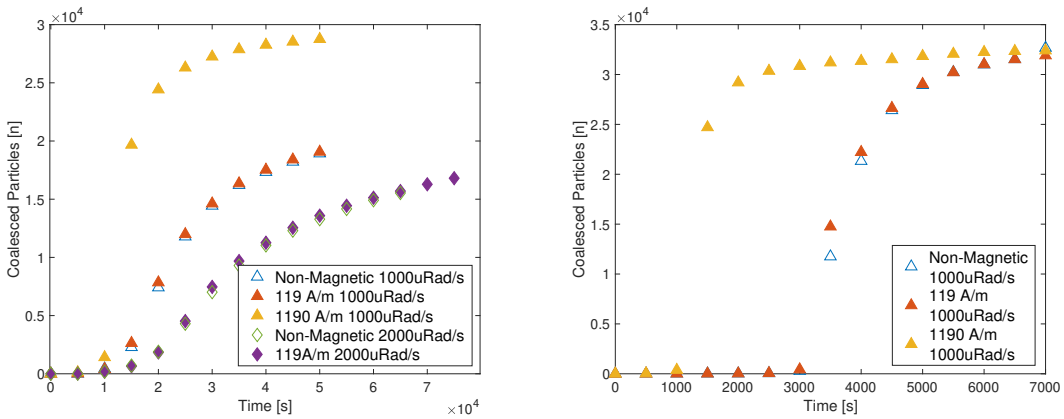

(a) Agglomeration rates of 50 cm grains (b) Agglomeration rates of 100 cm grains

Figure 4.1: The 1190 A/m grains coalesce much faster than the other two systems. The unmagnetized grains coalesce at the lowest rate, slightly slower than the 119 A/m grains for both the 50 cm and 100 cm grains. The 100 cm grains coalesce much faster than the 50 cm grains due to their larger cross section and the larger mass of the system.

chains of which only three chains are longer than two particles and zero chains are longer than three particles (fig. 4.2).

4.2.2.2 Structure

The asteroids coalesced from the dust clouds form shapes that are roughly oblate spheroids, as expected (figs. 4.3 and 4.4). The unmagnetized and lightly magnetized asteroids form very similar shapes. The structure of the highly magnetized asteroids, particularly of the smaller 50 cm grains, is extremely convoluted and irregular in comparison, with many caverns, voids, and arches (figs. 4.3e and 4.4c). This is expected given the repulsive forces between chains of magnetized particles, as well as the increased 'stickiness' of the particles, which prevents them from falling deeper into the asteroid after they are captured by an exterior particle chain. As the spin rate increases, the asteroids become more oblate in shape. The 119 A/m,

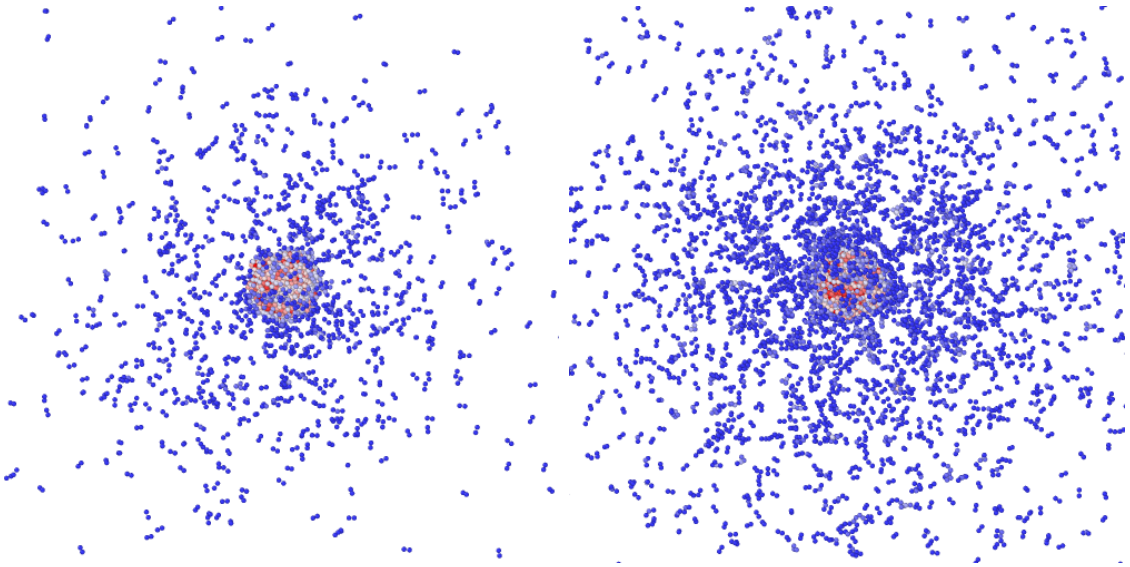

(a) Unmagnetized asteroid coalescing

(b) 119 A/m asteroid coalescing

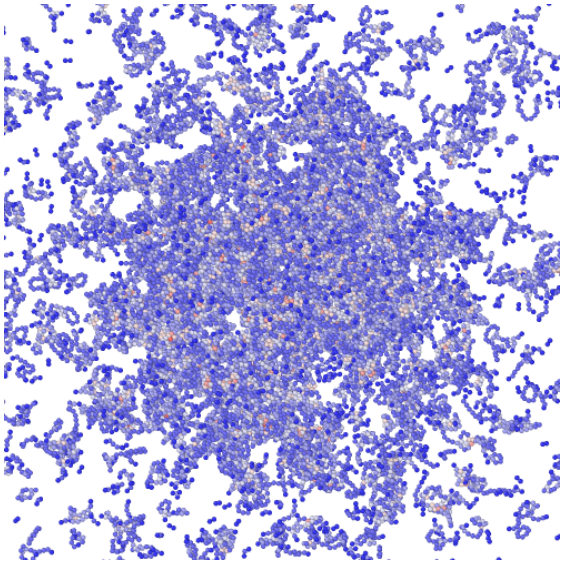

(c) 1190 A/m asteroid coalescing

Figure 4.2: Unmagnetized, lightly and heavily magnetized, 50 cm grain asteroids after coalescing for 15 000 s. Uncoalesced particles that are not in particle chains or clumps have been deleted, showing only chained particles. The unmagnetized particles form very few chains and therefore coalesce more slowly. The 119 A/m grains form small chains while the 1190 A/m grains form large chains and clumps, coalescing rapidly.

2000 µrad/s asteroid developed an elongated bulge near its equator that was not present in the unmagnetized asteroid (fig. 4.3g). The simulations with 2000 µrad/s initial angular velocities resulted in asteroids with minor axis near the minimum, constrained by the 5 m seed particles.

Fitting minimum bounding triaxial ellipsoids to the resultant asteroid shapes allows us to quantify some of the differences in shape (table 4.2). The magnetized asteroids appear more spherical and have smaller ratios between their major and minor axis, with the exception of the 2000 µrad/s, 50 cm asteroid, which developed a considerable protrusion in the magnetized case (white colored particles in fig. 4.3g). While the lightly magnetized asteroids have a smaller ratio between their axes than the unmagnetized asteroids, the highly magnetized asteroids have higher ratios than the low-magnetized asteroids. This may be due to the increased tensile strength of the magnetized grains holding the structure together, preventing equatorial bulge, while the irregular surface of the highly magnetized asteroids tends to push the boundaries of the minimum bounding ellipsoid outward.

As the magnetization increases, the size of the asteroid also increases. The 1000 µrad/s, 50 cm, 1190 A/m asteroid has 6 times the volume as its unmagnetized counterpart (table 4.2). This is partially explained by the increased number of particles captured by the magnetized asteroids vs. the unmagnetized asteroids. However, reduced density and increased porosity also contributes (figs. 4.5 and 4.6).

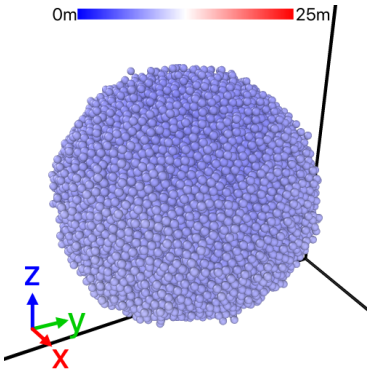

(a) Unmagnetized, with 500 µrad/s angular velocity

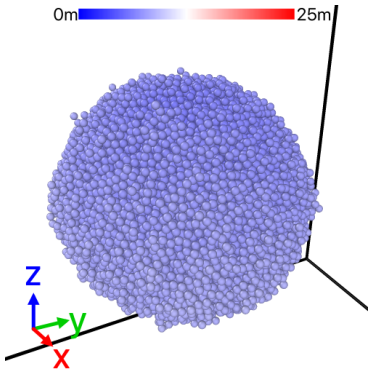

(b) 119 A/m magnetization and 500 µrad/s angular velocity

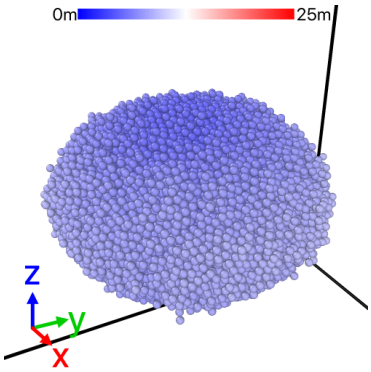

(c) Unmagnetized, with 1000 µrad/s angular velocity

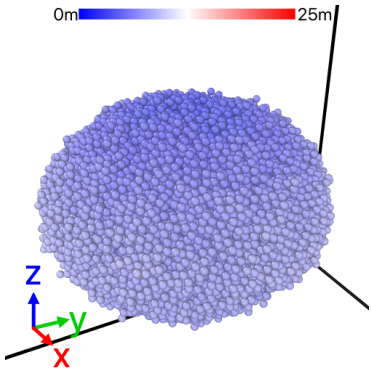

(d) 119 A/m magnetization and 1000 µrad/s angular velocity

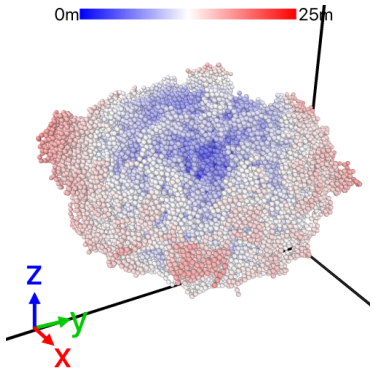

(e) 1190 A/m magnetization and 1000 µrad/s angular velocity

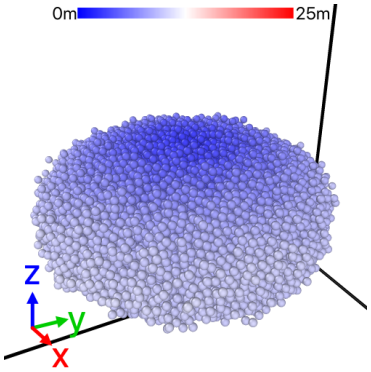

(f) Unmagnetized, with 2000 µrad/s angular velocity

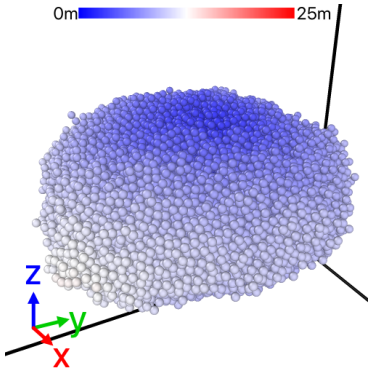

(g) 119 A/m magnetization and 2000 µrad/s angular velocity

Figure 4.3: Final asteroid shapes for several magnetic field strengths, and initial angular velocities for 50 cm grains. Particles are colored by their distance from the CoM of the asteroid

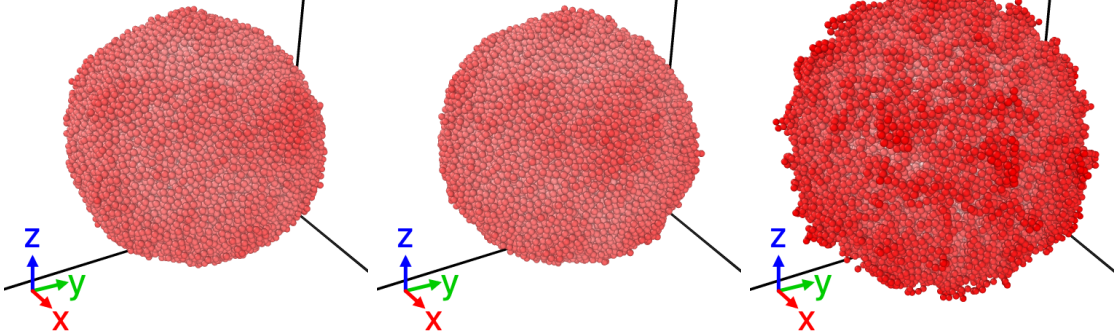

(a) Unmagnetized, with 1000 µrad/s angular velocity

(b) 119 A/m magnetization and 1000 µrad/s angular velocity

(c) 1190 A/m magnetization and 1000 µrad/s angular velocity

Figure 4.4: Final shapes for 100 cm grain asteroids with several magnetic field strengths, and an initial angular velocity of 1000 µrad/s. Particles are colored by their distance from the CoM of the asteroid

Particle Size	Angular Velocity	Magnetization	Major Axis	Inter. Axis	Minor Axis	Maj./Min. Ratio
50 cm	500 µrad/s	Unmagnetized	9.1738 m	8.8680 m	8.2030 m	1.1183
		119 A/m	9.3322 m	9.0238 m	8.4696 m	1.1018
	1000 µrad/s	Unmagnetized	9.6852 m	9.4346 m	6.8965 m	1.4044
		119 A/m	9.7087 m	9.4537 m	7.4939 m	1.2955
		1190 A/m	17.7205 m	16.8534 m	12.7270 m	1.3924
	2000 µrad/s	Unmagnetized	10.3581 m	9.8403 m	5.0588 m	2.0475
		119 A/m	11.3061 m	10.2350 m	5.1584 m	2.1918
100 cm	1000 µrad/s	Unmagnetized	21.3510 m	20.5915 m	19.6541 m	1.0863
		119 A/m	21.3678 m	20.7571 m	20.0575 m	1.0653
		1190 A/m	25.9366 m	25.1804 m	24.1899 m	1.0722

Table 4.2: Asteroid bounding ellipsoids

4.2.2.3 Density

We calculated the density for the final asteroid shapes by dividing their mass by the volume of a minimal convex hull created by its bounding particles. The density of the final coalesced asteroids tends to decrease with increasing magnetization (fig. 4.5). The Voronoi volume is the total volume of space closer to the center of a grain than any other grains. It is found from the volume of the polyhedra formed by vertices on the bisection of the line connecting the particle with its nearest neighbors. Using the minimum bounding triaxial ellipsoid as the outermost shell,

we created concentric ellipsoidal shells of equal volume and aspect ratios starting from the center of the asteroids and progressing outward to the minimal bounding ellipsoid. We found that the Voronoi volume of the inner shells was similar for the low magnetization asteroids and the unmagnetized asteroids. Grains closer to the surface of the low magnetization asteroids, however, diverged considerably from the Voronoi volume of the unmagnetized asteroid. The highly magnetized asteroids had significantly larger Voronoi volumes throughout the asteroid, though still increasing considerably near the surface (fig. 4.6). The seed particle creates a larger average Voronoi volume in the center most shell, particularly for the closely packed unmagnetized and low magnetization grains.

4.2.2.4 Bulk Magnetization

The magnetization of the individual grains used in our low magnetization simulations are comparable to bulk magnetizations previously measured around asteroids Braille and Gaspra, as well as those measured in meteorites. The highly magnetized grains are an order of magnitude stronger than bulk magnetizations detected. The bulk dipole moment is the sum of the individual dipoles however, and because they are not fully aligned, the bulk magnetization will be less than or equal to the individual magnetizations. In addition to the dipole moment, the unaligned dipoles will create higher order terms in the multipole expansion. The higher order terms will drop off much faster than the dipole terms, and so for the measurements made by DS1 and Galileo spacecrafts, the dipole term will dominate, dropping off at

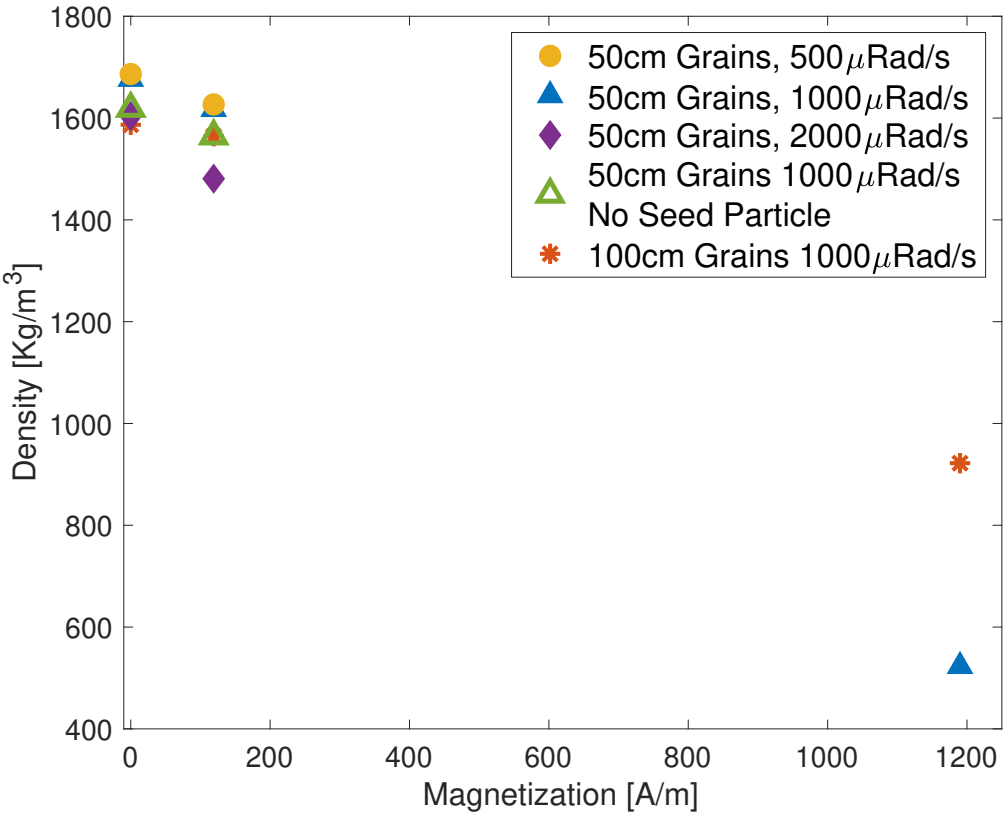

Figure 4.5: Density of asteroids formed by various initial dust clouds as a function of grain magnetization

$\propto r^{-3}$ while the quadrapole term will drop off $\propto r^{-5}$. Summing the dipole moments gives a bulk dipole of $7.3 \times 10^3\,\mathrm{Am}^2$, 4% of the maximum dipole moment for the low magnetization, 50 cm grains and $7.1 \times 10^4\,\mathrm{Am}^2$, 3.2% of the maximum dipole moment for the highly magnetized grains. The bulk magnetization, found from dividing the dipole moment by the convex hull volume, is 6.4 A/m for the highly magnetized asteroid and 3.0 A/m for the low magnetized asteroid. Using a hull that minimally contains all bounding particles, but does not require convexity, gives a bulk magnetization of 8.7 A/m for the highly magnetized asteroid and 3.2 A/m. Increasing the grain magnetization by an order of magnitude resulted in an order of

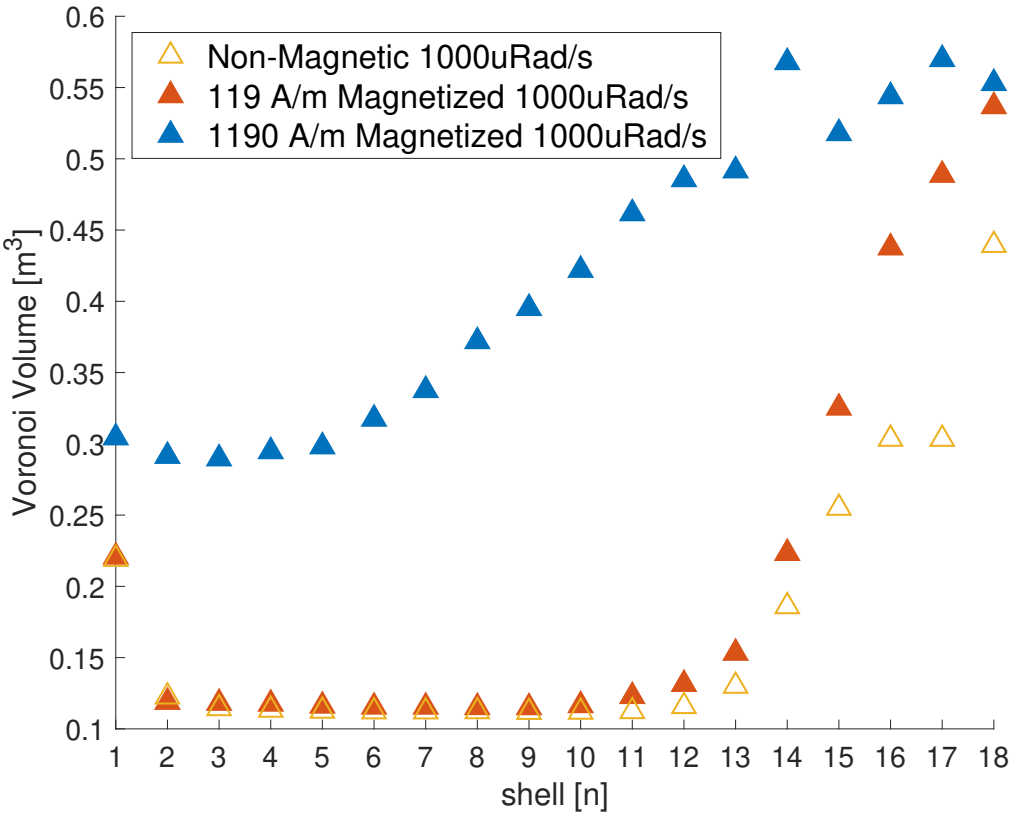

. The porosities of the unmagnetized and 119 A/m magnetized asteroids are similar towards the core, but the magnetized asteroid porosity increases more rapidly towards the surface. The highly magnetized asteroid is considerably more porous throughout, though the density does not decrease as rapidly and begins to converge with the less magnetized asteroid near the surface.

Figure 4.6: Mean Voronoi volume of grains in concentric ellipsoidal shells of equal volume for 50 cm grains with an initial angular velocity of 1000 µrad/s

magnitude higher bulk dipole, but only increased the resulting bulk magnetization by a factor $2-3\times$ due to the decreased packing fraction of the highly magnetized grains.

4.3 Spin-Up

Asteroids can be subjected to a torque due to differential heating and radiation, which can cause them to spin-up and be disrupted through the YORP effect [88, 129, 130]. As the asteroid spins up, it can reach a speed where it becomes destabilized and gets disrupted. The increased tensile strength due to magnetism will affect the asteroid's ability to resist this disruption as well as how it breaks up after disruption. To examine this we simulated these disruption events in LAMMPS using the same models and parameters as in the coalescence simulations (table 4.1).

4.3.1 Simulation

To start with as close to the same initial configuration as possible, we initialized disruption simulations similarly to the coalescence simulations, but without an initial tangential velocity, so the grains would quickly coalesce. The grains were allowed to coalesce under self-gravity until they formed roughly spherical agglomerates. We again used 50 cm and 100 cm grain sizes and 0 A/m, 119 A/m, and 1190 A/m grain magnetizations. For the 50 cm simulations, 33220 particles were used and for the 100 cm simulations, 4088 particles were used to get equal mass objects. For the spin up simulations, we omitted the central core particle.

After coalescing, the asteroid angular velocities were stepped up in increments of 100 µrad/s at intervals of 500 seconds until they reached 400 µrad/s and then at intervals of 3000 seconds until the asteroid had a deformation event where the grains shifted but no mass was lost. The deformation event was integrated until it reached

steady state. The spin up process was then resumed at 3000 second intervals until the asteroid began to disrupt. The asteroid was considered disrupted when it shed grains from the surface. The disruption event was integrated until the dynamics of the disruption were fully resolved.

4.3.2 Analysis

As the asteroids spin up, an initial deformation event occurs (figs. 4.7b and 4.8b). For the unmagnetized and low magnetization asteroids, with both large and small grains, the first significant deformation occurred at an angular velocity of 600 µrad/s and resulted in the spherical initial state getting deformed into an oblate spheroid. The unmagnetized grains developed a slightly larger equatorial bulge, 1.28× wider than tall vs 1.27× for the 50 cm grains and 1.39× vs 1.28× for the 100 cm grains. The highly magnetized grains had their primary deformation event at 700 µrad/s. The small grains formed the beginnings of a binary fissure with chains of particles tying the two halves together across the fissure line (fig. 4.9). The large grains formed a very porous structure in the center surrounded by a higher density ring around it. The highly magnetized asteroids had most of their elongation along a single axis rather than forming an oblate spheroid shape with an equatorial bulge. The small grains had an intermediate axis only 1.17× the size of the minor axis, but had a major axis 1.46× the minor axis, while the large grained asteroid had an intermediate axis 1.21× the minor axis and a major axis 1.85× the minor axis.

After the deformation event the asteroids were spun up again until they lost

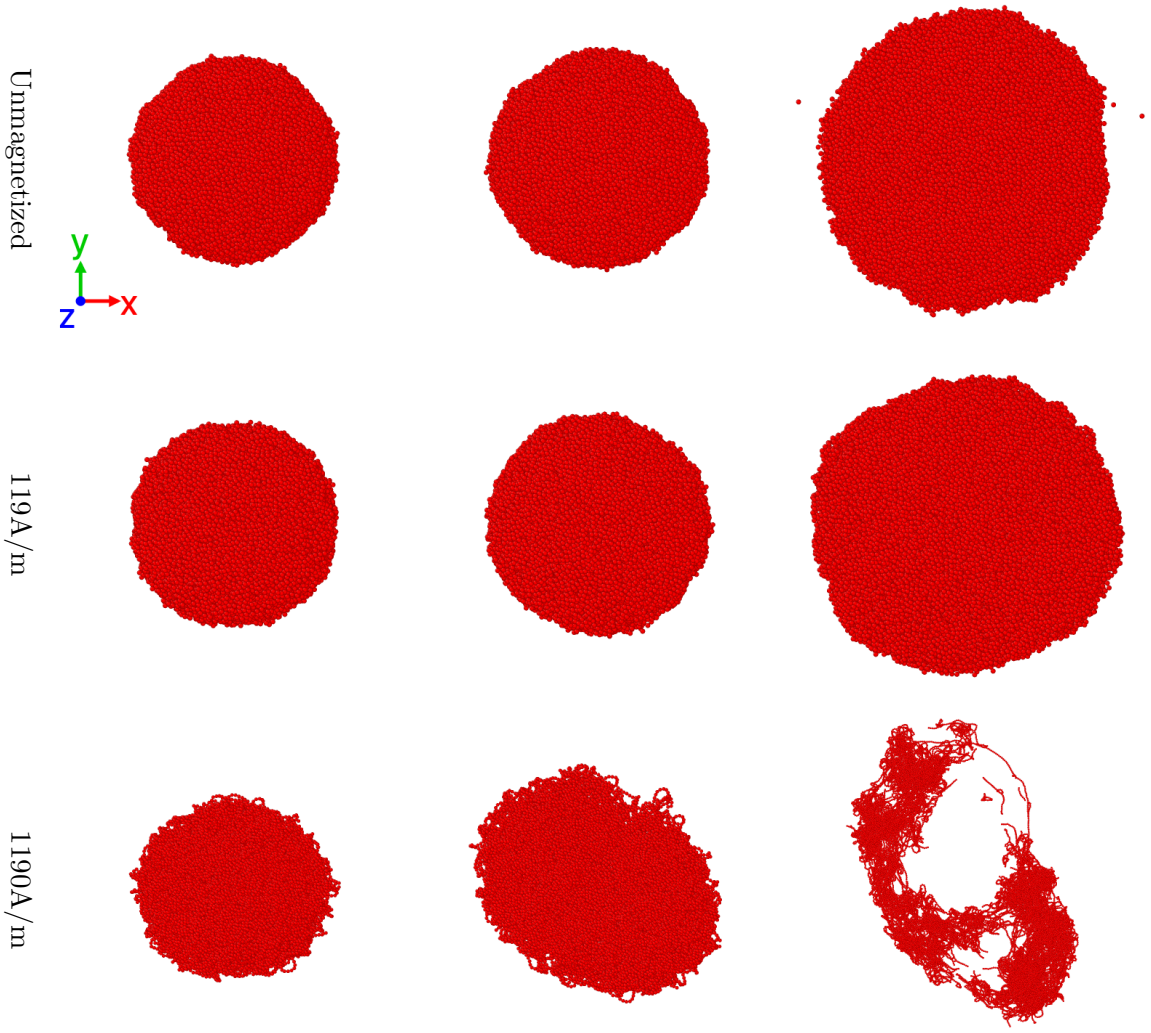

(a) Initialized (b) Deformed (c) Disrupted

Figure 4.7: 50 cm asteroid evolution as they are spun up to increasing angular momentum states, viewed parallel to the spin axis.

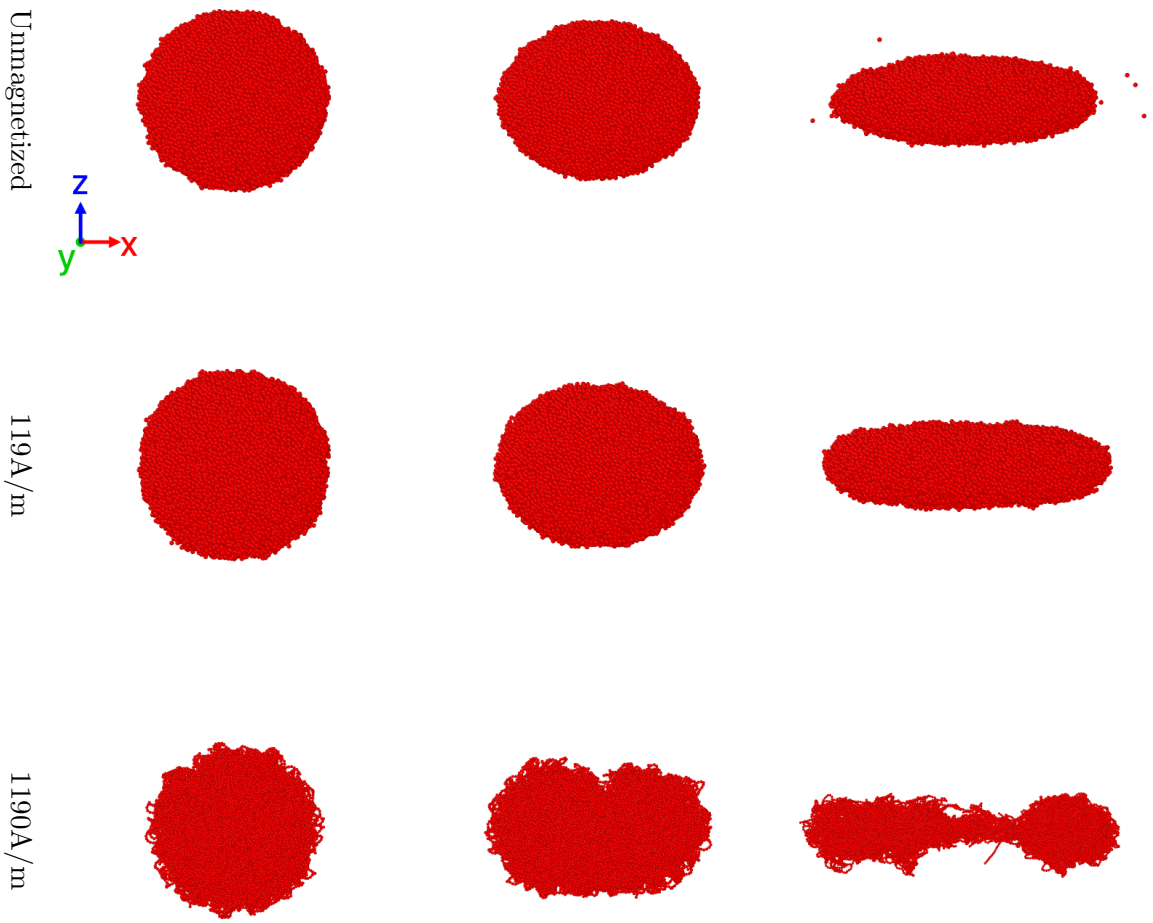

(a) Initialized (b) Deformed (c) Disrupted

Figure 4.8: 50 cm asteroid evolution as they are spun up to increasing angular momentum states, viewed perpendicular to the spin axis

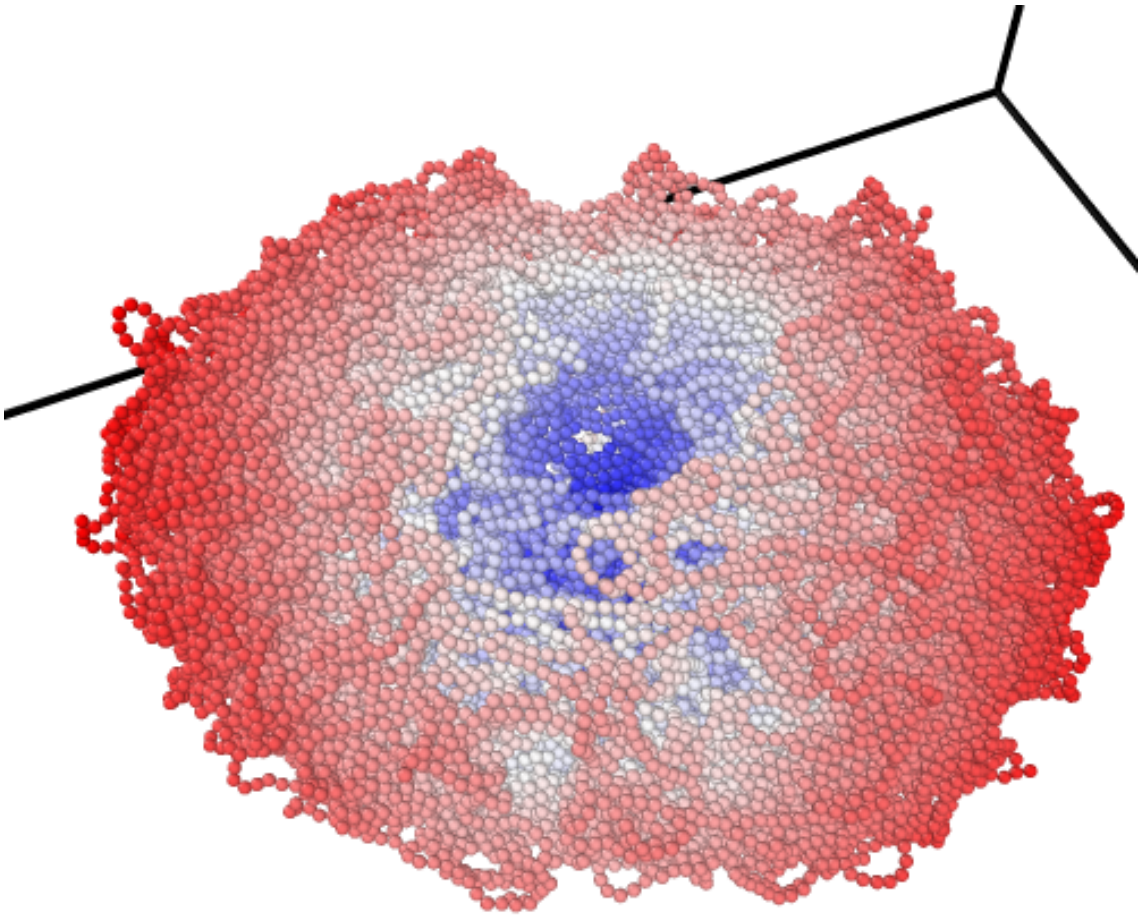

Figure 4.9: Close up of the binary fissure forming in the 50 cm, 1190 A/m asteroid after the deformation event. (Colored by distance from CoM)

mass, at which point they were considered 'disrupted' (figs. 4.7c and 4.8c). The unmagnetized and low magnetization asteroids were disrupted at 700 µrad/s while the high magnetization asteroids disrupted at 800 µrad/s. The low and no magnetization asteroids continued to increase their equatorial bulge until small collections of grains were ejected from local high points along the equator. For these cases the grains separated from high spots around the equator. Of these, several fell back and reaccumulated on the surface of the asteroid, while the others escaped. The highly magnetized asteroids tore themselves apart, leaving behind several large fragments (fig. 4.10). Two of the fragments from the 50 cm asteroid have very large aspect ratios of 6:1 for the largest body and 5:1 for the second largest.

As with the coalescing simulations, the magnetized asteroids had lower initial densities than the unmagnetized asteroids (fig. 4.11). The lower initial densities result in smaller initial strength due to the cohesive and gravitational forces. Despite the reduced strength from conventional sources, the magnetized asteroids disrupted at spin rates greater than or equal to the disruption rates of the unmagnetized asteroids. The reduction in density as the asteroid spun up was more pronounced for the highly magnetized asteroid than for the lower magnetization and unmagnetized asteroids, possibly due to the repulsion of adjacent chains. In contrast, the large grained, unmagnetized asteroid increased in density after deformation, possibly due to stick-slip caused by the cohesion. The remaining low magnetization and unmagnetized asteroids had small decreases in density as they spun up. The highly magnetized asteroids had very low densities, indicating a porosity of 83.6% for the 50 cm grains and 83.0% for the 100 cm grains.

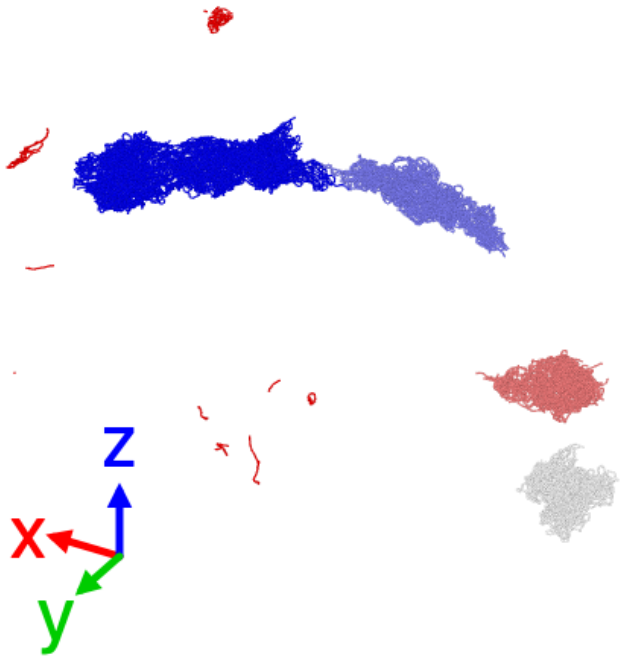

(a) Fragments from the 50 cm, 1190 A/m asteroid after being disrupted. (Colored by Cluster)

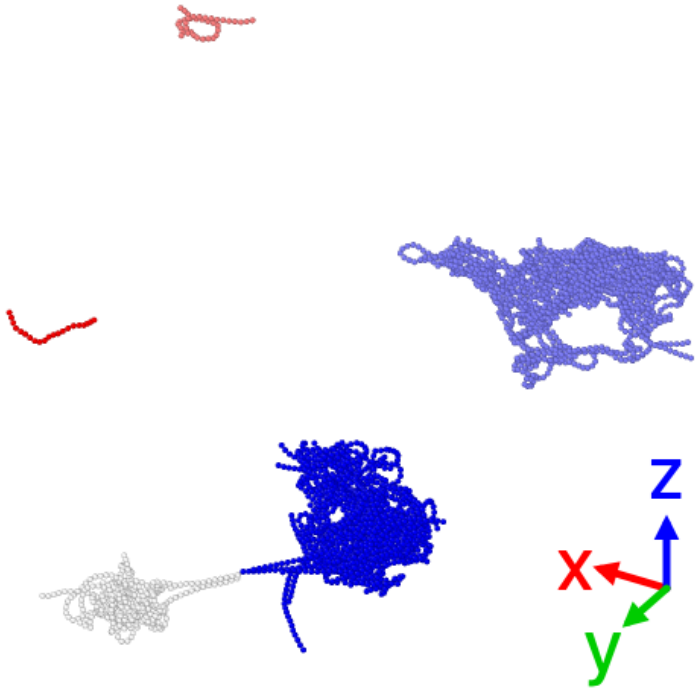

(b) Fragments from the 100 cm, 1190 A/m asteroid after being disrupted. (Colored by Cluster)

Figure 4.10: Fragments left behind after disruption of highly magnetized asteroids

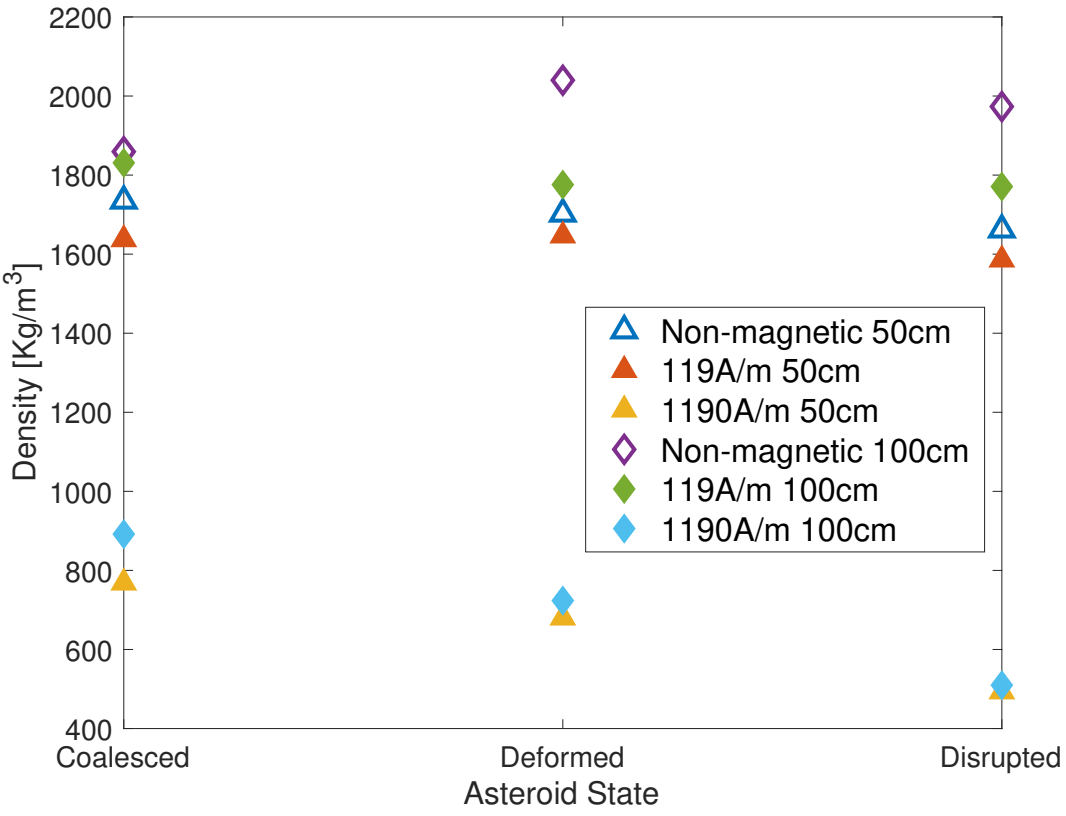

Figure 4.11: Density of asteroids as they are spun up until they are disrupted. The disrupted asteroid density is the density of the largest fragment.

4.4 Mass Wasting

Asteroids with a magnetized core may have grains on the surface with high susceptibility but which have been demagnetized by space weathering phenomenon or have coalesced from unmagnetized dust. The dynamics of these grains avalanching on craters or otherwise shifting on the surface could result in distinctive and identifiable features compared to unmagnetized asteroids.

4.4.1 Simulation

4.4.1.1 Contact Force Model

The mass wasting simulations were run on the open source SSDEM framework LIGGGHTS, which is based off of LAMMPS and optimized to run granular simulations [51]. LIGGGHTS uses the same Hertzian grain contact force as LAMMPS (eq. (4.3)). The cohesion model used in LIGGGHTS is the SJKR model where $F_n = k_c A$ with volume energy density k_c and contact area A. Rolling resistance is handled via an Elastic Plastic Spring Dashpot (EPSD) model where a restoring spring dashpot force provides a torque back to the initial contact point until the maximum torque is exceeded. After that point, the equilibrium point of the spring gets dragged along with the particle rotation, creating a plastic deformation.

4.4.1.2 Magnetic Model

We use soft magnetic grains in the mass wasting simulations. Soft magnetic grains, in contrast to the hard magnets used in the previous simulations, do not maintain their magnetization when an external field is removed. When a soft magnetic grain is placed in an external magnetic field (approximated as constant over the volume of the sphere), it has a dipole induced (eq. (4.11)).

$$\vec{m}_i = 4\pi \frac{\chi - 1}{\chi + 2} R_i^3 \vec{H} = C_{m_i} \vec{B} \tag{4.11}$$

The total dipole moment is the sum of the magnetic dipole induced by each of its neighbors and the background field due to linearity. Because the dipole moment of a soft grain will always be aligned with the local magnetic field, there is no torque induced on the grains, and the torque term is dropped from the model. In order to solve this system numerically we use an iterative, mutual dipole method [19], which uses the dipole moments from the previous iteration to calculate the magnetic field at each grain, which, when multiplied by a constant (C_i) yields its dipole moment (eq. (4.12)). In three iterations, this converges to within 10^{-2} percent of the value at 1000 iterations [table 4.3].

$$\vec{m}_i^k = C_i \left(B_0 + \sum_{j=1, j \neq i}^{n} \vec{B}_j^{k-1} \right) \tag{4.12}$$

The timestep for SSDEM simulations is constrained by particle size and hardness, such that the movement per timestep is small compared to the gradient of

i	P1	P2	P3
1	-23.6301%	-22.9105%	17.0134%
2	-0.6621%	-0.4894%	1.0083%
3	-0.0707%	-0.0476%	0.0804%
4	-0.0044%	-0.0032%	0.0044%

Table 4.3: Force convergence for contacting particles, in an "L" configuration, with three total particles, a central particle (P2) adjacent to one particle aligned with the field (P1) and one perpendicular to the field (P3), using mutual dipole method. Convergence is shown as percent error from values at 1000 iterations.

the magnetic field. Therefore, due to the rapid convergence, rather than iterating multiple times per timestep, we use the dipoles from the previous timestep to find the magnetic fields for magnetizing grains in the current timestep. The model for magnetic interactions and induced dipoles, as implemented in LIGGGHTS has been validated using simulations of magnetorheological fluid shear and jamming using $\sim 10^5$ particles [99, 101] and a more in depth analysis can be found in Leps and Hartzell [99].

4.4.1.3 Initialization

Gravity was set to Psyche surface gravity of $0.144\,\mathrm{m/s^2}$ [138]. The simulation box was initialized with ∼500,000, ∼77,000, and ∼70,000 grains, with 0.005 m, 0.01 m, or 0.05 m diameters respectively and particle properties given in table 4.4. The grains were were created in a rectangular cell, 1.5 m long, by 0.4 m wide by 2 m tall for the two smaller grain sizes and 7.5 m long, by 2 m wide by 10 m tall for the 5 cm grains, with periodic boundaries along the width, and then allowed to settle under gravity. Once the grains had fully settled, a 0.005 T external field was applied

Particle Diameters	0.5 cm	1 cm	5 cm
Density	$7750\,\mathrm{kg/m^3}$		
Young's modulus	$1 \times 10^9\,\mathrm{N/m^2}$		
Coefficient of Restitution	0.2		
Poisson's ratio	0.278		
Surface Energy Density	$10\,\mathrm{J/m^3}$		
Sliding Friction	$\mu_s = 0.6$		
Rolling Friction	$\mu_r = 0.4$, $\gamma_r = 0.4$, $k_r = 10$		

Table 4.4: Simulation particle properties for asteroid avalanching simulations

in the Z direction, parallel to gravity. The grains were allowed to reconfigure in the magnetic field and then the dividing wall was removed, allowing the grains to flow in the Y (long) direction. The grains were allowed to run out into the empty side of the container until they reached equilibrium.

4.4.2 Results

The angles of repose were enhanced by the magnetic forces. The 5 cm grains had their angle of repose increased by 0.4%, the 1 cm grains' angle of repose was enhanced 6.2%, and the 5 mm grains' angle of repose was enhanced 35.6% (table 4.5 and fig. 4.12). The 5 mm grains had two stable angles of repose, their enhanced angle of repose and the unenhanced original angle. The enhanced angle was at the top of the slope, while at the bottom of the slope it transitioned to the original angle (fig. 4.12a). This appears to be due to the momentum of the grains, as they crash into the base, overcoming the magnetic cohesion.

Like the self-gravity simulations, the magnetization of the grains increases porosity of the system. The magnetic field results in an increase in the volume of

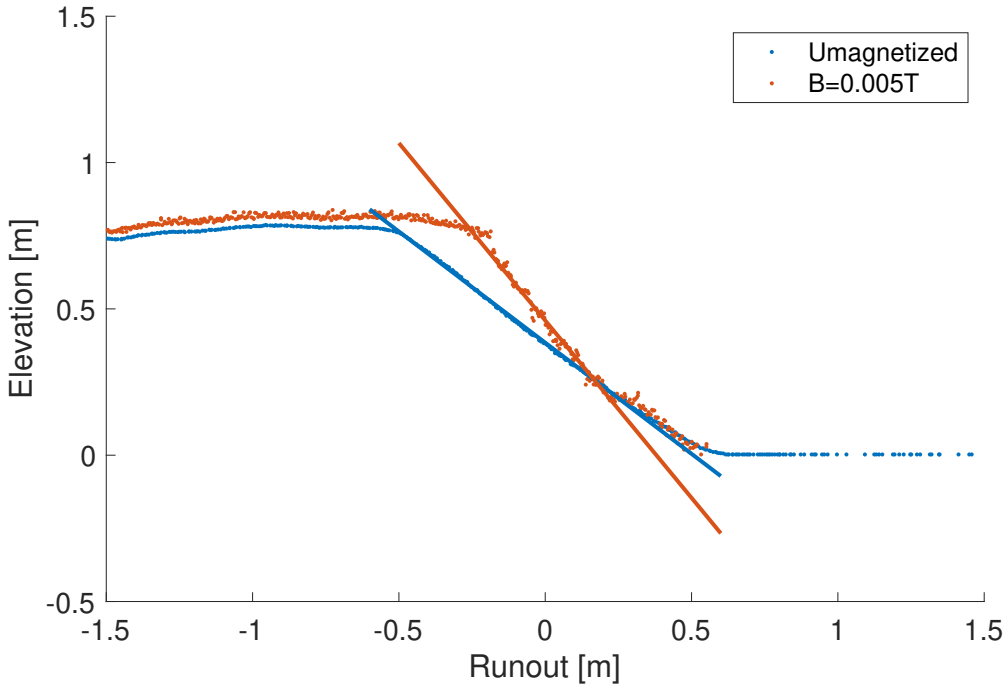

(a) Angle of repose for magnetized and unmagnetized 5 mm grains

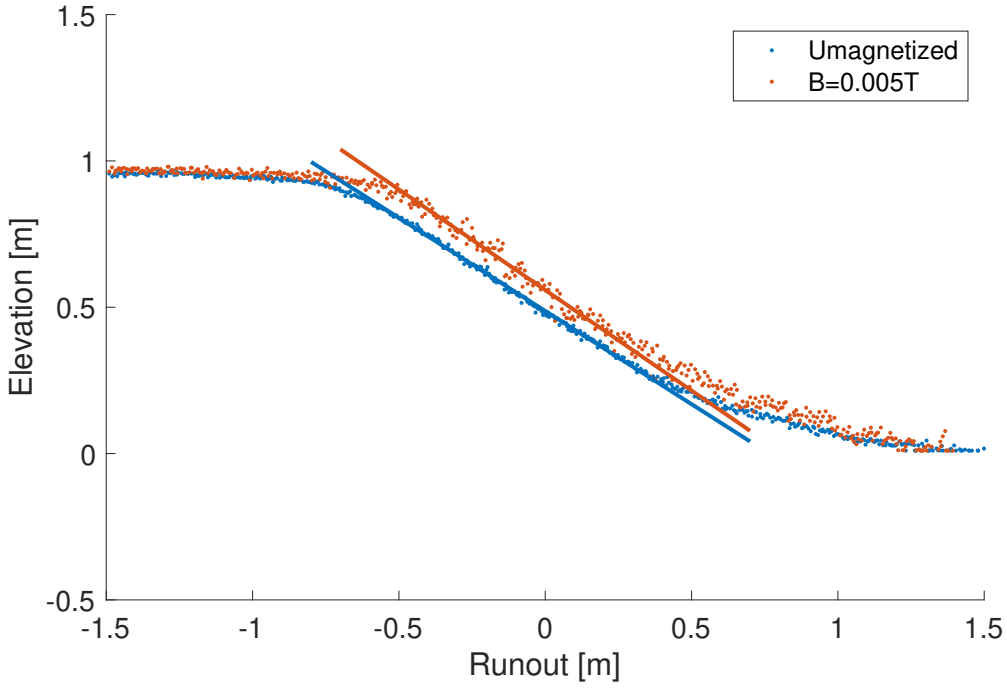

(b) Angle of repose for magnetized and unmagnetized 1 cm grains

Figure 4.12: Angle of repose for avalanched grains

Particle Size	Magnetization	Angle of Respose	Volume
5 mm	Unmagnetized	37.2209°	1.1602 m^3
	Magnetized	50.4837°	1.2659 m^3
1 cm	Unmagnetized	32.4847°	1.4859 m^3
	Magnetized	34.4926°	1.6097 m^3
5 cm	Unmagnetized	31.2953°	37.6239 m^3
	Magnetized	31.4193°	38.1069 m^3

Table 4.5: Characteristics of magnetized slope during avalanching

the 5 mm, 1 cm, and 5 cm grain heaps by 9%, 8% and 1% respectively (table 4.5). The majority of this comes from the near surface grains (fig. 4.13).

4.4.3 Discussion

The increased cohesion from the magnetic forces created an effect in the 5 mm grains similar to calving on snow cornices or glaciers. As the grains ran out down the slope, large chunks of the grain pile would shear off from the top of the slope and fall down the slope relatively intact until they were absorbed into the lower slope (fig. 4.14). This cornicing leaves a distinctive sharp edge at the top of the runout, which may be identifiable in images of asteroid surfaces. The highly magnetized surface also has a dual sloped runout that may also be used to identify magnetization of asteroids (fig. 4.12a).

The increased porosity on the surface of a highly magnetized asteroid may allow it to absorb energy through compression. This has implications for landing missions, which will have to account for the porosity in the design of the landing and anchoring mechanism. It may also have implications for planetary defense if we attempt to deflect a hazardous asteroid with an impactor.

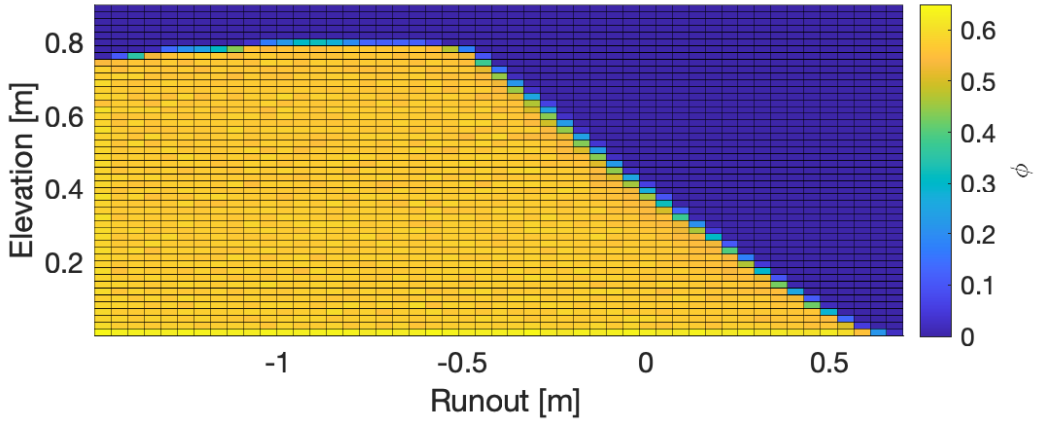

(a) Packing fraction of the 5 mm grain heap without a magnetic field

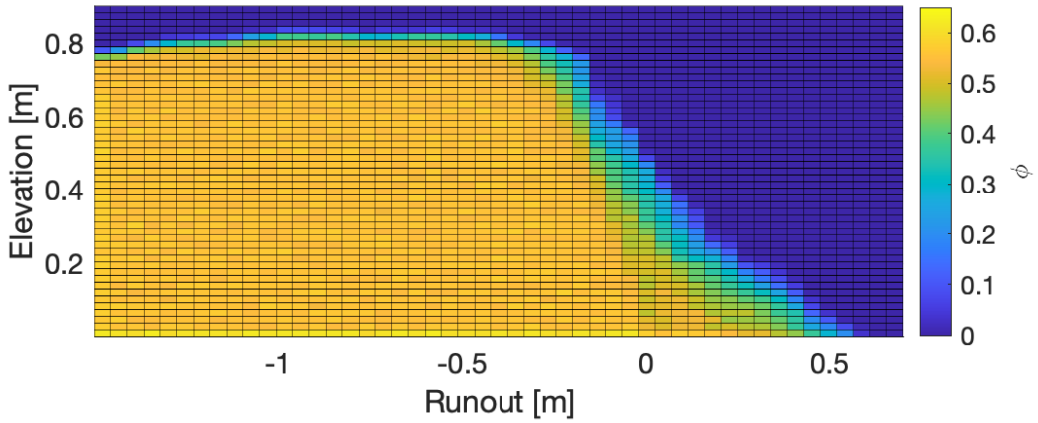

(b) Packing fraction of the 5 mm grain heap with a 0.005 T magnetic field

Figure 4.13: Packing fractions of avalanched grain slope

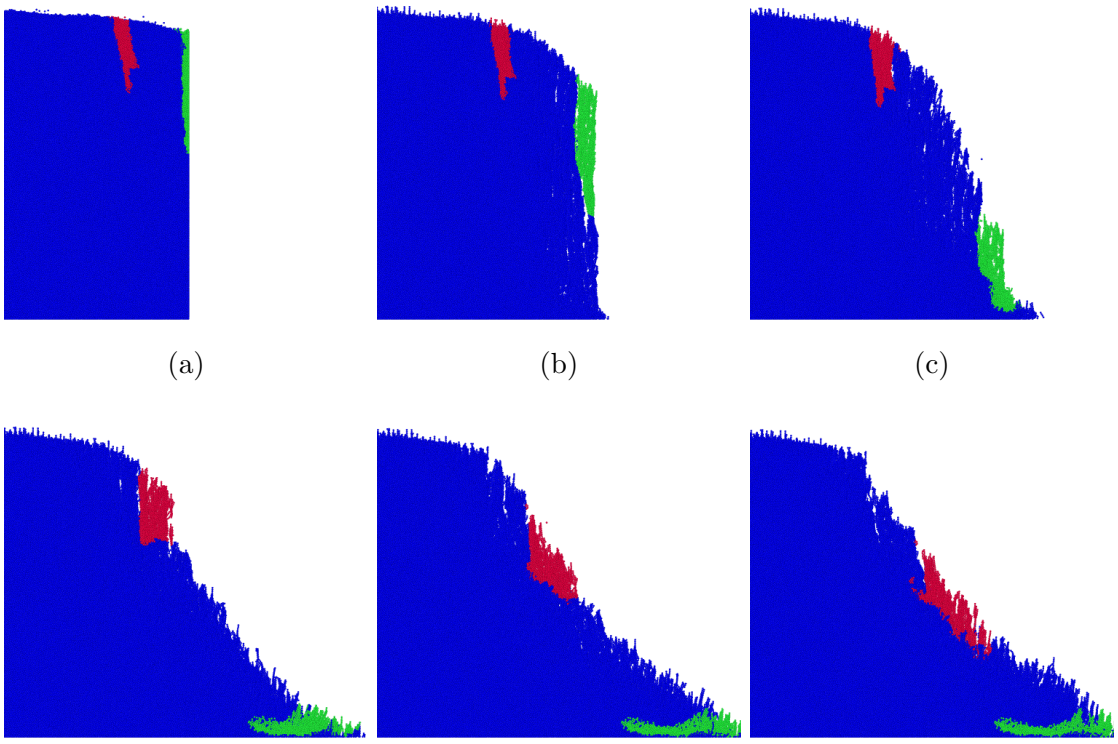

(a) (b) (c)

(d) (e) (f)

Figure 4.14: Calving of two cornices of magnetic grains, from the lip of the grain pile, during grain avalanching of the 5 mm grains in a 5 mT field. Figure 4.14a: Grains before avalanching with two groups of grains that will calve off (red & green). Figure 4.14b: The first cornice (green) calves off of the lip of the grain pile. Figure 4.14c: The first cornice (green) hits the bottom of the cell and begins to compress. Figure 4.14d: The first cornice (green) has been absorbed into the lower slope while the second cornice (red) is calving off of the lip. Figure 4.14e: The second cornice (red) hits the lower slope and begins to compress. Figure 4.14f: The second cornice (red) runs down and begins to get absorbed into the lower slope

4.5 Magnetic Interaction Scaling Forces

It is useful to understand under what circumstances magnetic effects may be relevant to asteroid structure and dynamics. By calculating the forces between two in-line particles, with radius R, aligned with various background field strengths (eqs. (4.1) and (4.12)) and comparing it to the attractive force of various surface gravities (eq. (4.13)), self-gravity (eq. (4.14)), and cohesive force for clean and dirty particles (S=1,0.1) (eq. (4.15)) [89], we can find when magnetism is a significant force for determining asteroid strength (figs. 4.15 and 4.16). Forces between axially aligned, permanently magnetized particles, with magnetizations equal to those created by placing individual, soft magnetic particles in a uniform background field, are within 30% of the forces using the mutual dipole method and the two are indistinguishable in the log-log plots in figs. 4.15 and 4.16 so they have been omitted. Background fields of 5×10^{-7} T, 5×10^{-6} T, 5×10^{-5} T, 5×10^{-4} T, and 5×10^{-3} T, result in magnetizations in individual spheres of 1.19 A/m, 11.9 A/m, 119 A/m, 1190 A/m, and 11 900 A/m respectively.

$$F_{gSurf} = \rho \frac{4}{3} \pi R^3 g \tag{4.13}$$

$$F_{gSelf} = G(\rho \frac{1}{3} \pi R^2)^2 \tag{4.14}$$

$$F_c = 3.6e - 2 \times S^2 R \tag{4.15}$$

The slope of the magnetic forces lies between the slope of the cohesive and surface gravity forces in a log-log plot. For small particles the cohesive forces will tend to be the dominant force, while large particles tend to be dominated by gravity. Medium sized grain forces can potentially be dominated by magnetism for some magnetic fields/magnetizations, surface gravities, and cleanliness coefficients. Magnetic forces will dominate for particles in an 5×10^{-4} T field with a cleanliness of 0.1, in a surface gravity of $10^{-4}\,\mathrm{m/s^2}$, for particle sizes ranging from $\sim 10^{-4}\,\mathrm{m} - 10^{-1}\,\mathrm{m}$, for example. Self gravity has the largest slope and does not dominate until much larger grain sizes, on the order of 10's-100's of meters.

4.6 Discussion

Both grain magnetizations during coalescing and disruption resulted in considerably lower bulk magnetization than the magnetizations measured at Braille and Gaspra of 110 A/m and 93 A/m. Based on the trend from our simulations, it's possible that an additional order of magnitude of grain magnetization over the maximum from our simulations would still have a bulk magnetization below that of Gaspra and Braille.

The higher rate of coalescence in the magnetized asteroids means that metallic cores of protoplanetary embryos may have been able to form faster, speeding planet forming during the early solar system. Further simulations of the protoplanetary disk during the formation of the solar system, which include magnetic forces, will provide insight into the importance of magnetism during planet formation.

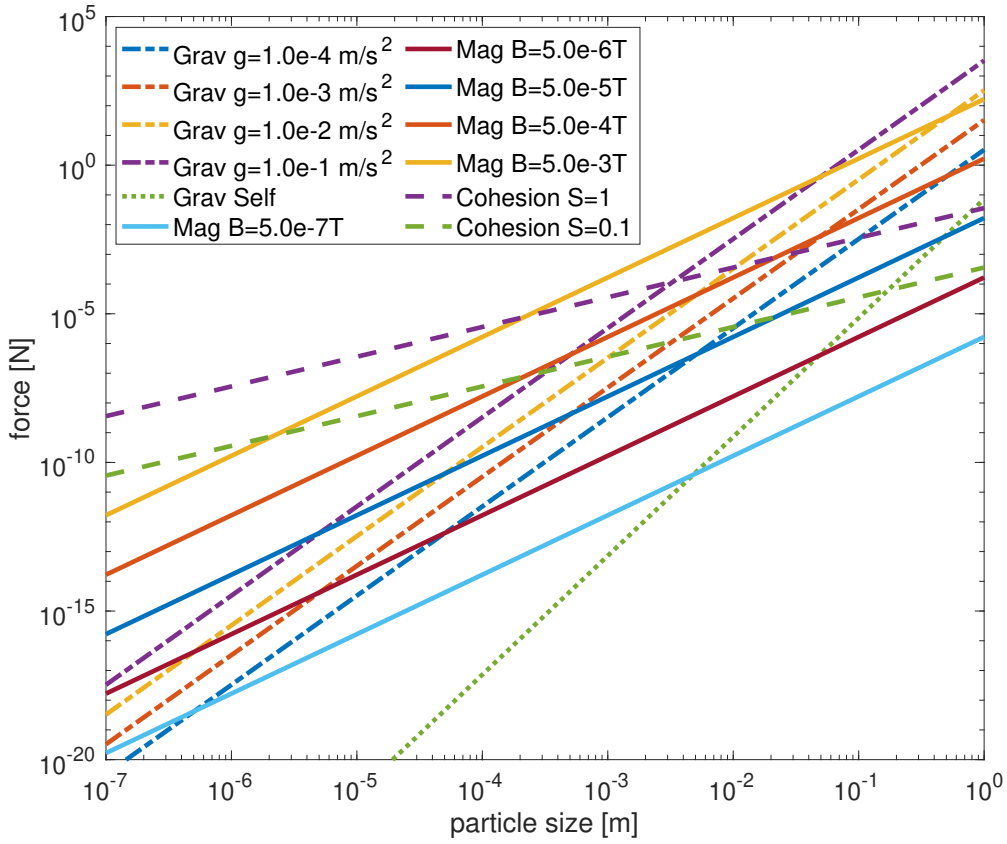

Figure 4.15: Forces on an iron particle from surface gravity, self-gravity and cohesion with a contacting grain of equal size, and dipole-dipole interactions between two equal sized soft magnetic grains, in contact, aligned with a background field, at the surface of a metallic asteroid. For several particle sizes and background field strengths, the dipole-dipole force dominates over gravity and cohesion. The magnetic dipole interactions tend to dominate at middle particle sizes $\sim 10^{-4}$ m - 1 m. Above these sizes, gravity tends to dominate and below these sizes, cohesion begins to take over.

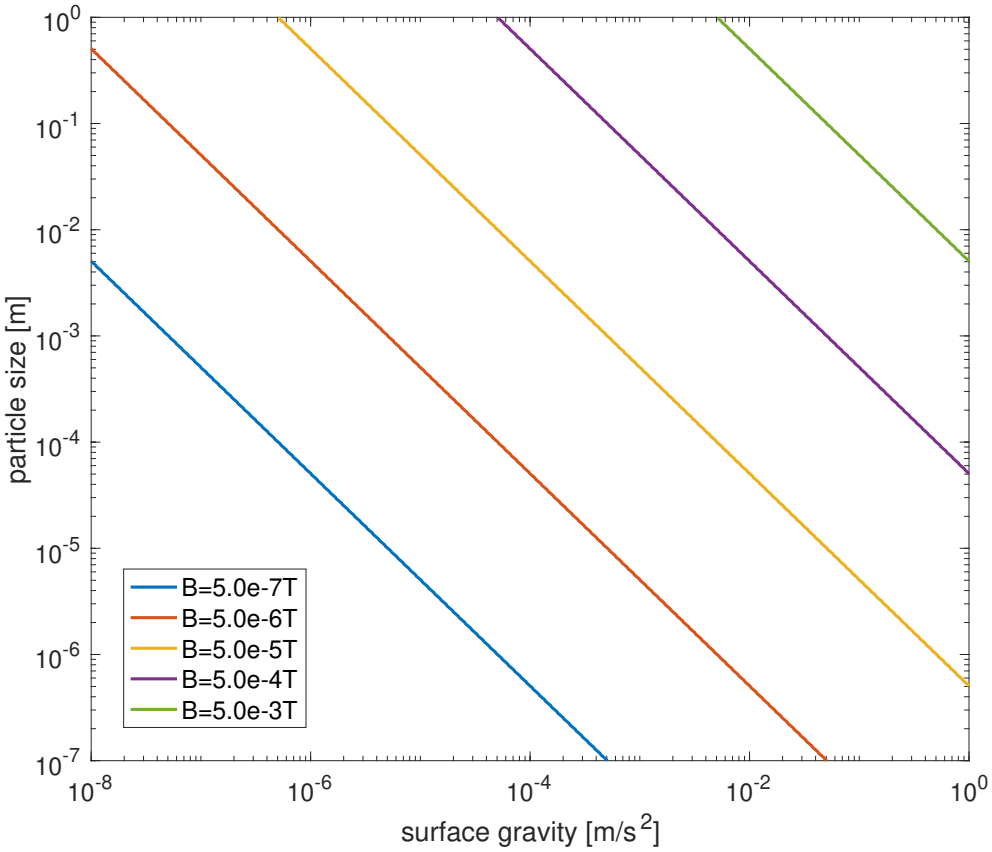

Figure 4.16: Lines of equal force between surface gravity and magnetic attraction between two magnetically susceptible grains in a background field. Magnetism dominates under the lines for the various magnetic field strengths.

The disruption patterns we found with magnetism match those found by Sanchez for high friction angle asteroids, which similarly use both rolling resistance and surface friction, and varying levels of internal strength [33]. Large strengths resulted in fissures with multiple large fragments, while lower strengths resulted in the shedding of individual grains or small clumps of grains from the equatorial region. The resulting fragments created from magnetized asteroids had some morphological differences from the Sanchez results and most observations of small bodies, such as high aspect ratios and porosities.

The fragments formed by the disruption of the highly magnetized asteroid have some similarities to two objects with unusual shapes. 216 Kleopatra has a shape very similar to one of the fragments from our simulations, with a long skinny middle connecting two larger ends, though Kleopatra is several orders of magnitude larger (fig. 4.17)[95]. 1I/2017 U1 'Oumuamua was found to have an aspect ratio of likely 6:1 and as high as 10:1 and a spectra consistent with a high metallicity. The high aspect ratios for 1I/2017 U1 are consistent with the aspect ratios seen in our disruption simulations with highly magnetized grains of 6:1 and 5:1. 'Oumuamua also experienced a high extra-gravitational acceleration as it went through perihelion, which could be consistent with a density much lower than expected. The high porosities in the high aspect ratio fragments of our simulations may be able to explain some of the accelerations observed.

In the asteroid strength simulations, the surface gravity was approximately $5 \times 10^{-6}\,\mathrm{m/s^2}$ and the equivalent background field to the highly magnetized, 1190 A/m, grains is $5 \times 10^{-5}\,\mathrm{T}$. At that surface gravity and magnetization, gravity slightly

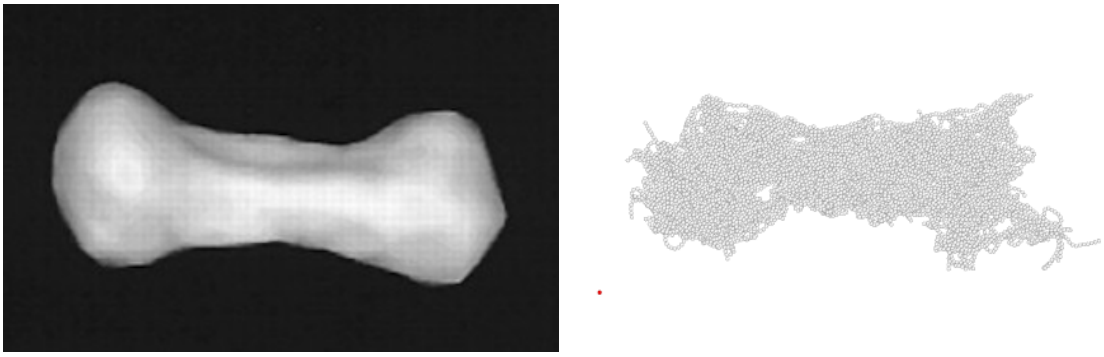

(a) 216 Kleopatra

(b) Fragment from 50 cm magnetized asteroid

Figure 4.17: Comparison between 216 Kleopatra and a fragment of the 50 cm grain, 1190 A/m, magnetized asteroid simulation. The scale of the images is several orders of magnitude off, with Kleopatra having a major axis of approximately 200 km while the fragment has a major axis of just 63 m, however the shape is very similar.

dominates for 100 cm grains, and magnetism slightly dominates for 50 cm grains. At 119 A/m gravity strongly dominates magnetism (fig. 4.16). This agrees with the results of the simulations where the largest differences due to magnetism were seen in the 50cm grains at high magnetization. At the lower magnetization, where gravity significantly dominated, the morphological changes were limited to slightly higher surface porosities.

The avalanching results also agree with the force scales. With 0.14 m/s^2 surface gravity, and a 5 mT background field, magnetic forces will dominate over gravity by an order of magnitude for iron grains with 5 mm diameters. For grains with a 1 cm diameter gravity and magnetism will be comparable, with magnetism slightly more powerful than gravity for contacting grains. For 5 cm grains gravity will be slightly more powerful than gravity. Our simulations showed that the 5 mm grain simulations had higher porosities, steeped angles of repose compared to the unmagnetized simulations, and a cornicing behavior which was not present in unmagnetized sim-

ulations. The 1 cm grains were slightly affected, with an increased angle of repose and increased porosity, mostly at the surface where the additional weight of grains above them were not a factor. The 5 cm grains were mostly unaffected by magnetism (figs. 4.15 and 4.16).

Further simulations with larger asteroids and a distribution of particle sizes instead of monodisperse particles may provide further insight into the effects of magnetism on asteroid formation and evolution.

4.7 Conclusion

Magnetic forces in the range of what could reasonably exist in metallic asteroids, based on observations from DS1, the Galileo spacecraft, and meteorites, can have a significant impact on asteroid formation, morphology, and strength. Using magnetic models, validated with simulations of magnetorheological fluid, we simulated the formation, disruption, and mass wasting on metallic asteroids. Magnetized grains resulted in faster coalescence of dust clouds. The resulting asteroids had increased internal strength, allowing higher spin rates before disruption, lower bulk densities, and lower surface densities. Avalanching of induced magnetic dipoles on the surface of a large asteroid showed increased angles of repose and reduced regolith densities. These morphological differences will allow us to better prepare for future missions to potentially magnetized bodies and give us a better understanding of the dynamics of planet core formation in the early solar system. Some of the characteristics found in these simulations can also be searched for in the upcoming Psyche

mission as well as other observations of m-type asteroids as an indirect indicator for magnetization.

Chapter 5: Conclusion

5.1 Contributions

We have implemented a mutual dipole magnetic model into the LIGGGHTS and LAMMPS DEM framework and shown that including the mutual dipole method with high fidelity granular interaction models the behavior of MRF systems can be reproduced for multiple modes of operation. We captured the shear yield stress behavior of MRFs in simple shear cells, matching the yield behavior as well as the low shear rate shear stress roll off and the bidisperse mixture yield enhancement. Our simulations show that the inclusion of an accurate particle distribution and a complete suite of contact forces (Hertz-Mindlin elastic deformation, rolling friction and cohesion) are necessary to properly simulate MRF behavior. In addition to shear behavior, we were able to capture jamming behavior in a novel MRF valve design, using our simulation model coupled with FEA to predict magnetic fields.

We developed an ElectroPermanent Magnet (EPM) actuated jamming MRF valve. Our valve design is an order of magnitude smaller than the smallest previous MRF valves. In addition, the valve requires no quiescent current to maintain the on or off state, leading to average power draw several orders of magnitude lower than current MRF valves for expected duty cycles. Despite the compact size and zero

power draw, our valve design is able to arrest flow with hundreds of kilopascals of pressure drop across the valve and still reliably reverse the jamming transition.

We integrated the EPM, jamming MRF valve into a multi-segmented, elastomeric soft robot allowing independent control of multiple segments with a single fluid supply channel and minimal wiring infrastructure. Due to the compact nature of the valve and low cost, it allows for control of a many segmented soft robot, enabling unprecedented degrees of freedom for an elastomeric robot design.

Using the DEM model developed for MRF simulation, we were able to model magnetized metallic asteroids coalescing and disrupting, finding unique morphologies that result from magnetization, which could be identifiable by radio astronomy observations and in future flyby and rendezvous missions. The addition of magnetism in metallic asteroids resulted in faster accretion from a rotating, self-gravitating particle cloud and the resultant objects had higher porosities than their unmagnetized counterparts. The magnetized asteroids also had higher internal strengths, being able to maintain higher spin rates before deforming and disrupting. Once disrupted, the magnetized asteroid fragments exhibited shapes with higher aspect ratios and porosities than unmagnetized fragments. Some of the fragments matched the shapes of observed, suspected metallic objects 'Oumuamua and Kleopatra, which have shapes that are unusual for objects formed with just non-magnetic forces.

Simulating mass wasting on the surface of a metallic asteroid again found changes in morphology compared to unmagnetized grains. Avalanching magnetized grains resulted in higher porosity in the runout and higher angles of repose. Also,

magnetized grains could form cohesive clumps, which broke off from the lip of the grain piles, in an action similar to calving of glaciers or cornices. The calving process resulted in a two slope runout, with a steep slope at the top dominated by magnetic cohesion, and a shallower slope at the bottom where the impact forces overcame magnetism and the clumps crumbled.

In addition to the results of our simulations, we have created an open source tool for further investigating magnetic, granular interactions. We are making our code available for use by the community at large.

5.2 Future Work

Our MRF model used a simple, uncoupled fluid dynamics model. In the case of the Couette flow in simple shear cells this approximation is very accurate. Due to the presence of no-slip boundary conditions on the two surfaces and symmetry of the system the actual fluid flow can be predicted and relative velocity of the particles and the background fluid should be very low. In more complicated geometries, the background fluid flow cannot be accurately predicted and so a coupled fluid dynamics model is desirable for higher fidelity. The developers of LIGGGHTS have implemented a coupled CFD-DEM model using OpenFOAM integrated with LIGGGHTS. Using the OpenFOAM CFD-DEM framework to simulate more complex systems will provide insights into realistic applications of MRF fluids.

Further validation of the model can be performed using dry, magnetic particle experiments. Segregation experiments involving mixtures of non-magnetic, soft

magnetic and hard magnetic particles, currently underway, will provide an additional data set. Accurately reproducing these experiments in LIGGGHTS with magnetism would give the model three independent sources of validation, increasing confidence in its predictions for magnetized asteroids. Experiments are also planned that will directly validate simulation results on the avalanching of magnetic grains in a background magnetic field.

Asteroid simulations could be carried out with a more disperse mixture of particle sizes and a variety of particle properties creating better data sets for comparison to shape models from future observations. Additionally, simulations of disruptions by impactors can be performed. Simulating an impact disruption of a proto-planetary embryo with a differentiated mixture of metallic and rocky grains would provide evidence for or against the theory that m-type asteroids can result from these impacts. Impactor simulations can also help with planetary defense planning, providing data on how the impact will be affected by magnetized grains and how the resultant the trajectories compared to unmagnetized asteroids. The bulk properties of magnetic grains can be analyzed to find analogs to angle of friction and tensile strengths for non-isotropic forces.

Bibliography

[1] Norman M. Wereley. *Magnetorheology*. Smart Materials Series. The Royal Society of Chemistry, 2014.

[2] A.-M. TRENDLER and H. BÖSE. Influence of particle size on the rheological properties of magnetorheological suspensions. *International Journal of Modern Physics B*, 19(07n09):1416–1422, 2005. doi: 10.1142/S0217979205030384. URL https://doi.org/10.1142/S0217979205030384.

[3] Jun Ai, Jian-Fei Chen, J. Michael Rotter, and Jin Y. Ooi. Assessment of rolling resistance models in discrete element simulations. *Powder Technology*, 206 (3):269 – 282, 2011. ISSN 0032-5910. doi: https://doi.org/10.1016/j.powtec.2010.09.030. URL http://www.sciencedirect.com/science/article/pii/S0032591010005164.

[4] K. Hutter and K. R. Rajagopal. On flows of granular materials. *Continuum Mechanics and Thermodynamics*, 6(2):81–139, 1994. doi: 10.1007/BF01140894. URL https://doi.org/10.1007/BF01140894.

[5] Sergei E. Esipov and Thorsten Pöschel. The granular phase diagram. *Journal of Statistical Physics*, 86(5):1385–1395, 1997. doi: 10.1007/BF02183630. URL https://doi.org/10.1007/BF02183630.

[6] Daniel L Blair and Arshad Kudrolli. Magnetized granular materials. *The Physics of Granular Media*, pages 281–296, 2004.

[7] B. Andreotti, Y. Forterre, and O. Pouliquen. *Granular Media: Between Fluid and Solid*. Cambridge University Press, 2013. ISBN 9781107034792. URL https://books.google.com/books?id=2ekG3NYgpqsC.

[8] J. F. Peters, M. Muthuswamy, J. Wibowo, and A. Tordesillas. Characterization of force chains in granular material. *Phys. Rev. E*, 72:041307, Oct 2005. doi: 10.1103/PhysRevE.72.041307. URL https://link.aps.org/doi/10.1103/PhysRevE.72.041307.

[9] Karen E. Daniels and Nicholas W. Hayman. Force chains in seismogenic faults visualized with photoelastic granular shear experiments. *Journal of Geophysical Research: Solid Earth*, 113(B11), 2008. doi: https://doi.org/10.1029/2008JB005781. URL https://agupubs.onlinelibrary.wiley.com/doi/abs/10.1029/2008JB005781.

[10] Nariman Mahabadi and Jaewon Jang. The impact of fluid flow on force chains in granular media. *Applied Physics Letters*, 110(4):041907, 2017. doi: 10.1063/1.4975065. URL https://doi.org/10.1063/1.4975065.

[11] Aghil Abed Zadeh, Jonathan Barés, Theodore A. Brzinski, Karen E. Daniels, Joshua Dijksman, Nicolas Docquier, Henry O. Everitt, Jonathan E. Kollmer, Olivier Lantsoght, Dong Wang, Marcel Workamp, Yiqiu Zhao, and Hu Zheng. Enlightening force chains: a review of photoelasticimetry in granular matter. *Granular Matter*, 21(4):83, 2019. doi: 10.1007/s10035-019-0942-2. URL https://doi.org/10.1007/s10035-019-0942-2.

[12] L. B. Wang, J. D. Frost, and J. S. Lai. Three-dimensional digital representation of granular material microstructure from x-ray tomography imaging. *Journal of Computing in Civil Engineering*, 18(1):28–35, 2004. doi: 10.1061/(ASCE)0887-3801(2004)18:1(28). URL https://ascelibrary.org/doi/abs/10.1061/%28ASCE%290887-3801%282004%2918%3A1%2828%29.

[13] E. Andò, G. Viggiani, S. A. Hall, and J. Desrues. Experimental micromechanics of granular media studied by x-ray tomography: recent results and challenges. *Géotechnique Letters*, 3(3):142–146, 2013. doi: 10.1680/geolett.13.00036. URL https://doi.org/10.1680/geolett.13.00036.

[14] S. A. Hall and J. Wright. Three-dimensional experimental granular mechanics. *Géotechnique Letters*, 5(4):236–242, 2015. doi: 10.1680/jgele.15.00094. URL https://doi.org/10.1680/jgele.15.00094.

[15] R. C. Hurley, S. A. Hall, and J. P. Wright. Multi-scale mechanics of granular solids from grain-resolved x-ray measurements. *Proceedings of the Royal Society A: Mathematical, Physical and Engineering Sciences*, 473(2207):20170491, 2017. doi: 10.1098/rspa.2017.0491. URL https://royalsocietypublishing.org/doi/abs/10.1098/rspa.2017.0491.

[16] John David Jackson. *Classical electrodynamics*. Wiley, New York, 1999. ISBN 047130932X 9780471309321. URL http://catdir.loc.gov/catdir/toc/onix04/97046873.html.

[17] M Mohebi, N Jamasbi, and J Liu. Simulation of the formation of nonequilibrium structures in magnetorheological fluids subject to an external magnetic field. *Phys Rev E Stat Phys Plasmas Fluids Relat Interdiscip Topics*, 54(5):5407–5413, Nov 1996. ISSN 1063-651X (Print); 1063-651X (Linking). doi: 10.1103/physreve.54.5407.

[18] H.V Ly, F Reitich, M.R Jolly, H.T Banks, and K Ito. Simulations of particle dynamics in magnetorheological fluids. *Journal of Computational Physics*, 155(1):160 – 177, 1999. ISSN 0021-9991. doi: https://doi.org/10.1006/jcph.1999.6335. URL http://www.sciencedirect.com/science/article/pii/S0021999199963350.

[19] Eric E. Keaveny and Martin R. Maxey. Modeling the magnetic interactions between paramagnetic beads in magnetorheological fluids. *Journal of Computational Physics*, 227(22):9554 – 9571, 2008. ISSN 0021-9991. doi: https://doi.org/10.1016/j.jcp.2008.07.008. URL http://www.sciencedirect.com/science/article/pii/S0021999108003677.

[20] K. Han, Y. T. Feng, and D. R. J. Owen. Three-dimensional modelling and simulation of magnetorheological fluids. *International Journal for Numerical Methods in Engineering*, 84(11):1273–1302, 2010. doi: 10.1002/nme.2940. URL https://onlinelibrary.wiley.com/doi/abs/10.1002/nme.2940.

[21] Steven G. Sherman, Derek A. Paley, and Norman M. Wereley. Massively Parallel Simulations of Chain Formation and Restructuring Dynamics in a Magnetorheological Fluid. ASME 2011 Conference on Smart Materials, Adaptive Structures and Intelligent Systems, Volume 1:651–658, 09 2011. doi: 10.1115/SMASIS2011-5188. URL https://doi.org/10.1115/SMASIS2011-5188.

[22] Stephen G. Sherman, Derek A. Paley, and Norman M. Wereley. Parallel simulation of transient magnetorheological direct shear flows using millions of particles. *IEEE Transactions on Magnetics*, 48(11):3517 – 3520, 2012. doi: 10.1109/TMAG.2012.2201214.

[23] S. G. Sherman and N. M. Wereley. Effect of particle size distribution on chain structures in magnetorheological fluids. *IEEE Transactions on Magnetics*, 49(7):3430–3433, July 2013. ISSN 1941-0069. doi: 10.1109/TMAG.2013.2245409.

[24] Ali Ghaffari, Seyed Hassan Hashemabadi, and Mahshid Ashtiani. A review on the simulation and modeling of magnetorheological fluids. *Journal of Intelligent Material Systems and Structures*, 26(8):881–904, 2015. doi: 10.1177/1045389X14546650. URL https://doi.org/10.1177/1045389X14546650.

[25] Hanna G. Lagger, Thomas Breinlinger, Jan G. Korvink, Michael Moseler, Alberto Di Renzo, Francesco Di Maio, and Claas Bierwisch. Influence of hydrodynamic drag model on shear stress in the simulation of magnetorheological fluids. *Journal of Non-Newtonian Fluid Mechanics*, 218:16 – 26, 2015. ISSN 0377-0257. doi: https://doi.org/10.1016/j.jnnfm.2015.01.010. URL http://www.sciencedirect.com/science/article/pii/S0377025715000221.

[26] Inderjit Chopra and Jayant Sirohi. *Smart Structures Theory*. Cambridge Aerospace Series. Cambridge University Press, 2013. doi: 10.1017/CBO9781139025164.

[27] C. P. Sonett. Evidence for a primordial magnetic field during the meteorite parent body era. *Geophysical Research Letters*, 5(2):151–154, 1978. doi: https://doi.org/10.1029/GL005i002p00151. URL https://agupubs.onlinelibrary.wiley.com/doi/abs/10.1029/GL005i002p00151.

[28] M. G. Kivelson, C. F. Kennel, R. L. McPherron, C. T. Russell, D. J. Southwood, R. J. Walker, K. K. Khurana, P. J. Coleman, C. M. Hammond, V. Angelopoulos, A. J. Lazarus, R. P. Lepping, and T. J. Hughes. The galileo earth encounter: Magnetometer and allied measurements. *Journal of Geophysical Research: Space Physics*, 98(A7):11299–11318, 1993. doi: https://doi.org/10.1029/92JA03001. URL https://agupubs.onlinelibrary.wiley.com/doi/abs/10.1029/92JA03001.

[29] I. Richter, D. E. Brinza, M. Cassel, K.-H. Glassmeier, F. Kuhnke, G. Musmann, C. Othmer, K. Schwingenschuh, and B. T. Tsurutani. First direct magnetic field measurements of an asteroidal magnetic field: Ds1 at braille. *Geophysical Research Letters*, 28(10):1913–1916, 2001. doi: 10.1029/2000GL012679. URL https://agupubs.onlinelibrary.wiley.com/doi/abs/10.1029/2000GL012679.

[30] Derek C. Richardson, Pradeep Elankumaran, and Robyn E. Sanderson. Numerical experiments with rubble piles: equilibrium shapes and spins. *Icarus*, 173(2):349–361, 2005. ISSN 0019-1035. doi: https://doi.org/10.1016/j.icarus.2004.09.007. URL https://www.sciencedirect.com/science/article/pii/S0019103504003124.

[31] D.C. Richardson, P. Michel, K.J. Walsh, and K.W. Flynn. Numerical simulations of asteroids modelled as gravitational aggregates with cohesion. *Planetary and Space Science*, 57(2):183–192, 2009. ISSN 0032-0633. doi: https://doi.org/10.1016/j.pss.2008.04.015. URL https://www.sciencedirect.com/science/article/pii/S0032063308001037. Catastrophic Disruption in the Solar System.

[32] Paul Sánchez and Daniel J. Scheeres. SIMULATING ASTEROID RUBBLE PILES WITH a SELF-GRAVITATING SOFT-SPHERE DISTINCT ELEMENT METHOD MODEL. *The Astrophysical Journal*, 727(2):120, jan 2011. doi: 10.1088/0004-637x/727/2/120. URL https://doi.org/10.1088/0004-637x/727/2/120.

[33] Paul Sánchez and Daniel J. Scheeres. Disruption patterns of rotating self-gravitating aggregates: A survey on angle of friction and tensile strength. *Icarus*, 271:453 – 471, 2016. ISSN 0019-1035. doi: https://doi.org/10.1016/j.icarus.2016.01.016. URL http://www.sciencedirect.com/science/article/pii/S0019103516000208.

[34] Kevin J. Walsh. Rubble pile asteroids. *Annual Review of Astronomy and Astrophysics*, 56(1):593–624, 2018. doi: 10.1146/annurev-astro-081817-052013. URL https://doi.org/10.1146/annurev-astro-081817-052013.

[35] A. N. Norris and D. L. Johnson. Nonlinear Elasticity of Granular Media. *Journal of Applied Mechanics*, 64(1):39–49, 03 1997. ISSN 0021-8936. doi: 10.1115/1.2787292. URL https://doi.org/10.1115/1.2787292.

[36] Antonio Coniglio and Mario Nicodemi. The jamming transition of granular media. *Journal of Physics: Condensed Matter*, 12(29):6601–6610, jul 2000. doi: 10.1088/0953-8984/12/29/331. URL https://doi.org/10.1088/0953-8984/12/29/331.

[37] H. P. Zhang and H. A. Makse. Jamming transition in emulsions and granular materials. *Phys. Rev. E*, 72:011301, Jul 2005. doi: 10.1103/PhysRevE.72.011301. URL https://link.aps.org/doi/10.1103/PhysRevE.72.011301.

[38] Aaron S. Keys, Adam R. Abate, Sharon C. Glotzer, and Douglas J. Durian. Measurement of growing dynamical length scales and prediction of the jamming transition in a granular material. *Nature Physics*, 3(4):260–264, 2007. doi: 10.1038/nphys572. URL https://doi.org/10.1038/nphys572.

[39] T. S. Majmudar, M. Sperl, S. Luding, and R. P. Behringer. Jamming transition in granular systems. *Phys. Rev. Lett.*, 98:058001, Jan 2007. doi: 10.1103/PhysRevLett.98.058001. URL https://link.aps.org/doi/10.1103/PhysRevLett.98.058001.

[40] Su-San Park and Eung Soo Kim. Jamming probability of granular flow in 3d hopper with shallow columns: Dem simulations. *Granular Matter*, 22(4):77, 2020. doi: 10.1007/s10035-020-01050-w. URL https://doi.org/10.1007/s10035-020-01050-w.

[41] R. A. Davis and H. Deresiewicz. A discrete probabilistic model for mechanical response of a granular medium. *Acta Mechanica*, 27(1):69–89, 1977. doi: 10.1007/BF01180077. URL https://doi.org/10.1007/BF01180077.

[42] D. H. Trollope and B. C. Burman. Physical and numerical experiments with granular wedges. *Géotechnique*, 30(2):137–157, 1980. doi: 10.1680/geot.1980.30.2.137. URL https://doi.org/10.1680/geot.1980.30.2.137.

[43] P. A. Cundall and O. D. L. Strack. A discrete numerical model for granular assemblies. *Géotechnique*, 29(1):47–65, 1979. doi: 10.1680/geot.1979.29.1.47. URL https://doi.org/10.1680/geot.1979.29.1.47.

[44] Charles S. Campbell and Christopher E. Brennen. Computer simulation of granular shear flows. *Journal of Fluid Mechanics*, 151:167–188, 1985. doi: 10.1017/S002211208500091X.

[45] C. S. Campbell and C. E. Brennen. Chute Flows of Granular Material: Some Computer Simulations. *Journal of Applied Mechanics*, 52(1):172–178, 03 1985. ISSN 0021-8936. doi: 10.1115/1.3168990. URL https://doi.org/10.1115/1.3168990.

[46] Y. Tsuji, T. Tanaka, and T. Ishida. Lagrangian numerical simulation of plug flow of cohesionless particles in a horizontal pipe. *Powder Technology*, 71(3): 239–250, 1992. ISSN 0032-5910. doi: https://doi.org/10.1016/0032-5910(92)88030-L. URL https://www.sciencedirect.com/science/article/pii/003259109288030L.

[47] R. D. Mindlin and H. Deresiewicz. Elastic Spheres in Contact Under Varying Oblique Forces. *Journal of Applied Mechanics*, 20(3):327–344, 06 1953. ISSN 0021-8936. doi: 10.1115/1.4010702. URL https://doi.org/10.1115/1.4010702.

[48] HIDE SAKAGUCHI, EIJI OZAKI, and TOHRU IGARASHI. Plugging of the flow of granular materials during the discharge from a silo. *International Journal of Modern Physics B*, 07(09n10):1949–1963, 1993. doi: 10.1142/S0217979293002705. URL https://doi.org/10.1142/S0217979293002705.

[49] M.J. Jiang, H.-S. Yu, and D. Harris. A novel discrete model for granular material incorporating rolling resistance. *Computers and Geotechnics*, 32(5):340–357, 2005. ISSN 0266-352X. doi: https://doi.org/10.1016/j.compgeo.2005.05.001. URL https://www.sciencedirect.com/science/article/pii/S0266352X05000649.

[50] Steve Plimpton. Fast parallel algorithms for short-range molecular dynamics. *Journal of Computational Physics*, 117(1):1–19, 1995. ISSN 0021-9991. doi: https://doi.org/10.1006/jcph.1995.1039. URL https://www.sciencedirect.com/science/article/pii/S002199918571039X.

[51] C. Kloss, C. Goniva, A. Hager, S. Amberger, and S. Pirker. Models, algorithms and validation for open source dem and cfd-dem. *Progress in Computational Fluid Dynamics*, 12(2/3), 2012.

[52] Christoph Goniva, Christoph Kloss, Niels G. Deen, Johannes A.M. Kuipers, and Stefan Pirker. Influence of rolling friction on single spout fluidized bed simulation. *Particuology*, 10(5):582–591, 2012. ISSN 1674-2001. doi: https://doi.org/10.1016/j.partic.2012.05.002. URL https://www.sciencedirect.com/science/article/pii/S1674200112001356.

[53] Christian Ringl and Herbert M. Urbassek. A lammps implementation of granular mechanics: Inclusion of adhesive and microscopic friction forces. *Computer Physics Communications*, 183(4):986–992, 2012. ISSN 0010-4655. doi: https://doi.org/10.1016/j.cpc.2012.01.004. URL https://www.sciencedirect.com/science/article/pii/S0010465512000069.

[54] Han Wei, Yanhong Zhao, Jian Zhang, Henrik Saxén, and Yaowei Yu. Liggghts and edem application on charging system of ironmaking blast furnace. *Advanced Powder Technology*, 28(10):2482–2487, 2017. ISSN 0921-8831. doi: https://doi.org/10.1016/j.apt.2017.05.012. URL https://www.sciencedirect.com/science/article/pii/S0921883117302169.

[55] Cristina Ramírez-Aragón, Joaquín Ordieres-Meré, Fernando Alba-Elías, and Ana González-Marcos. Comparison of cohesive models in edem and liggghts for simulating powder compaction. *Materials*, 11(11), 2018. ISSN 1996-1944. doi: 10.3390/ma11112341. URL https://www.mdpi.com/1996-1944/11/11/2341.

[56] Thomas Roessler and André Katterfeld. Dem parameter calibration of cohesive bulk materials using a simple angle of repose test. *Particuology*, 45: 105 – 115, 2019. ISSN 1674-2001. doi: https://doi.org/10.1016/j.partic.2018.08.005. URL http://www.sciencedirect.com/science/article/pii/S1674200119300033.

[57] Han Wei, Hao Nie, Ying Li, Henrik Saxén, Zhijun He, and Yaowei Yu. Measurement and simulation validation of dem parameters of pellet, sinter and coke particles. *Powder Technology*, 364:593–603, 2020. ISSN 0032-5910. doi: https://doi.org/10.1016/j.powtec.2020.01.044. URL https://www.sciencedirect.com/science/article/pii/S0032591020300565.

[58] Jacob Rabinow. The magnetic fluid clutch. *Electrical Engineering*, 67(12): 1167–1167, 1948. doi: 10.1109/EE.1948.6444497.

[59] Pradeep P. Phulé. Magnetorheological (mr) fluids: Principles and applications. *Smart Materials Bulletin*, 2001(2):7 – 10, 2001. ISSN 1471-3918. doi: https://doi.org/10.1016/S1471-3918(01)80040-X. URL http://www.sciencedirect.com/science/article/pii/S147139180180040X.

[60] G Bossis, S Lacis, A Meunier, and O Volkova. Magnetorheological fluids. *Journal of Magnetism and Magnetic Materials*, 252:224 – 228, 2002. ISSN 0304-8853. doi: https://doi.org/10.1016/S0304-8853(02)00680-7. URL http://www.sciencedirect.com/science/article/pii/S0304885302006807. Proceedings of the 9th International Conference on Magnetic Fluids.

[61] Xu Biao, Luo Yiping, and Ren Hongjuan. Review on magneto-rheological fluid and its application. *American Journal of Nano Research and Applications*, 2 (4):70–74, July 2014.

[62] Juan de Vicente, Daniel J. Klingenberg, and Roque Hidalgo-Alvarez. Magnetorheological fluids: a review. *Soft Matter*, 7:3701–3710, 2011. doi: 10.1039/C0SM01221A. URL http://dx.doi.org/10.1039/C0SM01221A.

[63] Glen A. Dimock, Jin-Hyeong Yoo, and Norman M. Wereley. Quasi-steady bingham biplastic analysis of electrorheological and magnetorheological dampers. *Journal of Intelligent Material Systems and Structures*, 13(9):549–559, 2002. doi: 10.1106/104538902030906. URL https://doi.org/10.1106/104538902030906.

[64] D. W. Felt, M. Hagenbuchle, J. Liu, and J. Richard. Rheology of a magnetorheological fluid. *Journal of Intelligent Material Systems and Structures*, 7 (5):589–593, 1996. doi: 10.1177/1045389X9600700522.

[65] Bhau K. Kumbhar, Satyajit R. Patil, and Suresh M. Sawant. Synthesis and characterization of magneto-rheological (mr) fluids for mr brake application. *Engineering Science and Technology, an International Journal*, 18(3):432 – 438, 2015. ISSN 2215-0986. doi: https://doi.org/10.1016/j.jestch.2015.03.002.

[66] Robert Thomas Foister. Magnetorheological fluids. Patent US5667715A, 1997.

[67] Seval Genç and Pradeep P Phulé. Rheological properties of magnetorheological fluids. *Smart Materials and Structures*, 11(1):140–146, feb 2002. doi: 10.1088/0964-1726/11/1/316. URL `https://doi.org/10.1088%2F0964-1726%2F11%2F1%2F316`.

[68] A. J. F. BOMBARD, M. R. ALCÂNTARA, M. KNOBEL, and P. L. O. VOLPE. Experimental study of mr suspensions of carbonyl iron powders with different particle sizes. *International Journal of Modern Physics B*, 19 (07n09):1332–1338, 2005. doi: 10.1142/S0217979205030268. URL `https://doi.org/10.1142/S0217979205030268`.

[69] Wen Lu, Yiping Luo, LuLu Kang, and Dan Wei. Characteristics of magnetorheological fluids under new formulation. *Journal of Testing and Evaluation*, 47(4):3123–3137, 07 2018. doi: 10.1520/JTE20170477. URL `https://www.astm.org/DIGITAL_LIBRARY/JOURNALS/TESTEVAL/PAGES/JTE20170477.htm`.

[70] F D Goncalves and J D Carlson. An alternate operation mode for mr fluids-magnetic gradient pinch. *Journal of Physics: Conference Series*, 149(1): 012050, 2009.

[71] Abdul Yasser Abd Fatah, Saiful Amri Mazlan, Tsuyoshi Koga, Hairi Zamzuri, Mohammadjavad Zeinali, and Fitrian Imaduddin. A review of design and modeling of magnetorheological valve. *International Journal of Modern Physics B*, 29(04):1530004, 2015. doi: 10.1142/S0217979215300042.

[72] W. I. Kordonski and D. Golini. Fundamentals of magnetorheological fluid utilization in high precision finishing. *Journal of Intelligent Material Systems and Structures*, 10(9):683–689, 1999. doi: 10.1106/011M-CJ25-64QC-F3A6. URL `https://doi.org/10.1106/011M-CJ25-64QC-F3A6`.

[73] X. Tang, X. Zhang, R. Tao, and Yiming Rong. Structure-enhanced yield stress of magnetorheological fluids. *Journal of Applied Physics*, 87(5):2634–2638, 2000. doi: 10.1063/1.372229. URL `https://doi.org/10.1063/1.372229`.

[74] David Kittipoomwong, Daniel J. Klingenberg, and John C. Ulicny. Dynamic yield stress enhancement in bidisperse magnetorheological fluids. *Journal of*

Rheology, 49(6):1521–1538, 2005. doi: 10.1122/1.2085175. URL https://doi.org/10.1122/1.2085175.

[75] Jin-Hyeong Yoo and Norman M. Wereley. Design of a high-efficiency magnetorheological valve. *Journal of Intelligent Material Systems and Structures*, 13(10):679–685, 2002. doi: 10.1177/1045389X02013010012.

[76] H. X. Ai, D. H. Wang, and W. H. Liao. Design and modeling of a magnetorheological valve with both annular and radial flow paths. *Journal of Intelligent Material Systems and Structures*, 17(4):327–334, 2006. doi: 10.1177/1045389X06055283. URL https://doi.org/10.1177/1045389X06055283.

[77] D H Wang, H X Ai, and W H Liao. A magnetorheological valve with both annular and radial fluid flow resistance gaps. *Smart Materials and Structures*, 18(11):115001, sep 2009. doi: 10.1088/0964-1726/18/11/115001. URL https://doi.org/10.1088/0964-1726/18/11/115001.

[78] Fitrian Imaduddin, Saiful Amri Mazlan, Mohd Azizi Abdul Rahman, Hairi Zamzuri, Ubaidillah, and Burhanuddin Ichwan. A high performance magnetorheological valve with a meandering flow path. *Smart Materials and Structures*, 23(6):065017, may 2014. doi: 10.1088/0964-1726/23/6/065017. URL https://doi.org/10.1088/0964-1726/23/6/065017.

[79] Kyle Gilpin, Ara Knaian, and Daniela Rus. Robot pebbles: One centimeter modules for programmable matter through self-disassembly. In *Robotics and Automation (ICRA), 2010 IEEE International Conference on*, pages 2485–2492. IEEE, 2010.

[80] Ara Nerses Knaian. *Electropermanent magnetic connectors and actuators: devices and their application in programmable matter*. PhD thesis, Massachusetts Institute of Technology, 2010.

[81] N. Q. Guo, H. Du, and W. H. Li. Finite element analysis and simulation evaluation of a magnetorheological valve. *The International Journal of Advanced Manufacturing Technology*, 21(6):438–445, 2003. doi: 10.1007/s001700300051. URL https://doi.org/10.1007/s001700300051.

[82] Donald R. Davis, Clark R. Chapman, Stuart J. Weidenschilling, and Richard Greenberg. Collisional history of asteroids: Evidence from vesta and the hirayama families. *Icarus*, 62(1):30–53, 1985. ISSN 0019-1035. doi: https://doi.org/10.1016/0019-1035(85)90170-8. URL https://www.sciencedirect.com/science/article/pii/0019103585901708.

[83] P. Pravec, A.W. Harris, D. Vokrouhlický, B.D. Warner, P. Kušnirák, K. Hornoch, D.P. Pray, D. Higgins, J. Oey, A. Galád, Š. Gajdoš, L. Kornoš, J. Világi, M. Husárik, Yu.N. Krugly, V. Shevchenko, V. Chiorny, N. Gaftonyuk, W.R. Cooney, J. Gross, D. Terrell, R.D. Stephens, R. Dyvig, V. Reddy, J.G. Ries, F. Colas, J. Lecacheux, R. Durkee, G. Masi, R.A. Koff,

and R. Goncalves. Spin rate distribution of small asteroids. *Icarus*, 197 (2):497–504, 2008. ISSN 0019-1035. doi: https://doi.org/10.1016/j.icarus.2008.05.012. URL https://www.sciencedirect.com/science/article/pii/S0019103508002145.

[84] A. Fujiwara, J. Kawaguchi, D. K. Yeomans, M. Abe, T. Mukai, T. Okada, J. Saito, H. Yano, M. Yoshikawa, D. J. Scheeres, O. Barnouin-Jha, A. F. Cheng, H. Demura, R. W. Gaskell, N. Hirata, H. Ikeda, T. Kominato, H. Miyamoto, A. M. Nakamura, R. Nakamura, S. Sasaki, and K. Uesugi. The rubble-pile asteroid itokawa as observed by hayabusa. *Science*, 312(5778): 1330–1334, 2006. doi: 10.1126/science.1125841.

[85] S. Watanabe, M. Hirabayashi, N. Hirata, Na. Hirata, R. Noguchi, Y. Shimaki, H. Ikeda, E. Tatsumi, M. Yoshikawa, S. Kikuchi, H. Yabuta, T. Nakamura, S. Tachibana, Y. Ishihara, T. Morota, K. Kitazato, N. Sakatani, K. Matsumoto, K. Wada, H. Senshu, C. Honda, T. Michikami, H. Takeuchi, T. Kouyama, R. Honda, S. Kameda, T. Fuse, H. Miyamoto, G. Komatsu, S. Sugita, T. Okada, N. Namiki, M. Arakawa, M. Ishiguro, M. Abe, R. Gaskell, E. Palmer, O. S. Barnouin, P. Michel, A. S. French, J. W. McMahon, D. J. Scheeres, P. A. Abell, Y. Yamamoto, S. Tanaka, K. Shirai, M. Matsuoka, M. Yamada, Y. Yokota, H. Suzuki, K. Yoshioka, Y. Cho, S. Tanaka, N. Nishikawa, T. Sugiyama, H. Kikuchi, R. Hemmi, T. Yamaguchi, N. Ogawa, G. Ono, Y. Mimasu, K. Yoshikawa, T. Takahashi, Y. Takei, A. Fujii, C. Hirose, T. Iwata, M. Hayakawa, S. Hosoda, O. Mori, H. Sawada, T. Shimada, S. Soldini, H. Yano, R. Tsukizaki, M. Ozaki, Y. Iijima, K. Ogawa, M. Fujimoto, T.-M. Ho, A. Moussi, R. Jaumann, J.-P. Bibring, C. Krause, F. Terui, T. Saiki, S. Nakazawa, and Y. Tsuda. Hayabusa2 arrives at the carbonaceous asteroid 162173 ryugu—a spinning top–shaped rubble pile. *Science*, 364(6437):268–272, 2019. doi: 10.1126/science.aav8032. URL https://www.science.org/doi/abs/10.1126/science.aav8032.

[86] D. N. DellaGiustina, J. P. Emery, D. R. Golish, B. Rozitis, C. A. Bennett, K. N. Burke, R. L. Ballouz, K. J. Becker, P. R. Christensen, C. Y. Drouet d'Aubigny, V. E. Hamilton, D. C. Reuter, B. Rizk, A. A. Simon, E. Asphaug, J. L. Bandfield, O. S. Barnouin, M. A. Barucci, E. B. Bierhaus, R. P. Binzel, W. F. Bottke, N. E. Bowles, H. Campins, B. C. Clark, B. E. Clark, H. C. Connolly, M. G. Daly, J. de Leon, M. Delbo', J. D. P. Deshapriya, C. M. Elder, S. Fornasier, C. W. Hergenrother, E. S. Howell, E. R. Jawin, H. H. Kaplan, T. R. Kareta, L. Le Corre, J. Y. Li, J. Licandro, L. F. Lim, P. Michel, J. Molaro, M. C. Nolan, M. Pajola, M. Popescu, J. L. Rizos Garcia, A. Ryan, S. R. Schwartz, N. Shultz, M. A. Siegler, P. H. Smith, E. Tatsumi, C. A. Thomas, K. J. Walsh, C. W. V. Wolner, X. D. Zou, D. S. Lauretta, D. E. Highsmith, J. Small, D. Vokrouhlický, N. E. Bowles, E. Brown, K. L. Donaldson Hanna, T. Warren, C. Brunet, R. A. Chicoine, S. Desjardins, D. Gaudreau, T. Haltigin, S. Millington-Veloza, A. Rubi, J. Aponte, N. Gorius, A. Lunsford,

B. Allen, J. Grindlay, D. Guevel, D. Hoak, J. Hong, D. L. Schrader, J. Bayron, O. Golubov, P. Sánchez, J. Stromberg, M. Hirabayashi, C. M. Hartzell, S. Oliver, M. Rascon, A. Harch, J. Joseph, S. Squyres, D. Richardson, J. P. Emery, L. McGraw, R. Ghent, R. P. Binzel, M. M. Al Asad, C. L. Johnson, L. Philpott, H. C. M. Susorney, E. A. Cloutis, R. D. Hanna, H. C. Connolly, F. Ciceri, A. R. Hildebrand, E. M. Ibrahim, L. Breitenfeld, T. Glotch, A. D. Rogers, B. E. Clark, S. Ferrone, C. A. Thomas, H. Campins, Y. Fernandez, W. Chang, A. Cheuvront, D. Trang, S. Tachibana, H. Yurimoto, J. R. Brucato, G. Poggiali, M. Pajola, E. Dotto, E. Mazzotta Epifani, M. K. Crombie, C. Lantz, M. R. M. Izawa, J. de Leon, J. Licandro, J. L. Rizos Garcia, S. Clemett, K. Thomas-Keprta, S. Van wal, M. Yoshikawa, J. Bellerose, S. Bhaskaran, C. Boyles, S. R. Chesley, C. M. Elder, D. Farnocchia, A. Harbison, B. Kennedy, A. Knight, N. Martinez-Vlasoff, N. Mastrodemos, T. McElrath, W. Owen, R. Park, B. Rush, L. Swanson, Y. Takahashi, D. Velez, K. Yetter, C. Thayer, C. Adam, P. Antreasian, J. Bauman, C. Bryan, B. Carcich, M. Corvin, J. Geeraert, J. Hoffman, J. M. Leonard, E. Lessac-Chenen, A. Levine, J. McAdams, L. McCarthy, D. Nelson, B. Page, J. Pelgrift, E. Sahr, K. Stakkestad, D. Stanbridge, D. Wibben, B. Williams, K. Williams, P. Wolff, P. Hayne, D. Kubitschek, M. A. Barucci, J. D. P. Deshapriya, S. Fornasier, M. Fulchignoni, P. Hasselmann, F. Merlin, A. Praet, E. B. Bierhaus, O. Billett, A. Boggs, B. Buck, S. Carlson-Kelly, J. Cerna, K. Chaffin, E. Church, M. Coltrin, J. Daly, A. Deguzman, R. Dubisher, D. Eckart, D. Ellis, P. Falkenstern, A. Fisher, M. E. Fisher, P. Fleming, K. Fortney, S. Francis, S. Freund, S. Gonzales, P. Haas, A. Hasten, D. Hauf, A. Hilbert, D. Howell, F. Jaen, N. Jayakody, M. Jenkins, K. Johnson, M. Lefevre, H. Ma, C. Mario, K. Martin, C. May, M. McGee, B. Miller, C. Miller, G. Miller, A. Mirfakhrai, E. Muhle, C. Norman, R. Olds, C. Parish, M. Ryle, M. Schmitzer, P. Sherman, M. Skeen, M. Susak, B. Sutter, Q. Tran, C. Welch, R. Witherspoon, J. Wood, J. Zareski, M. Arvizu-Jakubicki, E. Asphaug, E. Audi, R. L. Ballouz, R. Bandrowski, K. J. Becker, T. L. Becker, S. Bendall, C. A. Bennett, H. Bloomenthal, D. Blum, W. V. Boynton, J. Brodbeck, K. N. Burke, M. Chojnacki, A. Colpo, J. Contreras, J. Cutts, C. Y. Drouet d'Aubigny, D. Dean, D. N. DellaGiustina, B. Diallo, D. Drinnon, K. Drozd, H. L. Enos, R. Enos, C. Fellows, T. Ferro, M. R. Fisher, G. Fitzgibbon, M. Fitzgibbon, J. Forelli, T. Forrester, I. Galinsky, R. Garcia, A. Gardner, D. R. Golish, N. Habib, D. Hamara, D. Hammond, K. Hanley, K. Harshman, C. W. Hergenrother, K. Herzog, D. Hill, C. Hoekenga, S. Hooven, E. S. Howell, E. Huettner, A. Janakus, J. Jones, T. R. Kareta, J. Kidd, K. Kingsbury, S. S. Balram-Knutson, L. Koelbel, and The OSIRIS-REx Team. Properties of rubble-pile asteroid (101955) bennu from osiris-rex imaging and thermal analysis. *Nature Astronomy*, 3(4):341–351, 2019. doi: 10.1038/s41550-019-0731-1. URL `https://doi.org/10.1038/s41550-019-0731-1`.

[87] Keith A. Holsapple. Spin limits of solar system bodies: From the small fast-rotators to 2003 el61. *Icarus*, 187(2):500–509, 2007. ISSN 0019-

1035. doi: https://doi.org/10.1016/j.icarus.2006.08.012. URL https://www.sciencedirect.com/science/article/pii/S0019103506002776.

[88] Keith A. Holsapple. On yorp-induced spin deformations of asteroids. *Icarus*, 205(2):430–442, 2010. ISSN 0019-1035. doi: https://doi.org/10.1016/j.icarus.2009.08.014. URL https://www.sciencedirect.com/science/article/pii/S0019103509003522.

[89] D.J. Scheeres, C.M. Hartzell, P. Sánchez, and M. Swift. Scaling forces to asteroid surfaces: The role of cohesion. *Icarus*, 210(2):968 – 984, 2010. ISSN 0019-1035. doi: https://doi.org/10.1016/j.icarus.2010.07.009. URL http://www.sciencedirect.com/science/article/pii/S0019103510002812.

[90] C.M. Hartzell, X. Wang, D.J. Scheeres, and M. Horányi. Experimental demonstration of the role of cohesion in electrostatic dust lofting. *Geophysical Research Letters*, 40(6):1038–1042, 2013. doi: https://doi.org/10.1002/grl.50230. URL https://agupubs.onlinelibrary.wiley.com/doi/abs/10.1002/grl.50230.

[91] Stephen R. Schwartz, Derek C. Richardson, and Patrick Michel. An implementation of the soft-sphere discrete element method in a high-performance parallel gravity tree-code. *Granular Matter*, 14(3):363–380, 2012. doi: 10.1007/s10035-012-0346-z. URL https://doi.org/10.1007/s10035-012-0346-z.

[92] C. Cournede, J. Gattacceca, M. Gounelle, P. Rochette, B.P. Weiss, and B. Zanda. An early solar system magnetic field recorded in cm chondrites. *Earth and Planetary Science Letters*, 410:62–74, 2015. ISSN 0012-821X. doi: https://doi.org/10.1016/j.epsl.2014.11.019. URL https://www.sciencedirect.com/science/article/pii/S0012821X14007110.

[93] Birlan, M., Vernazza, P., and Nedelcu, D. A. Spectral properties of nine m-type asteroids. *A&A*, 475(2):747–754, 2007. doi: 10.1051/0004-6361:20077914. URL https://doi.org/10.1051/0004-6361:20077914.

[94] S. Fornasier, B.E. Clark, E. Dotto, A. Migliorini, M. Ockert-Bell, and M.A. Barucci. Spectroscopic survey of m-type asteroids. *Icarus*, 210(2):655–673, 2010. ISSN 0019-1035. doi: https://doi.org/10.1016/j.icarus.2010.07.001. URL https://www.sciencedirect.com/science/article/pii/S0019103510002733.

[95] Ostro Steven J., Scott R., Hudson null, Nolan Michael C., Margot Jean-Luc, Scheeres Daniel J., Campbell Donald B., Magri Christopher, Giorgini Jon D., and Yeomans Donald K. Radar observations of asteroid 216 kleopatra. *Science*, 288(5467):836–839, 2021/09/13 2000. doi: 10.1126/science.288.5467.836. URL https://doi.org/10.1126/science.288.5467.836.

[96] P. Descamps, F. Marchis, J. Pollock, J. Berthier, F. Vachier, M. Birlan, M. Kaasalainen, A.W. Harris, M.H. Wong, W.J. Romanishin, E.M. Cooper,

K.A. Kettner, P. Wiggins, A. Kryszczynska, M. Polinska, J.-F. Coliac, A. Devyatkin, I. Verestchagina, and D. Gorshanov. New determination of the size and bulk density of the binary asteroid 22 kalliope from observations of mutual eclipses. *Icarus*, 196(2):578–600, 2008. ISSN 0019-1035. doi: https://doi.org/10.1016/j.icarus.2008.03.014. URL https://www.sciencedirect.com/science/article/pii/S0019103508001309. Mars Polar Science IV.

[97] Bryce T. Bolin, Harold A. Weaver, Yanga R. Fernandez, Carey M. Lisse, Daniela Huppenkothen, R. Lynne Jones, Mario Jurić, Joachim Moeyens, Charles A. Schambeau, Colin. T. Slater, Željko Ivezić, and Andrew J. Connolly. APO time-resolved color photometry of highly elongated interstellar object 1i/'oumuamua. *The Astrophysical Journal*, 852(1):L2, dec 2017. doi: 10.3847/2041-8213/aaa0c9. URL https://doi.org/10.3847/2041-8213/aaa0c9.

[98] Marco Micheli, Davide Farnocchia, Karen J. Meech, Marc W. Buie, Olivier R. Hainaut, Dina Prialnik, Norbert Schörghofer, Harold A. Weaver, Paul W. Chodas, Jan T. Kleyna, Robert Weryk, Richard J. Wainscoat, Harald Ebeling, Jacqueline V. Keane, Kenneth C. Chambers, Detlef Koschny, and Anastassios E. Petropoulos. Non-gravitational acceleration in the trajectory of 1i/2017 u1 ('oumuamua). *Nature*, 559(7713):223–226, 2018. doi: 10.1038/s41586-018-0254-4. URL https://doi.org/10.1038/s41586-018-0254-4.

[99] Thomas Leps and Christine Hartzell. High fidelity, discrete element method simulation of magnetorheological fluids using accurate particle size distributions in LIGGGHTS extended with mutual dipole method. *Materials Research Express*, 8(8):085701, aug 2021. doi: 10.1088/2053-1591/ac113c. URL https://doi.org/10.1088/2053-1591/ac113c.

[100] H. Chen, Y.G. Xiao, Y.L. Liu, and Y.S. Shi. Effect of young's modulus on dem results regarding transverse mixing of particles within a rotating drum. *Powder Technology*, 318:507 – 517, 2017. ISSN 0032-5910.

[101] T Leps, P E Glick, D Ruffatto III, A Parness, M T Tolley, and C Hartzell. A low-power, jamming, magnetorheological valve using electropermanent magnets suitable for distributed control in soft robots. *Smart Materials and Structures*, 29(10):105025, sep 2020. doi: 10.1088/1361-665x/abadd4. URL https://doi.org/10.1088/1361-665x/abadd4.

[102] Norman M Wereley, editor. *Magnetorheology*. Smart Materials Series. The Royal Society of Chemistry, 2014.

[103] Osama Ashour, Craig A Rogers, and William Kordonsky. Magnetorheological fluids: materials, characterization, and devices. *Journal of intelligent material systems and structures*, 7(2):123–130, 1996.

[104] Christine M Hartzell, Young T Choi, Norman M Wereley, and Thomas Leps. Performance of a magnetorheological fluid-based robotic end effector. *Smart Materials and Structures*, 28(3):035030, 2019.

[105] Nicholas Wiltsie, Michele Lanzetta, and Karl Iagnemma. A controllably adhesive climbing robot using magnetorheological fluid. In *Technologies for Practical Robot Applications (TePRA), 2012 IEEE International Conference on*, pages 91–96. IEEE, 2012.

[106] Iker Zuriguel, Angel Garcimartín, Diego Maza, Luis A. Pugnaloni, and J. M. Pastor. Jamming during the discharge of granular matter from a silo. *Phys. Rev. E*, 71:051303, May 2005.

[107] Andrew D Marchese, Cagdas D Onal, and Daniela Rus. Soft robot actuators using energy-efficient valves controlled by electropermanent magnets. In *Intelligent Robots and Systems (IROS), 2011 IEEE/RSJ International Conference on*, pages 756–761. IEEE, 2011.

[108] G. Gerboni, T. Ranzani, A. Diodato, G. Ciuti, M. Cianchetti, and A. Menciassi. Modular soft mechatronic manipulator for minimally invasive surgery: overall architecture and development of a fully integrated soft module. *Meccanica*, 50(11):2865–2878, 2015.

[109] J. W. Booth, J. C. Case, E. L. White, D. S. Shah, and R. Kramer-Bottiglio. An addressable pneumatic regulator for distributed control of soft robots. In *2018 IEEE International Conference on Soft Robotics (RoboSoft)*, pages 25–30, April 2018. doi: 10.1109/ROBOSOFT.2018.8404892.

[110] Alì Sadeghi, Lucia Beccai, and Barbara Mazzolai. Innovative soft robots based on electro-rheological fluids. In *Intelligent Robots and Systems (IROS), 2012 IEEE/RSJ International Conference on*, pages 4237–4242. IEEE, 2012.

[111] Panagiotis Polygerinos, Nikolaus Correll, Stephen A Morin, Bobak Mosadegh, Cagdas D Onal, Kirstin Petersen, Matteo Cianchetti, Michael T Tolley, and Robert F Shepherd. Soft robotics: Review of fluid-driven intrinsically soft devices; manufacturing, sensing, control, and applications in human-robot interaction. *Advanced Engineering Materials*, 2017.

[112] Daniela Rus and Michael T Tolley. Design, fabrication and control of soft robots. *Nature*, 521(7553):467, 2015.

[113] Paul Glick, Srinivasan Suresh, Donald Ruffatto III, Mark Cutkosky, Michael T Tolley, and Aaron Parness. A soft robotic gripper with gecko-inspired adhesive. *IEEE Robotics and Automation Letters*, 2018.

[114] Michael Wehner, Michael T Tolley, Yiğit Mengüç, Yong-Lae Park, Annan Mozeika, Ye Ding, Cagdas Onal, Robert F Shepherd, George M Whitesides, and Robert J Wood. Pneumatic energy sources for autonomous and wearable soft robotics. *Soft Robotics*, 1(4):263–274, 2014.

[115] Michael Fanton, Paul Glick, Jonathan Bruce, Ken Caluwaerts, Jeffery Friesen, and Vytas Sunspiral. Robust and efficient multistage braking system for cable driven robots. In *Proc. 13th Int. Symp. Artif. Intell., Robot. Autom. Space*, 2016.

[116] D. Ruffatto, P. E. Glick, M. T. Tolley, and A. Parness. Long-duration surface anchoring with a hybrid electrostatic and gecko-inspired adhesive. *IEEE Robotics and Automation Letters*, 3(4):4201–4208, Oct 2018. ISSN 2377-3766. doi: 10.1109/LRA.2018.2856366.

[117] Steven I Rich, Robert J Wood, and Carmel Majidi. Untethered soft robotics. *Nature Electronics*, 1(2):102, 2018.

[118] Nils Napp, Brandon Araki, Michael T Tolley, Radhika Nagpal, and Robert J Wood. Simple passive valves for addressable pneumatic actuation. In *Robotics and Automation (ICRA), 2014 IEEE International Conference on*, pages 1440–1445. IEEE, 2014.

[119] Philipp Rothemund, Alar Ainla, Lee Belding, Daniel J Preston, Sarah Kurihara, Zhigang Suo, and George M Whitesides. A soft, bistable valve for autonomous control of soft actuators. *Science Robotics*, 3(16):eaar7986, 2018.

[120] Bobak Mosadegh, Chuan-Hsien Kuo, Yi-Chung Tung, Yu-suke Torisawa, Tommaso Bersano-Begey, Hossein Tavana, and Shuichi Takayama. Integrated elastomeric components for autonomous regulation of sequential and oscillatory flow switching in microfluidic devices. *Nature physics*, 6(6):433, 2010.

[121] Alex Zatopa, Steph Walker, and Yigit Menguc. Fully soft 3d-printed electroactive fluidic valve for soft hydraulic robots. *Soft robotics*, 2018.

[122] Alice Tonazzini, Ali Sadeghi, and Barbara Mazzolai. Electrorheological valves for flexible fluidic actuators. *Soft Robotics*, 3(1):34–41, 2016.

[123] Ahmed H Helal et al. *Designing devices using electro-active yield stress fluids*. PhD thesis, Massachusetts Institute of Technology, 2016.

[124] Melek Yalcintas and Heming Dai. Magnetorheological and electrorheological materials in adaptive structures and their performance comparison. *Smart Materials and Structures*, 8(5):560, 1999.

[125] Kristin Lochmann, Luc Oger, and Dietrich Stoyan. Statistical analysis of random sphere packings with variable radius distribution. *Solid State Sciences*, 8(12):1397 – 1413, 2006.

[126] A. Hager, C. Kloss, S. Pirker, and C. Goniva. Parallel resolved open source cfd-dem: Method, validation and application. *The Journal of Computational Multiphase Flows*, 6(1):13–27, 2014. doi: 10.1260/1757-482X.6.1.13.

[127] D.C. Richardson, Z.M. Leinhardt, H.J. Melosh, W.F. Bottke, and E. Asphaug. *Gravitational Aggregates: Evidence and Evolution*, pages 501–515. University of Arizona Press, 2002.

[128] Masatoshi Hirabayashi, Daniel J. Scheeres, Diego Paul Sánchez, and Travis Gabriel. CONSTRAINTS ON THE PHYSICAL PROPERTIES OF MAIN BELT COMET p/2013 r3 FROM ITS BREAKUP EVENT. *The Astrophysical Journal*, 789(1):L12, jun 2014. doi: 10.1088/2041-8205/789/1/l12. URL https://doi.org/10.1088/2041-8205/789/1/l12.

[129] William F. Bottke, David Vokrouhlický, David P. Rubincam, and David Nesvorný. The yarkovsky and yorp effects: Implications for asteroid dynamics. *Annual Review of Earth and Planetary Sciences*, 34(1):157–191, 2006. doi: 10.1146/annurev.earth.34.031405.125154. URL https://doi.org/10.1146/annurev.earth.34.031405.125154.

[130] D.J. Scheeres. Disaggregation of small, cohesive rubble pile asteroids due to yorp. *Icarus*, 304:183–191, 2018. ISSN 0019-1035. doi: https://doi.org/10.1016/j.icarus.2017.05.029. URL https://www.sciencedirect.com/science/article/pii/S0019103517300404. Asteroids and Space Debris.

[131] F.E. DeMeo and B. Carry. The taxonomic distribution of asteroids from multi-filter all-sky photometric surveys. *Icarus*, 226(1):723 – 741, 2013. ISSN 0019-1035. doi: https://doi.org/10.1016/j.icarus.2013.06.027. URL http://www.sciencedirect.com/science/article/pii/S0019103513002923.

[132] E. Asphaug and A. Reufer. Mercury and other iron-rich planetary bodies as relics of inefficient accretion. *Nature Geoscience*, 7(8):564–568, 2014. doi: 10.1038/ngeo2189. URL https://doi.org/10.1038/ngeo2189.

[133] Yun Zhang and Douglas N. C. Lin. Tidal fragmentation as the origin of 1i/2017 u1 ('oumuamua). *Nature Astronomy*, 4(9):852–860, 2020. doi: 10.1038/s41550-020-1065-8. URL https://doi.org/10.1038/s41550-020-1065-8.

[134] Nikolai V. Brilliantov, Frank Spahn, Jan-Martin Hertzsch, and Thorsten Pöschel. Model for collisions in granular gases. *Phys. Rev. E*, 53:5382–5392, May 1996. doi: 10.1103/PhysRevE.53.5382. URL https://link.aps.org/doi/10.1103/PhysRevE.53.5382.

[135] Stefan Luding. Cohesive, frictional powders: contact models for tension. *Granular Matter*, 10(4):235, 2008. doi: 10.1007/s10035-008-0099-x. URL https://doi.org/10.1007/s10035-008-0099-x.

[136] Steve Plimpton, Roy Pollock, and Mark Stevens. Particle-mesh ewald and rrespa for parallel molecular dynamics simulations. In *Proc. Eighth SIAM Conf. Parallel Process. Sci. Comp.*, 1997.

[137] A Fluglistaler and D Pfenniger. Substellar fragmentation in self-gravitating fluids with a major phase transition. *A&A*, 578:A18, 2015. doi: 10.1051/0004-6361/201424798. URL https://doi.org/10.1051/0004-6361/201424798.

[138] Michael K. Shepard, James Richardson, Patrick A. Taylor, Linda A. Rodriguez-Ford, Al Conrad, Imke de Pater, Mate Adamkovics, Katherine de Kleer, Jared R. Males, Katie M. Morzinski, Laird M. Close, Mikko Kaasalainen, Matti Viikinkoski, Bradley Timerson, Vishnu Reddy, Christopher Magri, Michael C. Nolan, Ellen S. Howell, Lance A.M. Benner, Jon D. Giorgini, Brian D. Warner, and Alan W. Harris. Radar observations and shape model of asteroid 16 psyche. *Icarus*, 281:388 – 403, 2017. ISSN 0019-1035. doi: https://doi.org/10.1016/j.icarus.2016.08.011. URL http://www.sciencedirect.com/science/article/pii/S0019103516300288.